# Specific ion effects and the molecular structure of water, ions and amphiphiles on nanoscopic hydrophobic interfaces

THÈSE N$^{O}$ 6060 (2014)

PRÉSENTÉE LE 19 FÉVRIER 2014

À LA FACULTÉ DES SCIENCES ET TECHNIQUES DE L'INGÉNIEUR

CHAIRE JULIA JACOBI DE PHOTOMÉDECINE - LABORATOIRE DE BIOPHOTONIQUE FONDAMENTALE

PROGRAMME DOCTORAL EN PHOTONIQUE

ÉCOLE POLYTECHNIQUE FÉDÉRALE DE LAUSANNE

POUR L'OBTENTION DU GRADE DE DOCTEUR ÈS SCIENCES

PAR

Rüdiger SCHEU

acceptée sur proposition du jury:

Prof. A. Radenovic, présidente du jury
Prof. S. Roke, directrice de thèse
Dr M. A. Brown, rapporteur
Dr R. K. Campen, rapporteur
Prof. T. Rizzo, rapporteur

ÉCOLE POLYTECHNIQUE
FÉDÉRALE DE LAUSANNE

Suisse
2014

# Abstract

*The molecular-level structure of aqueous interfaces plays a key role for many phenomena in life sciences. Water's complex structure and hydrogen bonding propensity brings about phenomena that are specific to the size and composition of ions and ionic groups or to the charge of ionic species. To obtain a molecular-level understanding of the processes happening at aqueous (biological) interfaces, experiments that probe structure and dynamics in realistic model systems are needed. In this thesis, we investigate ion-specific, amphiphile-specific, and charge-specific effects at a nanoscopic hydrophobic interface. Using sum frequency and second harmonic scattering, intrinsically interface-specific techniques, we access the structure of ions, amphiphiles, the hydrophobic phase and water. Electrophoretic mobility and Raman measurements provide additional information about the charge density of the interface and the hydration of ions and amphiphiles in the bulk solution. Investigating hydrophobic effects in a series of tetraalkylammonium ions, we found that a mixed stern (mono-)layer is formed when the ionic solutes extend a typical size of $\sim 1\,nm$, the length scale on which the crossover from small to large-scale hydrophobicity occurs. Further, the influence of ionic amphiphiles with equal alkyl chains but different head groups on the hydrophobic oil-water interface has been investigated; we found that the different amphiphiles have a distinct interaction with water, resulting in strikingly different interfacial structures of both amphiphile and oil molecules. Moreover, we investigated inherent charge asymmetries in the interaction of ions with water; tetraphenylborate and tetraphenylarsonium, ions of opposite charge but otherwise virtually identical chemical properties, show a strikingly different interaction with water and accordingly a distinct molecular structure at a hydrophobic interface.*

**List of keywords:** interfaces, water, amphiphiles, specific ion effects, hydrophobic effect, charge asymmetry, sum frequency scattering, second harmonic scattering, time-resolved sum frequency scattering

# Résumé

*La structure des interfaces aqueuses à l'échelle moléculaire joue un rôle clé dans de nombreux phénomènes en sciences de la vie. La structure complexe de l'eau et son penchant à créer des liaisons d'hydrogène donne naissance à des phénomènes spécifiques à la taille, la structure, ou à la charge des ions/groupes ioniques. Pour comprendre les processus qui interviennent au niveau des interfaces aqueuses (biologiques) à l'échelle moléculaire, il est nécessaire de sonder la structure et la dynamique des molécules dans des systèmes modèles réalistiques. Dans cette thèse, nous étudions ces effets spécifiques au niveau des interfaces hydrophobes nanoscopiques. En utilisant la spectroscopie de la diffusion de la fréquence somme et de la seconde harmonique — méthodes intrinsèquement spécifiques aux interfaces — nous pouvons accéder à la structure de différentes entités : ions, amphiphiles, phase hydrophobe et eau. Des informations supplémentaires sur la densité de charge de l'interface et sur l'hydratation des ions/amphiphiles sont obtenues par mesures de la mobilité électrophorétique et par spectroscopie Raman. En étudiant les effets hydrophobes dans une série d'ions tétraalkylammonium, nous avons trouvé qu'une couche Stern se forme lorsque les solutés ioniques ont une taille typique de $\gtrsim 1\,nm$ — taille typique correspondant à la transition entre petite et grande échelle d'hydrophobicité. De plus, l'influence des amphiphiles ioniques composées de chaînes alkyles égales et de groupes de tête différents, sur l'interface hydrophobe huile-eau a été étudié. Nous avons trouvé que ces amphiphiles présentent une interaction très différente avec l'eau selon leur composition, en exposant une structure interfaciale differente au niveau des amphiphiles et des molécules d'eau. Finalement, nous avons étudié l'asymétrie inhérente de charge dans l'interaction des ions avec l'eau au sein même d'un volume et à l'interface huile-eau ; Les ions tétraphénylborate et tétraphénylarsonium, de charge opposée mais de propriétés quasiment identiques, montrent des interactions remarquablement différentes avec l'eau et entraîne ainsi à la formation d'une structure moléculaire distincte au niveau de l'interface.*

**Liste des mots clés :** interfaces, eau, amphiphiles, effets spécifiques au ions, l'effet hydrophobe, asymétrie de charge, diffusion de la fréquence somme, seconde harmonique

# Contents

# List of Figures

# Introduction

Interfaces emerge where two phases or immiscible substances face each other. They define the boundaries of media and thus control transport phenomena. Their microscopic properties influence the 'strength' and stability of the boundaries and therefore determine the macroscopic structure of materials. In this way, interfaces and particularly aqueous interfaces play a key role for a wide range of phenomena in technology and life sciences. For example, in biology, ions at membrane-water interfaces regulate biological cell function, where particular tasks are handled by specific choices of ions[1]. Biologists have been aware of effects that are specific to ions or ionic groups, as such effects are ubiquitous; for example, they play a key role for all sorts of complex structural rearrangements such as protein folding, self-assembly, or molecular transport[2,3]. Yet, those effects are not accommodated by the classical (continuum) theories[4]. Continuum theories neglect the molecular structure of water and thus lack a complete description of important effects, such as (i) the hydrophobic effect due to strong (cooperative) water-water interaction, (ii) specific interaction of water with ions or functional groups, and (iii) specificity with respect to charge.

An ongoing debate about the origin of specific ion phenomena exists. The effects have either been attributed to direct ion-macromolecule and ion-surface interactions or to the ions' influence on the water structure, as already proposed by Franz Hofmeister in his pioneering work in the 19th century[5–8]. Recent studies indicate that the hydration of ions and ionic groups at interfaces is key to understand ionic specificity[6,9–11]. At a hydrophobic surface and around a hydrophobic ion such as iodide, water structures in a way that is energetically quite unfavorable. To remove the unfavorably structured water, the hydrophobic ion is driven towards the surface. As seen in the example of iodide[12], this propensity can even overcome electrostatic attraction to nearby surface patches. Further, as pointed out by recent theoretical investigations, the nanoscale structure at interfaces critically affects hydrophobic behavior. Macroscopic effects cannot be simply translated to the nanoscale regime[13–15]. Despite many advances in theoretical modelling, many

challenges remain and experiments that are able to probe the water and the surface structure in realistic model systems are needed to fully understand and control the complex phenomena at nanoscopic interfaces, such as those of vesicles or proteins[16].

A large number of tools have been developed in the field of surface/interface science, but most of them are limited in their application[17]. Electron scattering and photoemission require vacuum, and thus cannot be used under physiological conditions. Other methods such as neutron and x-ray scattering require extensive instrumentation and suppression of the bulk response[18,19]. Optical techniques, however, allow in-situ probing of essentially all materials that are accessible to light. Furthermore, nonlinear optical sum frequency and second harmonic generation (SFG and SHG) allow for interfacial specificity down to sub-monolayers of molecules[20]. These methods are dipole-forbidden in inversion-symmetric media such as isotropic liquids or gases. Interfaces are per se asymmetric; hence, the selection-rules render SFG and SHG inherently sensitive to interfaces in otherwise isotropic media. Infrared-visible SFG further allows probing of vibrational 'fingerprints' of interfacial molecules, thus adding chemical specificity[20,21]. SFG has proven to be a powerful tool to study specific ion adsorption and water structuring at the vapor-water and solid-water interfaces[22–27]; however, it has been restricted to macroscopically planar interfaces. As pointed out in the latter paragraph, biologically relevant interfaces such as those of proteins, vesicles, or cells are structured on the nanoscale. To access them, SFG (and SHG) can be combined with light scattering techniques, thereby extending its application to nanoscopic systems and aqueous dispersions. Using sum frequency scattering (SFS), insights into phenomena at colloidal particle, nanoscopic oil droplet, and catanionic vesicle interfaces have been gained, revealing fundamental differences between nanoscopic hydrophobic and planar hydrophobic interfaces[27–31]. Further advantages of SFS are that it facilitates the measurement of liquid-liquid interfaces and that it is less prone to impurities because of the large surface-to-volume ratios in nanoscopic dispersions[32,33].

In this thesis, sum frequency and second harmonic scattering (SFS and SHS) are used to investigate specific ion, amphiphile, and charge effects at nanoscopic hydrophobic interfaces. We address key issues of specificity induced by the interaction with water: the effect of hydrophobic counterions on the interfacial structure, 'specific amphiphile' effects in surface stabilization, and inherent charge asymmetry in ionic hydration in the bulk and at the interface.

Hydrophobic effects were studied in a series of tetraalkylammonium (TAA) ions with gradually varying hydrophobic interaction. We followed the change in the structure of the oil-water interface induced by tuning the hydrophobicity of

the TAA ions in the solution. Using a combination of surface-specific techniques, we are able to clearly separate effects on the structure of water, the adsorbed amphiphiles, the counterions, and on the interfacial charge density. We found that the induced Stern layer appears to be rather a mixed monolayer and not, as often seen in textbooks, a capacitor-like double layer. Moreover, a transition from bulk-active to surface-active behavior was found to happen at a TAA size of $\sim$1 nm, the length scale on which the crossover from microscopic to macroscopic hydrophobicity occurs[34].

With the ionic amphiphiles dodecyl sulfate ($DS^-$) and dodecyltrimethylammonium ($DTA^+$), we investigated how the head group of an amphiphile affects the stabilization of the hydrophobic oil-water interface. The two amphiphiles, which macroscopically appear to behave similarly, adopt and induce strikingly different surface structures. The observed differences can be attributed to the head group hydration and suggest a Hofmeister-like ordering for amphiphilies.

In the Hofmeister series for anions and cations, differences between the ions are typically more pronounced for anions. We address this issue of charge asymmetry that is also inherent in many interfacial systems. For example, air bubbles and oil droplets in water appear to be negatively charged, as indicated by them migrating towards the positive electrode[35]. This preference for the apparent negative charge, though fascinating, has yet remained unexplained. Using surface-active ions of opposite charge but virtually identical chemical properties, we quantify charge asymmetry and demonstrate how such an inherent asymmetry arises on a molecular level.

The presented work reveals striking features in the structure of hydrophobic water interfaces. To further elucidate the microscopic mechanisms that govern the studied phenomena, the dynamics of the systems will provide further input. In this thesis a key step towards the study of vibrational dynamics at nanoscopic and liquid-liquid interfaces has been taken. We realized a time-resolved SFS measurement on a nanoscopic amphiphile-stabilized dispersion by probing the dephasing of the alkyl chain and headgroup vibrations of $DS^-$ amphiphiles.

**This thesis**

The chapters of this thesis are organized as follows:

- Starting with a short historical introduction, Chapter 1 introduces the topic of specific ion effects and the hydrophobic effect. The chapter also introduces the background information on the employed methods used in this work.
- Chapter 2 presents a realization of a time-resolved sum frequency scattering experiment, probing the free induction decay of the vibrations of dodecyl sulfate ($DS^-$) ions in the C-H stretch and vibrational fingerprint region.
- Chapter 3 describes the study of hydrophobic effects with tetraalkylammonium ($TAA^+$)ions that induce a Stern layer formation at the hydrophobic water interface.
- Chapter 4 describes the study of the differences in interface stabilization with ionic dodecylsulfate ($DS^-$) and dodecyltrimethylammonium ($DTA^+$) amphiphiles.
- Chapter 5 describes the study of the inherent charge asymmetry of ion hydration in the bulk solution and at the hydrophobic interface using tetraphenylborate ($Ph_4B^-$) and tetraphenylarsonium ($Ph_4As^+$) — ions of opposite charge, but virtually identical chemical properties.

The thesis finishes with conclusive remarks about the work and an outlook giving future perspectives.

# 1 Methods and research background

*This introductory chapter aims at providing the reader with background information about the employed methods and the research background. Specific ion (Hofmeister) effects and the hydrophobic effect are shortly reviewed, starting off with a historical perspective of Hofmeister's experiments. The experimental methods and in particular sum frequency scattering (SFS) are introduced.*

## 1.1 Research background: Ionic specificity

As we have seen in the introduction and will further see in the following chapters, effects that are specific to the composition/structure of ions, ionic groups, or the charge of ionic species, occur everywhere. Such effects have been extensively studied in the context of specific ion effects, i.e. the *Hofmeister series*. The *origin* of ionic specificity is hotly debated; ion-macromolecule/surface, ion-water, or water-water interactions are candidates. At any rate, water's propensity to hydrogen bond giving rise to the *hydrophobic effect* and water's *asymmetric molecular structure* certainly play a key role for a full understanding of the phenomena.

In the following we will address the above-mentioned key issues of Hofmeister effects, the origin of ionic specificity, the hydrophobic effect, and the importance of water's molecular structure.

**Hofmeister series.** In 1888, Franz Hofmeister, together with his coworkers, started to publish a series of papers entitled "Zur Lehre von der Wirkung der Salze", which could be loosely translated as 'teachings about the effects of salts'. Hofmeister did not only perform the first systematic studies about the precipitating effect of ions in aqueous solution, but he was also the first to draw important conclusions about the interaction of water with salts[36]. He stated this as follows:

> *"As an explanation (...) no assumption is better than that the globulin precipitation results from the water withdrawing capability of the added salt, and that this water withdrawing capability cannot be attributed to each salt to the same degree. (...) If this is correct, one has to expect that the order of the salts according to their precipitating effect should not only be valid for proteins, but also for other colloidal substances, and that this order can be associated with the diverse physical properties of salt solutions, which one has reason to explain by one or few intimate relations of the salts to water."*

Hence, Hofmeister already suspected that the effect is much more general and not merely associated with protein precipitation. Due to his pioneering work, specific ion effects are also commonly termed as Hofmeister effects. Diverse phenomena and properties are affected by ion-specificity: solubility of salts, electrolyte activities, zeta potentials, critical micelle concentrations, membrane, protein and colloidal stability[3,37]. A typical ordering of ions is shown in Fig. 1.1; however, the Hofmeister ordering is not unique and each ion series depends in general on the counterions present. The classification of ions as being 'soft' or 'hard' was introduced by

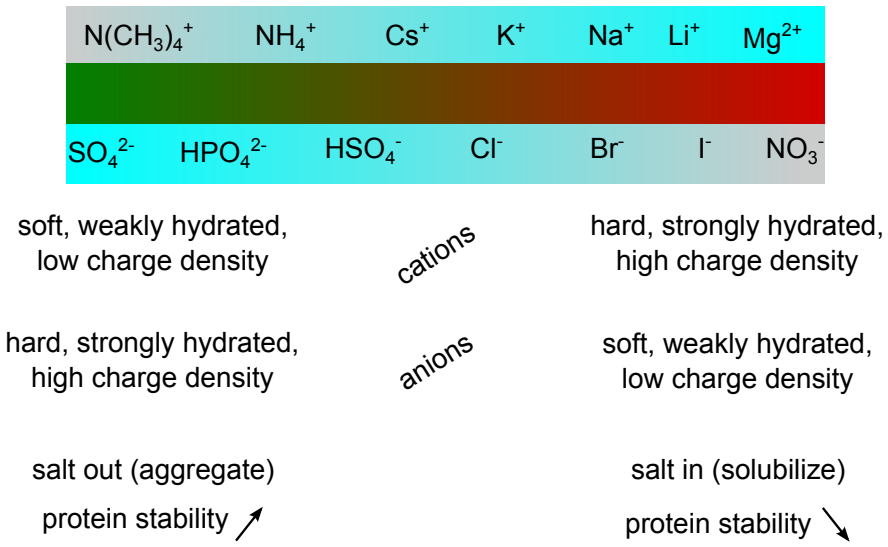


Figure 1.1: Typical ordering of cations and anions in a Hofmeister series. Adapted from Ref. 3.

Pearson[38,39]. Chemical 'hardness' essentially means resistance to deformation or change[†]. Soft, weakly hydrated ions have a large propensity for hydrophobic interfaces[40]. Accordingly, the same could be suspected for soft ionic groups, for example in amphiphiles. In Chapter 4, we therefore correlate amphiphile-specific effects with the well-known Hofmeister effects. We will discuss how amphiphiles with soft ($DTA^+$) and hard ($DS^-$) head groups distinctly influence the interfacial structure of the oil-water interface. The two ionic headgroups resemble the $HSO_4^-$ and $N(CH_3)_4^+$ ions in the Hofmeister series, suggesting that the way the amphiphiles are hydrated is the origin of their distinct behavior.

It is interesting that, in a certain sense, the order of cations and anions (or accordingly of cationic and anionic groups) is reversed (Fig. 1.1). Weakly hydrated soft cations such as $N(CH_3)_4^+$ but strongly hydrated hard anions such as $SO_4^{2-}$ both increase protein stability, i.e. they keep the proteins from salting-in and allow them to keep their native folded structure. Most likely, this opposite ordering has to do with the different functional groups present in proteins: soft cationic groups such as ammonium and hard anionic groups such as carboxylates. It can be partly explained by the concept of matching water affinities, stating that soft

[†]Here, change is meant in the sense as to add or remove an electron; hardness is therefore defined as the second derivative of the potential energy with respect to the number of electrons. The analogy stems from the fact that a mechanical oscillator is 'stiff' or resistant against external forces if the curvature of the potential, i.e. the second derivative of the force with respect to elongation, is large.

cations/cationic groups interact most easily with soft anions/anionic groups[41,42]. This concept of matching water affinity can be seen as a particular case of the general rule often found in chemistry: “like likes like" and stresses the importance of the interaction of water with ions and ionic groups.

**Origin of ionic specificity.** Although ion-specific effects are widespread, there is still an ongoing debate on the relative importance of direct ion-macromolecule/surface interactions, ion-water, and water-water interactions. Evidences for and against the ions' influence on the water structure have been brought forward recently[5,9,43]. The question is whether one can actually attribute *structure-making* (kosmotropic) and *structure-breaking* (chaotropic) properties to the ions; this is connected to the question of how many layers in the hydration shell can be influenced by the ions. Either way, the fact that specific ion effects are particularly pronounced at aqueous interfaces and in aqueous solutions points to the key role of water for the phenomena.

**The hydrophobic effect.** The strong water-water interaction through hydrogen bonding drives ions with low charge density and of large dimension to surfaces or leads to ion-ion aggregation. This *hydrophobic effect* and the resulting hydrophobic interaction can be captured to a great extent by the size of ions and plays an important role for specific ion effects[13,34,44]. The free energy cost to solvate an ion in the water phase is in the absence of strong ion-water interactions mainly attributed to the formation of a cavity. Small solutes can be more easily ‘encaged’ by water molecules in a hydrogen bonding network. If the size of the solute exceeds a critical dimension of about 1 nm, the water network moves away from the solute to maintain as many hydrogen bonds as possible[34,45]. This important crossover, as confirmed by recent studies[46,47], also seems to affect a transition in the adsorption behavior of hydrophobic solutes onto the oil-water interface (Ch. 3).

**Water's molecular structure.** Understanding specific ion effects can be counterintuitive. Large anions such as iodide have been shown to be equally or even more attracted to hydrophobic parts than to positively charged patches on a hydrophobic sphere[12]. The reason lies again in the structuring of water next to hydrophobic surfaces. When water is only accounted for through its dielectric constant, as in simplified continuum models such as the Debye-Hückel and other Poisson-Boltzmann-based approaches, specific ion effects can never be completely captured[6,48]. One has to account for the detailed molecular structure of water. The

water molecule itself is asymmetric along the direction of its dipole; this results, for example, in charge asymmetries present in many phenomena such as the low isoelectric point of the oil-water interface, the dominance of negative membrane potentials, and the distinct dynamics around positive and negative ions[35,43,49]. In Chapter 5, we address the question of charge asymmetry in bulk and surface hydration by probing anions and cations of virtually identical chemical structure but opposite charge.

## 1.2 Methods

### 1.2.1 Sum frequency and second harmonic generation (SFG, SHG)

Second order nonlinear optical methods are powerful tools to study interfaces and surfaces. They are intrinsically surface-specific in media where the bulk possesses inversion symmetry. Figure 1.2 schematically depicts the process of sum frequency (second harmonic) generation (a) and two experimental realizations: reflection (b) and scattering (c) geometry.

When two input light fields that oscillate at frequencies $\omega_1$ and $\omega_2$ interact with a medium, a polarization, representing locally oscillating dipoles, is induced in the medium. If the input fields are weak, the molecules in the medium respond linearly to the electric fields. However, for strong input fields, such as that of focused femtosecond lasers, higher orders of the interaction potential come into play, generating higher orders of induced polarizations:

$$\boldsymbol{P} = \boldsymbol{P}^{(1)} + \boldsymbol{P}^{(2)} + \dots$$

The linearly induced polarization, i.e. linear with the input fields, explains phenomena such as dispersion and absorption. The second order nonlinear polarization term $\boldsymbol{P}^{(2)}$ is responsible for many nonlinear optical phenomena such as second harmonic and sum frequency generation (SHG, SFG) or optical parametric generation/amplification. In the case of SFG and SHG, which can be seen as a special case of SFG where the two input fields have the same frequency, the nonlinear polarization is given by[51,52]:

$$\boldsymbol{P}^{(2)}(\omega = \omega_1 + \omega_2) = \chi^{(2)} : \boldsymbol{E}(\omega_1)\boldsymbol{E}(\omega_2), \tag{1.1}$$

where $\chi^{(2)}$, the second order susceptibility tensor, represents the (local) nonlinear response of the medium. Because of symmetry properties, the susceptibility vanishes

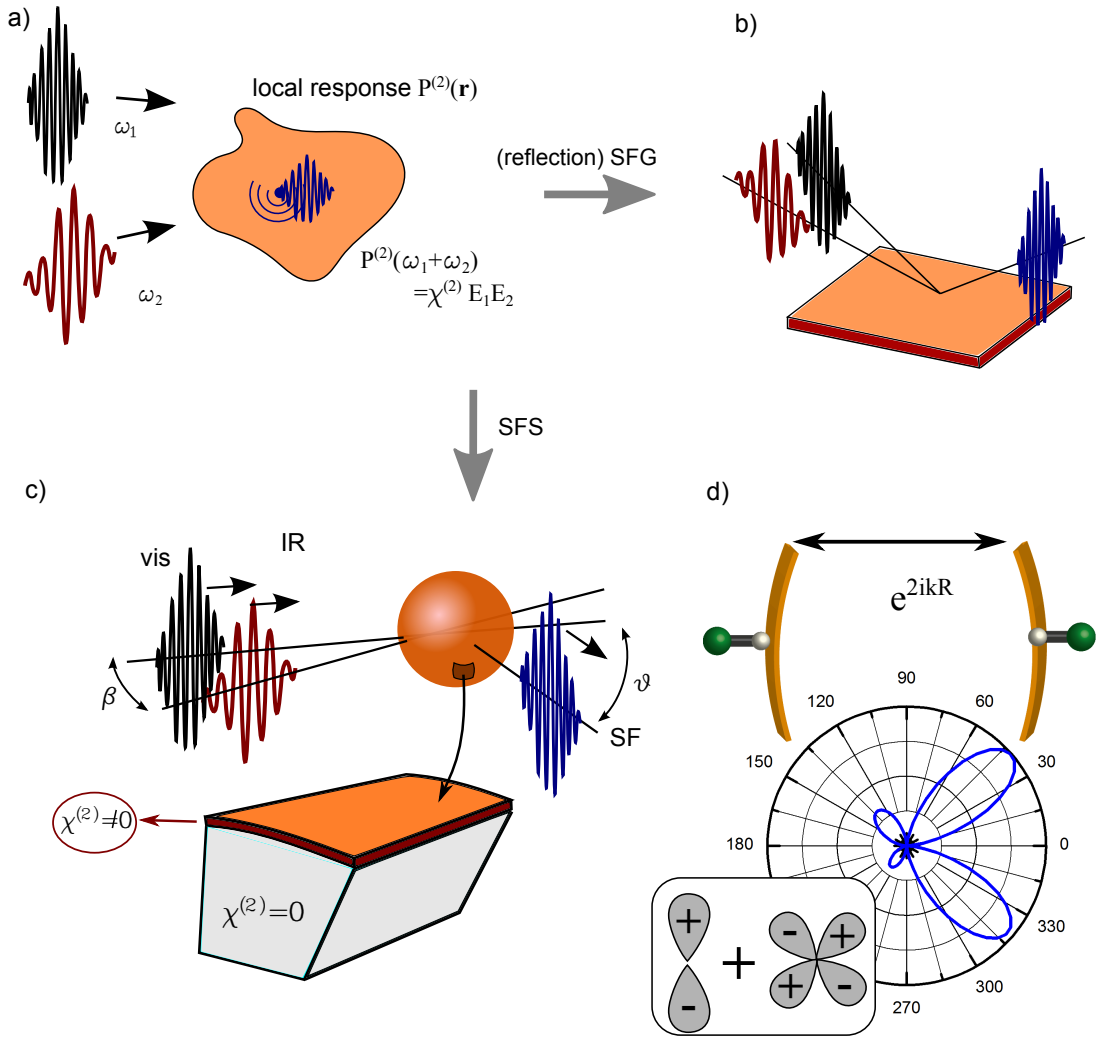


Figure 1.2: (a) 2nd order nonlinear interaction results in a local oscillating polarization $\boldsymbol{P}^{(2)}(\boldsymbol{r})$ that oscillates at the sum frequency $\omega_1 + \omega_2$. The locally induced dipoles either coherently add to yield a reflected SF beam in a reflection SFG experiment (b), or interfere to form a scattering pattern in the case of a small particle (SFS experiment, c). (ad c) IR and visible pulses overlap under an angle $\beta$ on the particle. The polarization is induced only on the surface of the scatterer while the bulk and the surrounding media are assumed to be isotropic and thus sum-frequency-inactive. (d) Angular scattering pattern of spherical particles with a radius of 150 nm for the $CH_2$ symmetric stretch vibration. The angle between visible and IR beams was set to 4°. Calculations are based on Ref. 50. The schematic on top of the angular pattern illustrates how the dipole contribution along the direction of momentum conservation $\boldsymbol{k}_0$ arises: The phase retardation $e^{2ikR}$ breaks the symmetry along $\boldsymbol{k}_0$, resulting in a non-vanishing dipole contribution to the scattered signal. The box on the bottom shows that the typical scattering pattern is a superposition of a dipole emission along $\boldsymbol{k}_0$ and a quadrupole emission.

in centrosymmetric media. This is easily understood, if one recalls that a polar vector such as the polarization or the electric field transforms antisymmetrically under inversion: $\boldsymbol{E} \rightarrow -\boldsymbol{E}$. In an inversion-symmetric medium the response of the medium is invariant under inversion of the coordinate system, i.e. $\chi^{(2)}(-\boldsymbol{r}) = \chi^{(2)}(\boldsymbol{r})$. However, the electric field and the polarization switch signs under this coordinate transform. It therefore follows that the susceptibility vanishes in inversion-symmetric (centrosymmetric) media, $\chi^{(2)}(\boldsymbol{r}) = -\chi^{(2)}(\boldsymbol{r}) = 0$. The given derivation holds in the electric dipole approximation, in which the polarization response is assumed to be local, thus neglecting higher order multipoles in the derivation of the macroscopic Maxwell's equations[53]; in general, the relation of the polarization to the electric fields in (1.1) only holds true in the frequency domain.[†] Hence, quadrupolar bulk contributions to the induced second-order polarization might affect the surface sensitivity of SHG and SFG. However, this contribution is at least an order of magnitude weaker than the dipolar contribution.[56] In particular, for SFG, where the signal originates from localized atomic groups, bulk contributions were shown to be negligible for the monolayers of oriented molecules at the interface[57]. From an experimental point of view, the insensitivity of the spectral shape of measured spectra to the size of the investigated oil droplets, indicates that the bulk contribution is negligible in the observed SF signals. The ratio of surface to bulk molecules scales with the size of the particle; hence, the bulk contribution should increasingly affect the spectra of larger particles. For oil droplets in the size range of $R \sim$80-200 nm, no influence on the spectral shape has been observed.

Isotropic media such as liquids, gases, or amorphous glasses are inversion symmetric and therefore exhibit, as discussed in the last paragraph, no second harmonic or sum frequency response. Nonetheless, density and orientational fluctuations in liquids or gases lead to a non-vanishing instantaneous susceptibility. Since light detectors 'see' the averaged intensity which is proportional to the square of the susceptibility, this results in (incoherent) hyper Rayleigh scattering (HRS), which occurs even in pure liquids[58–60]. In the SH measurements, the data was corrected for this HRS background. In the SF measurements, no such incoherent contribution to the signal has been observed.

The nonlinear susceptibility $\chi^{(2)}$ is the macroscopic average of the molecular

[†]In the time-domain, the polarization is in general a convolution of the electric fields with the susceptibility, $\boldsymbol{P} = \int \chi^{(2)}(\boldsymbol{r}-\boldsymbol{r}', \boldsymbol{r}-\boldsymbol{r}'') : \boldsymbol{E}(\boldsymbol{r}')\boldsymbol{E}(\boldsymbol{r}'')d^3r'd^3r''$. In the lowest order of non-locality, this gives rise to terms of the type $\chi^{(2)} : \boldsymbol{E}\boldsymbol{\nabla}\boldsymbol{E}$[54,55].

second order polarizability $\beta^{(2)\dagger}$. Because an interface breaks the symmetry in the direction normal to the surface, we can often assume that this averaging of molecular properties results in a macroscopic response that is azimuthally isotropic, i.e. $\chi^{(2)}$ has $C_\infty$ symmetry. This particularly means that the response of interfacial molecules only results in macroscopic response if the orientation distribution has a non-vanishing normal component. In other words, molecules that are oriented with their symmetry axis parallel to the surface generate no second harmonic or sum frequency response[61,62].

*Infrared-visible SFG* uses visible and infrared light as input beams, taking advantage of the nonlinear susceptibility being resonantly enhanced if the infrared (IR) electric field frequency matches eigenfrequencies of molecular vibrations. By probing vibrational resonances, we access 'fingerprints' of interfacial molecules, thereby gaining chemical specificity. An excited vibrational resonance decays exponentially in time. The frequency response function, being the Fourier transform of the time response, therefore exhibits a superposition of Lorentzians with linewidths that are inversely proportional to the time decay rates of the vibrational resonances[‡]. When modeling the spectral response of the vibrations, usually a non-resonant contribution is added. This contribution may originate from the substrate of the material in a reflection SFG experiment. For SF scattering the water surface layer adds a non-resonant contribution that can be slightly frequency dependent[31].

$$\chi^{(2)}(\omega) = A_{\mathrm{NR}} e^{i\phi_{\mathrm{NR}}} + \sum_n \frac{A_n \Upsilon_n}{\omega - \omega_n + i\Upsilon_n}$$

Here, $\phi_{\mathrm{NR}}$ is the phase of the non-resonant contribution relative to the resonant part, $\omega_n$ and $\Upsilon_n$ are the frequencies and the damping constants of the vibrations. $A_{\mathrm{NR}}$ and $A_n$ refer to the real amplitudes of the non-resonant contribution and the vibrations, respectively. The amplitudes of the resonances may also be complex and carry a specific phase. This issue has been considered in detail in Ref. 63. However, the main phenomena that may lead to a significant relative phase of the resonances, such as the complex response of a metal substrate (plasmonic resonances), are absent for the samples studied in this thesis. Further, the transformations of the molecular response (hyperpolarizability) to the macroscopic response of the surface and to the effective susceptibility (refer to 1.2.2) are all linear transformations[50] and thus can result in a flip of the sign of resonance amplitudes, but not in complex

[†]Often also called first order hyperpolarizability.

[‡]Inhomogeneous broadening or experimental limitations alter the observed lineshapes, resulting in Gaussian or Voigt profiles.

amplitudes. Experimental influences like a possible chirp or a complex linear response that alter the electric fields have been considered in Chapter 2. The correction for such effects can be done independently from the nonlinear response of the medium represented by its second-order susceptibility.

Generally speaking, SFG fitting is challenging because of the coherent nature of the process. The measured intensity is proportional to the square of the nonlinear susceptibility, $I_{\mathrm{SFG}} \propto |\chi^{(2)}|^2$. Without any restrictions on the fitting parameters, the procedure is not very stable, especially if one also allows the phase of its resonance to vary[63]. To improve the estimation of parameters such as the amplitudes and linewidths of resonances, different approaches have been considered. Mathematical methods such as the maximum entropy method and Fourier filtering techniques[64,65] can help to reduce the number of free parameters and to simplify fitting with a Lorentzian lineshape model. Experimental techniques like phase-resolved SFG[66], measurement of both SFG and DFG[67], and the combination of time- and frequency-resolved measurements[68,69] also facilitate the estimation of the desired parameters. The latter method is applied in Chapter 2, helping to retrieve the relative phases of the resonances in the CH-stretch spectral region. In Chapter 4 the fitting method was used to quantify differences in the amplitudes of the vibrational modes. Those differences are already clear from a visual inspection of the spectra. Moreover, to estimate the differences in amplitudes, linewidths and center frequencies were fixed to reduce the parameter space.

Vibrationally resonant SFG can be viewed as a combined Raman and IR process. Vibrational modes that are SFG-active must therefore be both Raman- and IR-active. The amplitude of a vibration with normal coordinate $q$, which is proportional to the cross-section of the vibrational excitation, is then given by[70]

$$A_{n,ijk} = \frac{\partial \alpha_{n,ij}}{\partial q} \frac{\partial \mu_{n,k}}{\partial q}.$$

Here, $ijk$ refer to the cartesian coordinates, $\alpha_{n,ij}$ is the $(ij)$-component of the Raman polarizability and $\mu_{n,k}$ is the $k$-component of the transition dipole. It is noteworthy that inversion-symmetric media are either IR or Raman-active, reflecting the fact that SFS is forbidden in inversion-symmetric materials.

For *non-resonant SHG*, the second harmonic response depends mainly on the orientational distribution, number densities, and the inherent asymmetries of the electronic orbitals of surface molecules. As is the case for the static dipole moment of a molecule, the second-order molecular polarizability $\beta^{(2)}$ is only non-zero if molecules are asymmetric in the sense that they are non-centrosymmetric.

In some cases a linear dependence of $\beta^{(2)}$ on the static dipole moment can be shown[71]. This explains the relatively high $\beta^{(2)}$ of water compared to alkanes of similar size, e.g. methane. Moreover, in HRS experiments we found the signal strength of water to be about 7 times greater that that of hexadecane. Although interfaces may induce an asymmetric conformation, thereby enhancing the signal from a molecule that is rather centrosymmetric in its conformational ground state, the given reasons strongly indicate that water dominates the SH response. The SH signal from the dispersion of oil in water investigated in this thesis can therefore be attributed mainly to water. Note that the signal from surfaces is proportional to the square of the number densities present at the interface (coherent addition). Amphiphilic and hydrophobic solutes that adsorb to the interface may also give some contribution to the SH signal. However, those molecules are present in much smaller quantities (surface densities). Moreover, most of the molecules studied here have in large parts hydrocarbon structures similar to hexadecane.[†] We thus conclude that the majority of the observed SH signal can be attributed to water. For a coherent addition of the signal originating from water molecules, those have to be oriented anisotropically; this renders SHG (and second harmonic scattering, SHS) a powerful probe of orientational anisotropy of water at interfaces[72,73].

Water ordering can occur because of effects in the surface chemistry, i.e. due to short-ranged interactions of water molecules with the surface molecules. Additionally, some water order can be attributed to the long-range interaction water' dipoles with an electric field generated by surface charges. The latter mechanism gives rise to a third-order process that is proportional to the DC electric field generated by the surface charges[74]. Within this thesis we will not distinguish these two effects since they both lead to an 'ordering' of molecules. In principal one can separate the two effects by reducing the influence of the electric field through a variation of the ionic strength of the solution. An increased ion concentration in the solution screens surface charges more effectively, resulting in a suppression of the water ordering due to the long-range interaction with the surface charges. However, a different ion concentration might also affect the surface chemistry, e.g. through specific ions effects, which is one more reason why we did not distinguish between long-range and short-range interaction-induced order.

[†]An exception are the tetraphenyl salts presented in the last chapter. Here, the $\pi$-electron system of the aromatic rings enhances the nonlinear polarizability of the molecule. As a results, the SHS signal might have some contribution from those adsorbates.

### 1.2.2 Sum frequency and second harmonic scattering (SFS, SHS)

So far, we have only discussed the local second harmonic and sum frequency response. SHG and SFG have been frequently used in reflection geometry. Here, the induced dipoles add coherently to emit a sum frequency beam in the phase-matched direction (Fig. 1.2b). In the scattering geometry, the locally induced dipoles $\boldsymbol{P}^{(2)}(\boldsymbol{r})$ on the surface of a scatterer of isotropic material emit spherical waves that superimpose to form a characteristic intensity distribution in the far field (scattering pattern, Fig. 1.2c,d). Geometrical properties of the scatterer can be included in an effective susceptibility $\Gamma^{(2)}$ to obtain expressions for sum frequency scattering (SFS) that are formally analogous to the expressions for SFG in the literature[62,75]. The intensity of the emitted sum frequency light at a scattering angle $\theta$ then becomes

$$I_{\mathrm{SFS}} \propto \left|\Gamma^{(2)}(\chi^{(2)}, R, \theta) : \boldsymbol{E}_{\mathrm{vis}}\boldsymbol{E}_{\mathrm{IR}}\right|^2 .$$

For a spherical scatterer, $\Gamma^{(2)}$ is related to $\chi^{(2)}$ via form factor functions that depend on the scattering angle and the ratio of the particle radius to the wavelength (as detailed in Refs. 28,50). In the limit of a small spherical particle, the intensity scales as $\sim k_0^6\, R^6$, where $k_0$ is the magnitude of the sum frequency wave vector. The dependence on the wavelength ($\sim 1/\lambda^4$) is by a factor of $1/\lambda^2$ larger than that of linear Rayleigh scattering. The dependence on the size of the scatterer stems from the coherent emission of all molecules at the surface. The intensity is thus proportional to the square of the number of surface molecules ($\sim R^4$). The additional factors of $\sim R^2$ and $\sim k_0^2 = 1/\lambda^2$ arise because of a higher order effect, as discussed in the following paragraph.

It is insightful to consider the origin of the SHS and SFS response from a centrosymmetric particle. The pure dipole contribution vanishes because of the selection rules mentioned before. However, because of the finite size of particles, the retardation of the pump beam results in a phase difference $e^{2ik_0R}$ of the excited dipoles along the propagation direction of the incoming beams (see Fig. 1.2d). Hence, this retardation alters the complete canceling of the induced dipoles on the surface of the particle and generates a dipolar emission with scattering pattern corresponding to a dipole that is oriented along the direction of momentum conservation $\boldsymbol{k}_0 = \boldsymbol{k}_{\mathrm{vis}} + \boldsymbol{k}_{\mathrm{IR}}$. This intensity contribution is, however, by a factor of $k_0^2R^2$ smaller than would be the pure dipolar excitation/emission process. The quadrupolar emission term therefore becomes of the same order as the former dipolar term.

Hence, the resulting scattering pattern is a superposition of a quadrupole emission and a 'longitudinal' dipole emission. A typical scattering pattern calculated using the theory presented in Ref. 50 for a particle with a radius of 150 nm is shown in Fig. 1.2d. The appended sketch shows how the scattering pattern results from the superposition of the dipolar and quadrupolar scattering fields.

### 1.2.3 Solute-correlated Raman spectroscopy

In a collaboration with Dor Ben-Amotz's group at Purdue University, solute-correlated Raman spectra of ions and amphiphiles in aqueous solution have been measured. The technique combines linear Raman spectroscopy with multivariate curve resolution[77] (Raman-MCR) and is essentially an advanced type of a difference spectroscopy. Figure 1.3 displays the measurement principle. From the measurement of the sample that contains the solutes and of the pure solvent (water), Raman-MCR allows deconvoluting the measured sample spectrum into a solute-correlated spectrum and the bulk (non-solute-correlated) spectrum. The solute-correlated spectrum contains spectral features from the solute, such as the C-H vibrations of a hydrocarbon, and the O-H spectrum of water molecules that are perturbed by the presence of the solute[78,79].

The decomposition of mixture spectra (typically 4 to 8 spectra) contained in a data matrix $D$ into the spectra of the pure components (solute perturbed, $S_{\mathrm{SP}}$, and solvent, $S_{\mathrm{sol}}$) with concentrations $c_{\mathrm{SP}}$ and $c_{\mathrm{sol}}$

$$D = \boldsymbol{c}_{\mathrm{SP}} S_{\mathrm{SP}} + \boldsymbol{c}_{\mathrm{sol}} S_{\mathrm{sol}} \tag{1.2}$$

is performed with self-modeling curve resolution (SMCR). SMCR has widely been applied since it had been introduced by Lawton and Sylvestre[77]. It requires a bilinear data structure and some knowledge about the pure component data such as non-negativity[80]. The latter holds true for Raman-MCR because of the inherent incoherence of the scattering process. A bilinear data structure, i.e. a linear decomposition of mixture spectra into $S_{\mathrm{SP}}$ and $S_{\mathrm{sol}}$ as given in equation (1.2), can be assumed if the spectral components can be thought of originating solely from molecules in the hydration shells or in the unperturbed bulk solution. In such a model, the water structure around solutes is simplified since the water structure changes rather gradually from the water molecules in the first hydration shell to those molecules that recover the properties of bulk water. Exchange dynamics between unperturbed water and hydration shell water might also inhibit the linear decomposition; however, such dynamics would occur on time scales characteristic

a)

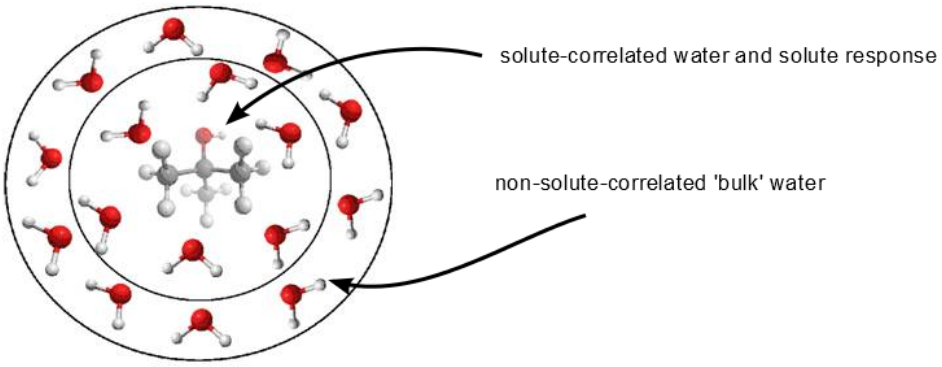


b)

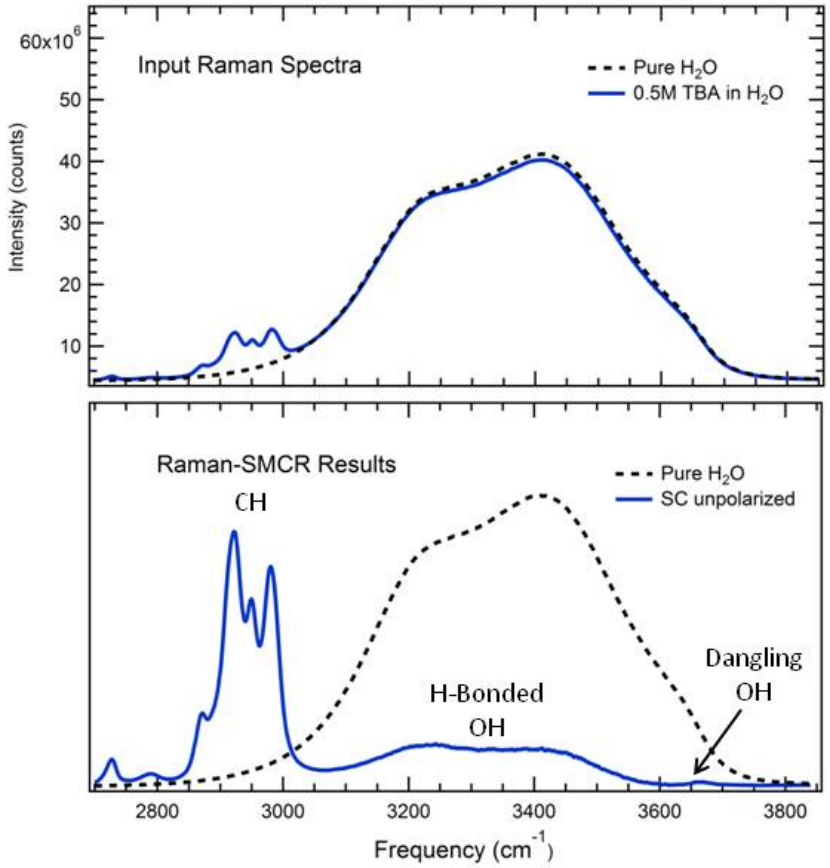


Figure 1.3: Principle of solute-correlated Raman spectroscopy. (a) Water molecules around solutes are perturbed and thus have a response that is different from the response of bulk water. (b) Using the background measurement of the pure solvent (water), self-modelling curve resolution is used to extract the solute-correlated (SC) spectrum (blue, lower graph, here for tert-butyl alcohol (TBA))[76].

to rotational and translational motion which are much longer than the relaxation of the O-H oscillators probed by Raman-MCR. The bilinear model therefore captures the essential effects induced by the solute molecules on the hydration shell solvent molecules. The unpolarized Raman spectrum of the solute-perturbed O-H oscillators, as depicted in the lower graph in Fig. 1.3b (blue curve), marks differences with respect to the bulk water structure. The interpretation of the water O-H band, in particular the two lobes at $3200\,\mathrm{cm}^{-1}$and $3450\,\mathrm{cm}^{-1}$, is intricate; coupling of O-H vibrators lead to the feature at lower frequencies which occurs largely pronounced in Raman spectra compared to IR spectra[81]. An enhancement of the lower frequency lobe can roughly be associated with more tetrahedrally ordered water structures, as indicated by calculations[82] and experimental results of for ice[83]. In the example in Fig. 1.3b, the presence of the solute TBA (tert-butyl-alcohol) results in a greater spectral density at lower frequencies and therefore indicates an enhanced tetrahedral ordering of water molecules around TBA solutes.

### 1.2.4 Dynamic light scattering and zeta potential

In our experiments, we used dynamic light scattering (DLS) and zeta potential measurements to characterize the size and the charge of the colloids, respectively.

#### Dynamic light scattering, DLS

DLS used linear light (back) scattering to measure the intensity autocorrelation function of the sample dispersion. Theoretical modelling allows to extract the diffusion coefficient $D$ of the dispersed particles[84]. The Stokes-Einstein relation is then used to calculate the *hydrodynamic radius* taking the viscosity $\eta$ of the solvent and the temperature $T$ as input parameters:

$$R = \frac{kT}{6\pi\eta D}$$

#### Zeta potential

Charged particles in an ionic solution attract ions of opposite charge towards the surface. An electric double layer with immobilized ions in a Stern layer and 'free' ions in a diffuse layer is formed. These ions decrease the influence of the surface charges, they screen the electrostatic potential. When the charged particle moves, certain layers around the particle are dragged with the particle and firmly attach to the surface. At a certain distance from the surface ions in the diffuse layer do not move with the particle anymore. The boundary is called the hydrodynamic shear or slipping plane (see also Fig. 1.4). The electric potential at this boundary is called

the *zeta potential* $\phi_\zeta$. The zeta potential is a common measure for colloidal stability. Under the influence of an electric field, the charged particle accelerates towards the

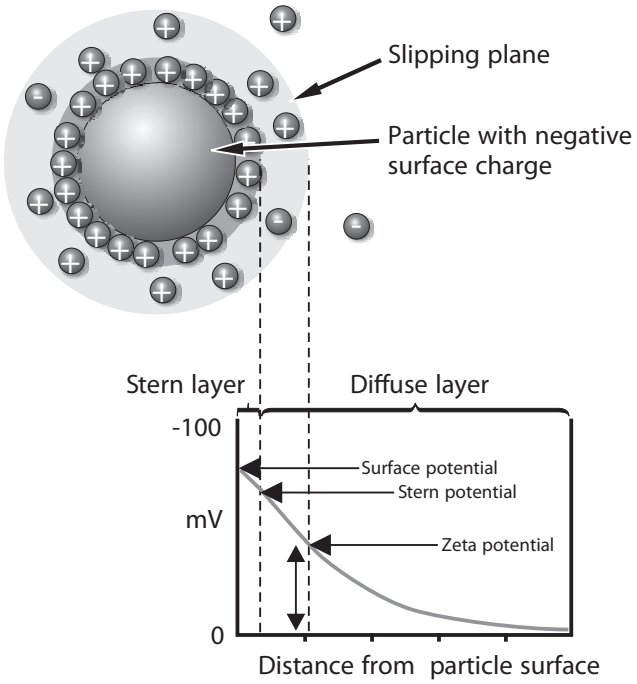


Figure 1.4: Concept of the zeta potential. Adapted from Ref. 85

electrode of opposite polarity. Viscous forces (basically 'friction') counteract the accelerating force resulting in a movement at constant velocity. This phenomenon is called electrophoresis. The electrophoretic mobility $\mu_e$ relates the velocity to the external electric field,

$$\mu_e = \frac{v}{E_{\text{ext}}}.$$

The mobility is connected to the zeta potential. They can be related by Henry's equation[86],

$$\mu_e = \frac{2\varepsilon\phi_\zeta f(\kappa a)}{3\eta}. \tag{1.3}$$

Here, $\varepsilon$ is the dielectric constant and $\eta$ the viscosity of the solution. The function $f(\kappa a)$ is called Henry's function and depends on the ratio of the particle size $a$ to

the Debye screening length ($\kappa^{-1}$). Even though the relation of the zeta potential to the interfacial charge is rather complicated and involves models such as the Gouy-Chapman model[87], the zeta potential can in some cases be used as an estimate to compare surface charge densities. For instance, for particles in solutions with identical ionic strength (concentration of ions), an equal zeta potential indicates equal surface charge densities. To obtain zeta potentials from equation (1.3), the Smoluchowski approximation ($f(\kappa a) = 1.5$), which assumes a 'thin' double layer, is useful; it assumes the size or the particle to be large compared to the extent of the double layer given by the Debye length. The Smoluchowski approximation is a good approximation in the case of aqueous solutions with particles/droplets in the $\sim 100\,\text{nm}$ size range. For example, in solutions with ionic strengths of 10 to 100 mM, the Debye length is about 3 to 1 nm (at room temperature), rendering the approximation of a thin double layer quite reasonable.
Zeta potential measurement and size measurements were performed with a commercial device (Malvern ZS Nanosizer). For size measurements, the z-average size and the polydispersity index (PDI) are obtained from the intensity auto-correlation[84]. For zeta potential measurements, we used the above-mentioned Smoluchowsky approximation to obtain zeta potentials from electrophoretic mobilities.

## 1.3 Experimental details

### 1.3.1 Sample preparation

To finely disperse oil droplets in aqueous solution, we used the following typical procedure. 0.05-2 vol% of oil in an aqueous ($D_2O$) solution that contains the desired amphiphile and salt concentrations were mixed in a small vial (3-6 ml) using a hand-held homogenizer (TH, OMNI International) for ∼1 minute. The homogenizer consists of a motor driven tip that spins inside a fixed plastic tube. The tip and the tube were immersed in the vial containing the oil and the water. The homogenizer can be used with angular velocities varying between 5 an 35 rpm. When working with amphiphiles, only small velocities are necessary while the fastest setting is needed to obtain suitable dispersions with only oil and water. This procedure produces an emulsion with droplets in the micrometer size range. To reduce the droplet size further, the samples were ultrasonicated (35 kHz, 400 W, Bandelin) for 2-5 minutes. Using this methodology, typical size distributions with a mean radius in the range of 70-150 nm (radius) were obtained. Since the size distribution cannot be rigorously controlled by this method, we used a common stock dispersion in measurement series that demanded a comparison of absolute

signal amplitudes. Samples were then prepared by diluting the stock dispersion with aqueous solutions of amphiphiles and salts to obtain samples with the desired concentrations.
In SFS experiments, 1-2 vol% of oil were used whereas lower volume fractions (0.05% to 0.2%) were used for SHS and zeta potential measurements.

### 1.3.2 Time-domain and frequency-domain SFS

Our experimental setup, which can be used to measure both time- and frequency resolved SFS signals, is based on a femtosecond Ti:Sa amplifier system (Spitfire, Spectra Physics) producing pulses at a wavelength of 800 nm (pulse length 90 fs, pulse energy 7 mJ, repetition rate 1 kHz). The majority of the pulse energy is used to drive an optical parametric amplifier (OPA, He-Topas, Light Conversion) that ultimately produces tunable infrared pulses (2.5-15 $\mu$m, 1-120 $\mu$J) by difference frequency generation. The second beam (VIS) for the SF generation is derived from the fundamental amplifier output. A combination of a grating and a mechanical slit were used to control the pulse length and the bandwidth of the VIS pulses (compare Fig. 1.5a).

SFS spectra were measured using the broadband IR laser pulses centered at $\sim$2900 cm$^{-1}$ or $\sim$1050 cm$^{-1}$(120 cm$^{-1}$ FWHM bandwidth) and VIS pulses at 800 nm (FWHM bandwidth of 12 cm$^{-1}$). IR and VIS pulses were focused with a parabolic gold mirror (f=50 mm) and a plano-convex lens (f=125 mm), respectively. The beams were overlapped under an angle of $\beta = 20°$ in a sample cuvette ($CaF_2$ and quartz windows, path length = 100-200 $\mu$m) containing the aqueous droplet dispersion. The beam waist of the VIS beam was placed slightly behind the sample cuvette to match the diameter of the VIS beam to the beam waist of the IR pulse. At an angle of $\theta = 60°$ with respect to the direction of momentum conservation, the scattered SF light was collimated with a plano-convex lens (f=15 mm, Thorlabs LA1540-B) and then passed through two short wave pass filters (3rd Millenium, 3RD770SP). The SF light was spectrally dispersed with a monochromator (Acton, SpectraPro 2300i) and detected with an intensified CCD camera (Princeton Instruments, PI-Max3) using a gate width of 10 ns. A Glan-Taylor prism (Thorlabs, GT15-B), a half-wave plate (EKSMA, 460-4215) in combination with a polarizing beam splitter cube (CVI, PBS-800-050), and two $BaF_2$ wire grid polarizers (Thorlabs, WP25H-B) were used to control the polarization of the SF, VIS, and IR beams, respectively (compare also Fig. 1.5b). Spectra were typically collected with an acquisition time of 150 s. To control the stability of the laser system, a reference sample was measured in between every

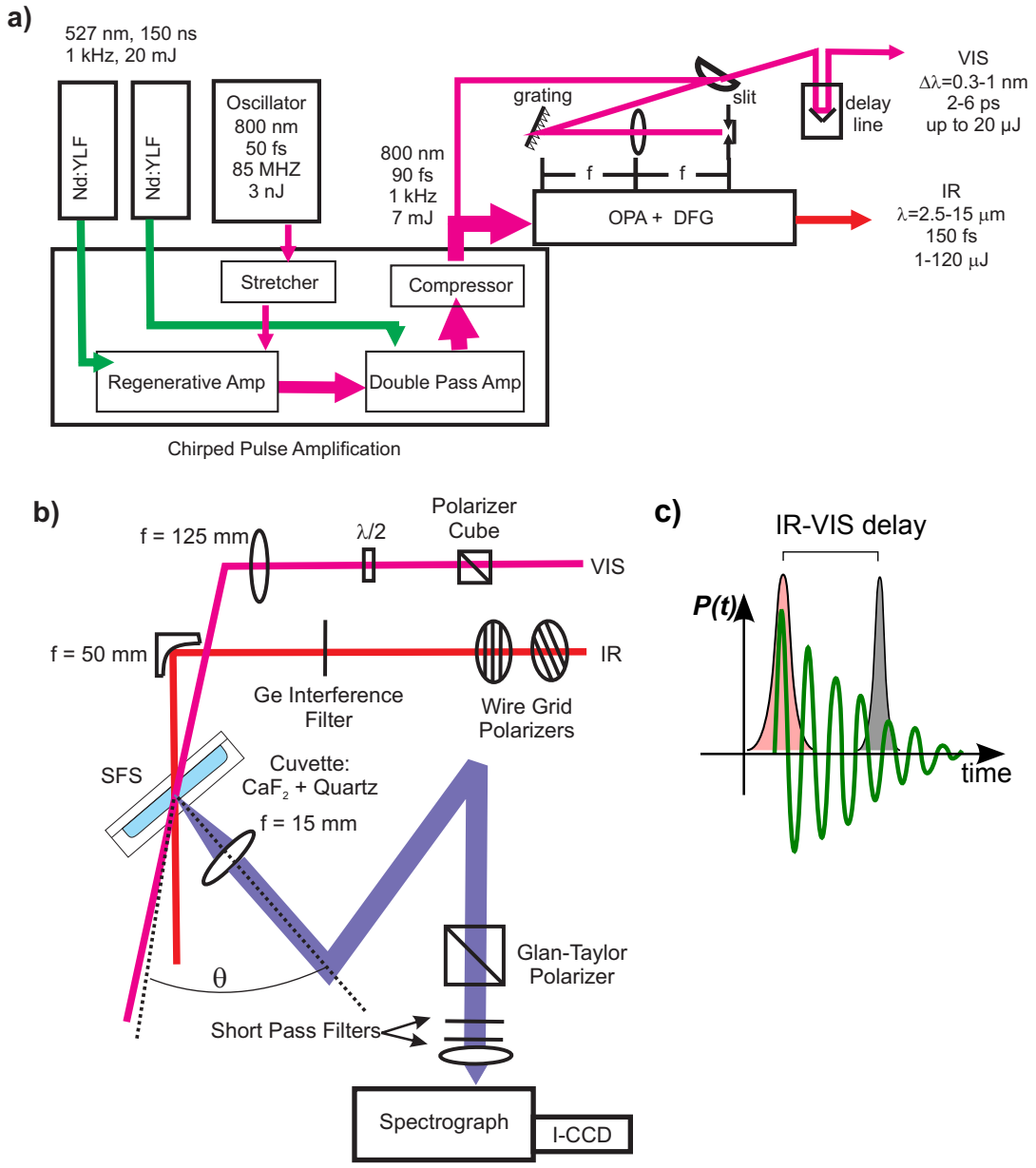


Figure 1.5: (a) **Schematic of the Ti:Sa laser system:** IR pulses are generated from a white-light seeded OPA pumped by the fundamental output of a chirped pulse Ti:Sa amplifier system. Signal and idler output of the OPA generate IR pulses with up to 120 $\mu$J by DFG. (b) **Schematic of the SFS experiment:** IR and VIS pulses are overlapped non-collinearly and the generated SFS radiation is collected, polarization analyzed, spectrally dispersed, and detected with an ICCD camera. (c) Temporal order and induced nonlinear polarization in a time-resolved SFS experiment.

sample in a series of measurements. This reference sample was a 2 vol% dispersion of deuterated hexadecane oil droplets in an aqueous solution of 10 mM of sodium dodecyl sulfate (SDS) in $D_2O$.

Time-resolved data was measured with the same setup as described in the previous paragraph, but using both broadband IR and broadband VIS (FWHM 185 $cm^{-1}$) pulses. Here, the IR-VIS delay time was controlled with a retro-reflector mirror mounted on a stepper-motor-driven translation stage (Thorlabs, LTS300). To probe the dephasing of the molecular vibrations, we employed the time-domain free induction decay (TD-FID) scheme previously described in Refs. 88–90. A fs IR pulse first creates a vibrational coherence, i.e. a first order polarization in the sample, which in turn is upconverted by a delayed short visible pulse. The upconversion results in the emission of SF photons that are scattered into the detector (see schematic (c) in Fig. 1.5 and schematic (c) in Fig. 1.2). For FID traces, the intensity on the iCCD was integrated and several scans of the time delay with time steps set between 30 and 100 fs were averaged.

**Normalization of SFS spectra**

To obtain the frequency-domain response of the sample, i.e. $|\Gamma^{(2)}|^2$, the following procedure was used:

1. Spectra were background-corrected for the dark pattern and background noise.

2. The spectral intensities (CCD counts) were divided by the acquisition time (in s) and the pulse energies of IR and VIS pulses (in $\mu$J).

3. The spectra were divided by the spectrum of the IR pulse, which was obtained from a reflection SFG experiment of a reference substrate (z-cut quartz for the CH-spectral region and gold for the spectral fingerprint region).

All SFS spectra labeled as 'normalized' have been processed in this way. From the given procedure, it is clear that the normalized spectra can be compared in spectral shape. The total amplitude is, however, not only affected by the acquisition time and the pulse energies, but also by e.g. the spatial overlap of the beams and the efficiency of the collection of the scattered light. The absolute scale of the normalized spectra therefore only allows for a rough comparison of the total scattering cross section of the sample. Yet, *all samples within a given measurement series can be compared in both amplitude and shape*. The stability of the system was controlled through the reference sample measured in between every sample in

the series (see above). In this thesis, unless stated otherwise explicitly, all spectra shown in one graph have been measured in one measurement series to allow for a comparison of both amplitude and spectral shape.

**Influence of the sample.** Different preparations of sample dispersions with the same chemical composition can be compared with DLS, allowing a comparison of the particle size. However, the absolute number of droplets can vary between different preparations, since the complete portion of oil may not be dispersed in small droplets. Because no multiple scattering is observed for samples with a vol% of less than 1-2 %, this difference in the particle number only affects the total amplitudes, but not the spectral shape of the spectra. All spectra shown in one graph have therefore been prepared with a common stock solution to allow for a comparison of the total spectral amplitude. For the range of particle sizes used in the experiments ($R$ = 80-170 nm), different particle size distributions do not affect the relative amplitudes of the vibrations; this has been confirmed by measuring different preparations of the reference sample with varying particle size distributions. Consequently, the normalized spectra of different samples can be compared in spectral shape which allows drawing conclusion about the surface chemistry.

### 1.3.3 Second harmonic scattering (SHS)

The SHS experiments were performed with a pulsed Yb:KGW femtosecond laser system (Light Conversion) that delivers 190 fs light pulses with a center wavelength of 1028 nm at a repetition rate of 200 kHz. The polarized beam was focused with a plano-convex lens (f = 75 mm) into a cylindrical glass sample cell (4.2 mm inner diameter). The typical power at the sample was 10-50 mW. The scattered SH light was collimated with a plano-convex lens (f = 50 mm) and then sequentially passed through an iris to control the angular resolution and a bandpass filter that is centered at 525 nm. The polarization state was analyzed with a polarizer cube. The filtered SH light was focused into a photomultiplier tube (PMT) with a plano-convex lens (f = 30 mm). The signal from the PMT was analyzed with a gated photon counter (Stanford, SR400) whose gate width was set top 10 ns. The typical acquisition time was 1 s per measurement angle. The SH signals were measured at a scattering angle of 35° with an angular resolution of ±1.75°. The measured signal was corrected by subtracting the hyper Rayleigh scattering background of the solution without any particles of droplets at the same angle and polarization combination. The data was then normalized to the signal of pure water in ss

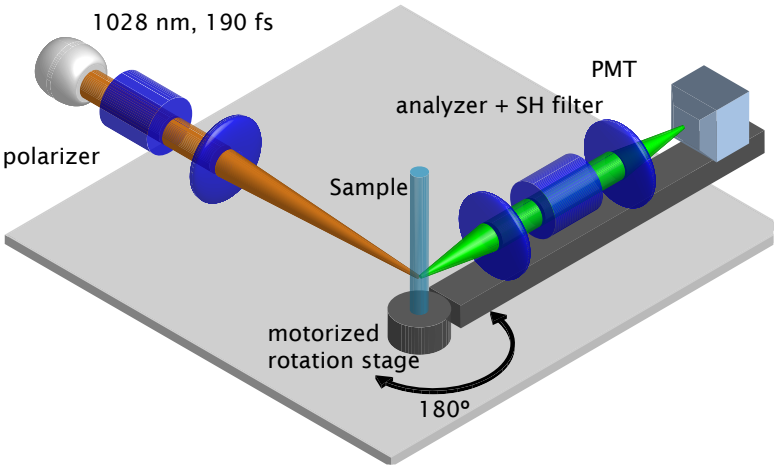


Figure 1.6: **Schematic of the SHS setup:** The incident pulses at a fundamental wavelength of 1028 nm are polarized and focused into the cylindrical sample cuvette. The scattered light is collected and the polarization state is analyzed. A band pass filter centered at 525 nm blocks the scattered fundamental light. SH photons are detected with a PMT that is connected to a photon counter.

polarization combination. The plotted data points represent an average of 20-30 measurements, each with an acquisition time of 1 s. The typical error of the mean was 1-2% for aqueous solutions and 3-6% for the used droplets solutions. The latter number reflects the uncertainty in the reproducibility of the preparation of the droplet solutions.

### 1.3.4 Solute-correlated Raman spectroscopy

Raman spectra were collected using an Ar-ion laser (514.5 nm) as the excitation source with approximately 15 mW of power at the sample. Two to four spectra were collected with an integration time of five minutes for each the sample and the pure solvent. The back-scattered Raman photons were collected and delivered at the entrance slit of a 300 gr/mm-grating using a fiber bundle consisting of seven 100 $\mu$m core diameter fibers (arranged in a close packed circular array at the collection end and a linear stack at the entrance slit). The spectral resolution of the Raman system is $\sim$1 nm ($\sim$25 cm$^{-1}$ or $\sim$25 CCD pixels), as determined from the FWHM of isolated neon calibration lamp lines measured using the same collection fiber-bundle and detection system. All Raman spectra are unpolarized (i.e. they include both S and P polarized scattering). The Raman-MCR decomposition of measured spectra into SC and pure water components was performed using Self-Modeling Curve Resolution (SMCR)[77]. Although SMCR is limited to two component systems,

we have previously shown that multi-component systems can be reduced to two components by varying the concentration of only one component [91]. The strategy has been used here by including the same $Br^-$ concentration in both solvent (as $Na^+Br^-$) and $OTA^+$ surfactant solutions (as $OTA^+Br^-$). Note that the OH band of water molecules around $Na^+$ ions is virtually indistinguishable from that of pure water [78] and thus $Na^+$ ions have essentially no influence on the SC spectra.

# 2 Towards vibrational dynamics at liquid-liquid and nano-interfaces: Time-resolved Sum Frequency Scattering

*Interfacial molecular dynamics are key to understanding many phenomena in technology and life sciences. We demonstrate a first step towards the vibrational dynamics at liquid-liquid and nanoscopic (bio)-interfaces, measuring the free induction decay of vibrational modes of dodecylsulfate amphiphiles. We probed the vibrational response of both the functional head group and the alkyl tail. In the molecular fingerprint region, a beating of vibrational modes was observed. Simultaneous fitting revealed modes at* $\sim 995\,cm^{-1}$ *and* $\sim 1065\,cm^{-1}$ *that can be assigned to -C-O-S and* $SO_3$ *stretch vibrations.*

## 2.1 Introduction

Time-resolved femtosecond vibrational spectroscopy is a valuable tool to study condensed phases. It provides information on the structure and dynamics of molecules on time scales relevant for many biological and chemical processes[92]. Particularly important are the structure and dynamics at interfaces[21,93] because they play a key role in phenomena such as molecular transport, catalysis, or self-assembly. Moreover, the dynamics at interfaces often greatly differ from the bulk dynamics; for example, water reorientation is much faster at the water surface than in the bulk[94].

Interfacial relaxation dynamics can be revealed by time-domain vibrational sum frequency generation (SFG)[95,96]. In particular, SFG free induction decay (SFG-FID)[88,90] techniques that probe the dephasing of vibrational modes have been employed to study adsorbates at metal interfaces[89,97,98], water at the $D_2O$-$CaF_2$ interface[99] as well as Langmuir-Blodgett and self-assembled monolayers[68,69]. While SFG is thus extremely powerful in elucidating dynamics at a variety of interfaces, its application has been restricted to macroscopically planar surfaces. However, many biologically and chemically important interfaces such as those of proteins, vesicles, and colloids are structured on the nanoscale. To access them, SFG can be combined with light scattering techniques, thereby extending its application to nanoscopic systems and aqueous dispersions. Sum frequency scattering (SFS) has thus been used to study the stucture of nanoscopic colloidal particles, liquid nano-droplets, and catanionic vesicles[29,30,90]. SFS also has the advantage that it facilitates the measurement of liquid-liquid interfaces and that it is less prone to impurities because of the large surface-to-volume ratios in nanoscopic dispersions[32,33]. Extending SFS to the time domain would be key to access the dynamics of molecules at nanoscopic biointerfaces, liquid-liquid and nanoparticle interfaces.

Here, we demonstrate a time-resolved sum frequency scattering (TD-SFS) experiment. We recorded the free induction decay (FID) of vibrational modes from the interface of dispersed nanoscopic oil droplets in aqueous solution. We probed the vibrational response of both the head group and the alkyl chain of the amphiphiles that stabilize the dispersion. In the molecular fingerprint region around $\sim 1000\,\mathrm{cm}^{-1}$, we observed a beating on the time-domain signal, indicating that two sum-frequency-active modes coherently interfere; the symmetric stretch mode of the $SO_3^-$ head group and another mode that we tentatively assign to a C-O-S stretch vibration.

## 2.2 Materials and Methods

**Sample preparation.** Dispersions of oil droplets in water were prepared with 1 v/v% of deuterated hexadecane (d-$C_{16}$) in solutions of 10 mM of sodium dodecyl sulfate (SDS) in $D_2O$ (compare 1.3.1). The size distribution of the droplets was measured with dynamic light scattering and laser Doppler electrophoresis (Zetasizer Nano ZS, Malvern). d-$C_{16}$ (98% d, Cambridge Isotope), SDS(99%, Biomol), and $D_2O$ (99%, Sigma-Aldrich) were used as received.

### 2.2.1 Sum frequency scattering setup

Time- and frequency-resolved SFS measurements were performed as described in Chapter 1.3.2. To determine the time resolution of our system, we measured the frequency-resolved IR-VIS SF cross-correlation (XFROG) from a gold substrate, which is analogous to a FROG measurement[100]. We overlapped IR and VIS beams under an angle of 20° on the substrate. The incident angles of the beams with respect to the surface normal were 40° and 60°. The generated SF beam was collimated and then detected in the same way as the scattered light in the scattering geometry (refer to 1.3.2). Figure 2.1c shows the SF spectrum as a function of the IR-VIS delay time (XFROG-trace). The shape of the XFROG trace is almost perfectly spherical; this confirms that IR and VIS pulses are not chirped. A conventional cross-correlation was obtained by integrating the XFROG trace over all frequencies. The retrieved almost perfectly Gaussian IR-VIS cross-correlation (FWHM of 220 fs) represents the instrument response function (Fig. 2.1d). This instrument response, however, underestimates the time resolution of the measurement; the geometry used for the XFROG trace introduces a lengthening of the cross-correlation due to the non-collinear geometry. The geometric lengthening can be described by a Gaussian transfer function with FWHM of 100 fs. This estimate is based on the beam geometry described above and the overlapping area that is mainly determined by the focus size of the IR beam ($\sim$70 $\mu$m). In the scattering geometry, we used a sample cuvette that is placed such that its entrance and exit windows are tilted by 45° with respect to the IR beam. Because of refraction at the air/$CaF_2$/water interface, the effective overlapping angle $\beta$ is reduced to $\sim$ 6° inside the sample cell. This reduction improves the time resolution of the experiment, ultimately yielding a resolution of $\sim$ 200 fs. For the experiments in the spectral fingerprint region around 1000 $cm^{-1}$, the IR pulse becomes chirped because $D_2O$ is more dispersive in that frequency region, particularly on the red frequency side of the spectral range of the measurements[101]. This would lead to a reduced time resolution in

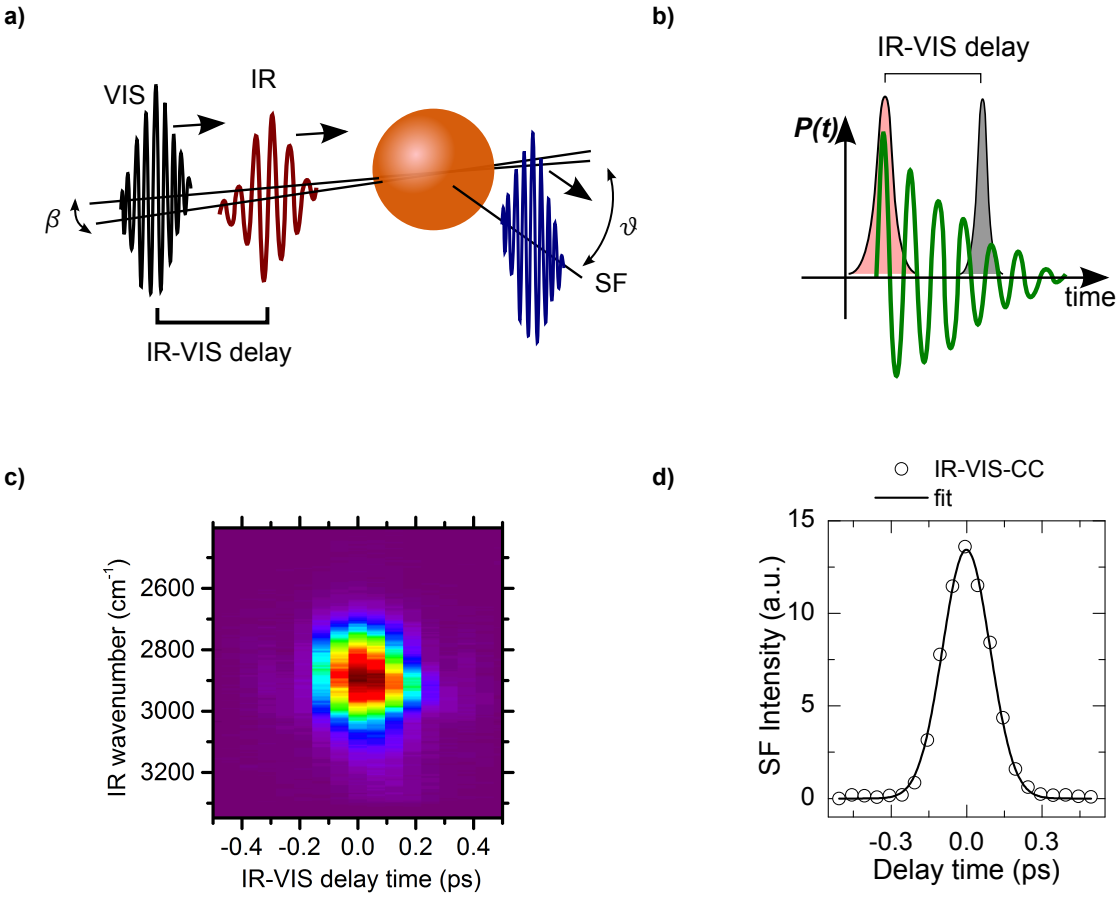


Figure 2.1: (a) Scheme showing the arrangement of fs pulses in the time-resolved sum frequncy scattering experiment. (b) Scheme showing the temporal order of the IR (red) and VIS (grey) pulses and the induced polarization (green).(c) Frequency-resolved cross-correlation (XFROG) of IR and VIS pulses and (d) spectrally integrated IR-VIS cross-correlation from a gold substrate in reflection (ppp polarization combination)

the spectral fingerprint region. However, we can utilize the input $CaF_2$ window to partly cancel the lengthening of the IR pulse: Whereas the $D_2O$ group velocity dispersion is normal, i.e. $n''(\omega) > 0$, the $CaF_2$ window is anomalously dispersive, i.e. $n''(\omega) < 0$. To estimate the true instrument response in the spectral fingerprint region, it is best to fit the rise time of the signal in the scattering experiments. We thus found that the time resolution is $\sim$270 fs in the $\sim$1000 $cm^{-1}$ region.

### 2.2.2 Modelling of the time and frequency domain response

The response of the sample can be described with TD and FD response functions [102]. For the employed TD scheme (Fig. 2.1b) and the samples studied here, the sample

response is only resonant to the IR light. Its response function can therefore be modeled as a superposition of exponentially decaying oscillators[68,69,90] and an instantaneous (non-resonant) contribution:[†]

$$R^{(2)}(t) = A_{\mathrm{NR}} e^{i\phi_{\mathrm{NR}}} \delta(t) - i\Theta(t) \sum_j A_j \exp\left(-i\omega_j t - \Upsilon_j t\right) + c.c.$$

Here, $\phi_{\mathrm{NR}}$ is the phase of the non-resonant contribution relative to the resonant part, $\delta(t)$ is the Dirac delta function, and $\Theta(t)$ is the Heavyside step function. $\omega_j$ and $\Upsilon_j$ are the frequencies and the damping constants of the molecular vibrations. $A_j$ and $A_{\mathrm{NR}}$ are the real amplitudes of the vibrational and non-resonant response. The corresponding frequency domain response function

$$\chi^{(2)}(\omega) = A_{\mathrm{NR}} e^{i\phi_{\mathrm{NR}}} + \sum_j \frac{A_j}{\omega - \omega_j + i\Upsilon_j}$$

is the Fourier transform of $R^{(2)}(t)$. While the complex response functions in the time and frequency domain are each others Fourier transform, the SFS signal obtained from the time- and frequency resolved measurements possesses complementary information; the difference in the experimental schemes, e.g. the different pulse shapes of the VIS pulse, render the two measurement types sensitive to distinct properties of the sample response. This advantage of the combined measurement in the TD and FD is discussed in Section 2.3.

The locally induced polarization at the droplet surface for a certain IR-VIS delay time $\tau$ is given by

$$P^{(2)}(t,\tau) = E_{\mathrm{VIS}}(t-\tau) \int_{-\infty}^{\infty} E_{\mathrm{IR}}(t-t') R^{(2)}(t') dt',$$

For a scattering geometry, the locally induced polarization $P^{(2)}$ has to be integrated over the surface of the particle. By introducing an effective susceptibility, the influence of the particle size and geometry can be captured and an expression formally analogous to planar SFG can be retrieved[75]. Although, the effective nonlinear susceptibility/response function is necessary for calculations of scattering patterns and the intensities in different polarization combinations, the time-dependence of the SFS signal is simply proportional to the time integral of the squared induced

[†]This model assumes that inhomogeneous broadening, e.g. due to environmental effects, is negligible. In particular in the region of 2890-2930 $\mathrm{cm}^{-1}$ this does not completely describe the broad Fermi bands in that spectral region. (See also the discussion in Section 2.3)

polarization

$$I_{\mathrm{SFS}}(\tau) \propto \int_{-\infty}^{\infty} \left|P^{(2)}(t,\tau)\right|^2 \, dt.$$

For the frequency-resolved experiment, the measured intensity at the sum frequency $\omega_{\mathrm{SF}}$ is given by[68†]

$$I_{\mathrm{SFS-FD}}(\omega_{\mathrm{SF}}) \propto \left| \int_{-\infty}^{\infty} E_{\mathrm{VIS}}(\omega_{\mathrm{SF}} - \omega_{\mathrm{IR}}) E_{\mathrm{IR}}(\omega_{\mathrm{IR}}) \chi^{(2)}(\omega_{\mathrm{IR}}) d\omega_{\mathrm{IR}} \right|^2$$

To describe the data, we assumed Gaussian pulse shapes for the electric field of the VIS and the IR pulses,

$$E(t) = \frac{1}{2}\mathcal{E}(t)e^{-i\omega_0 t} + c.c. = \frac{1}{2\pi}\int_{-\infty}^{\infty} E(\omega)e^{-i\omega t}d\omega$$

with $\mathcal{E}$ being a complex amplitude that models the temporal shape of the Gaussian pulse with pulse length $\tau = \tau_{\mathrm{FWHM}}/2\sqrt{\log 2}$, and a possible chirp which is described by the chirp parameter $a$[103],

$$\mathcal{E}(t) = \mathcal{E}_0 e^{-(1+ia)(t/\tau)^2}.$$

The pulse lengths of VIS and IR pulses were estimated from the autocorrelation of the VIS pulse and the IR-VIS cross-correlation measured with a non-resonant gold substrate. The retrieved values were used as input parameters to fit the spectrum and the FID simultaneously by adjusting the amplitudes, center frequencies and damping constants of the resonances mentioned in Section 2.3. We additionally introduced the linear chirp described by $a$ as a fitting parameter to account for a possible chirp due to the dispersion of $D_2O$ and $CaF_2$. To estimate confidence intervals for the parameters, we used a bootstrapping method[104]. This method essentially repeats the fitting process for a certain number of runs using the data with an additional normal-distributed random noise added to it. The confidence intervals were estimated by the standard deviation of the resulting fit parameter distribution which was obtained by fitting 2000 such noise-modified data sets for each of the fit parameters, i.e. the resonance frequencies, linewidths and amplitudes.

[†]Note that Parceval's theorem tells us that $\int |P(t)|^2 dt = \int |P(\omega)|^2 \frac{d\omega}{2\pi}$. The frequency-resolved experiment accesses $|P(\omega)|^2$, the Fourier transform of $|P(t)|^2$. When switching the domain, a product becomes a convolution an vice versa; from this follows that the FD signal is a convolution of the VIS electric field with the product of the IR field and $\chi^{(2)}(\omega)$.

## 2.3 Results and Discussion

**C-H stretch spectral region**

We applied the time-resolved SFS method to a dispersion of nanoscopic amphiphile-stabilized oil droplets in $D_2O$. The bulk concentration of the amphiphile dodecylsulfate ($DS^-$) was 10 mM. We measured the SFS spectrum (Fig. 2.2a) and the free induction decay (Fig. 2.2b) of the $DS^-$ ions adsorbed at the interface of the droplets. Figure 2.2 shows the methyl and methylene vibrational SFS response of $DS^-$. The signal originates from the $DS^-$ ions alone, since the deuterated methyl and methylene groups of the oil phase vibrate at lower frequencies[105]. Figure 2.2a

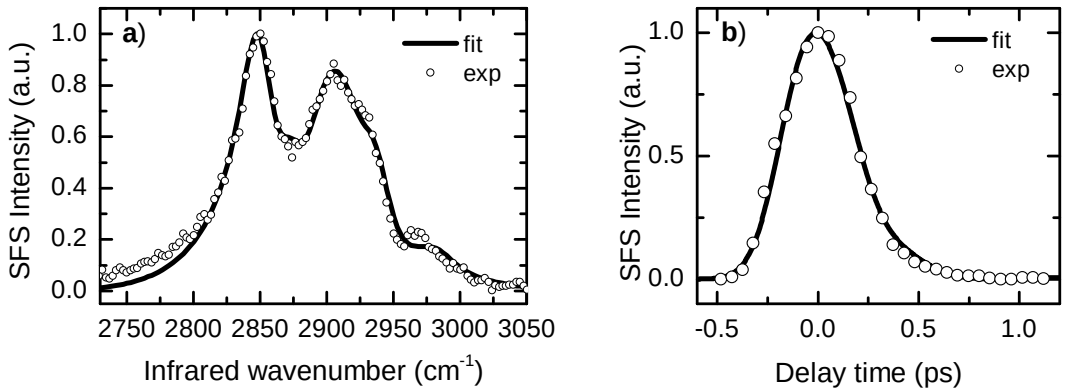


Figure 2.2: (a) Frequency-domain and (b) Time-domain (FID) SFS signal of the methyl and methylene vibrational modes of $DS^-$ ions at the aqueous interface of nanoscopic hexadecane droplets. Circles represent experimental data points and solid lines are simultaneous fits to the data using the model described in section 2.2.2

depicts the SFS intensity spectrum in ppp polarization combination (i.e. all beams are polarized parallel to the scattering plane). The spectrum shows the symmetric methylene ($d^+, \sim$2852 $cm^{-1}$) and methyl ($r^+, \sim$2871 $cm^{-1}$) stretch modes, the antisymmetric methylene ($d^-, \sim$2919 $cm^{-1}$) and methyl ($r^-, \sim$2974 $cm^{-1}$) stretch modes. The symmetric stretch modes are split by Fermi resonance with deformation modes thereby giving rise to two resonances each; the overtone modes that gain intensity are labeled as 'Fermi resonance', as is convention in the SFG community[106]. The modes gaining intensity by Fermi resonance are the $d^+_{FR}$ ($\sim$2890-2920 $cm^{-1}$) and $r^+_{FR}$ ($\sim$2934 $cm^{-1}$) modes, as similarly reported in[69,106–108]. The region between 2890 and 2930 $cm^{-1}$ is notoriously difficult to interpret; it contains Fermi resonances that are very sensitive to conformational and environmental influences and many modes overlap each other[109].

Figure 2.2b displays the time-resolved SFS signal of the same sample dispersion as in Figure 2.2a. Here, the ppp intensity has been integrated and recorded as a function of the infrared-visible delay time. The curve represents a first demonstration of a time-domain SF scattering measurement; it shows the free induction decay (dephasing) of the C-H vibrational modes of interfacial $DS^-$ ions. We observed a fast dephasing with characteristic decay time of ∼0.5 ps, which can be explained by the great number of modes that are simultaneously excited by the broad band IR pulse. While the vibrational dephasing time of a single C-H stretch mode is of the order of 1-2 ps, the interference of the modes can result in a faster overall decay of the polarization.

Using the model described in Section 2.2.2, we were able to simultaneously fit both time and frequency-resolved data assuming the above mentioned resonances and an additional non-resonant response. The results are summarized in Table 2.1. The deviation on the red frequency side probably results from the simplification of using a non-resonant response that is completely frequency-independent. In previous studies we have determined that the non-resonant response is enhanced on the red frequency side of the CH-stretch modes[31]. Including such a modification would, however, not influence the main results described below.

The $d^-$ and $r^+_{FR}$ modes were determined as being out of phase with the other modes. This demonstrates a big advantage of the combined measurement in the time and frequency domain. While the frequency domain measurement could be fitted well with all resonances being in phase, this resulted in a poor fit to the time domain data. The time-resolved response has thus proven to be quite sensitive to the relative phases of the resonances, adding valuable information to the spectral measurement. While one would in general expect two modes split by Fermi resonance to belong to the same symmetry group and thus vibrate in phase, the complexity of the region between 2890-2930 $cm^{-1}$makes it hard to distinguish all the modes in detail. From the measurements it is clear that some of the modes in the Fermi resonance band region have to vibrate out of phase with the symmetric stretch modes to produce the measured TD response.

### Spectral fingerprint region

In addition to the measurements in the C-H stretch region, the sample dispersion can be probed in the spectral fingerprint region around 1000 $cm^{-1}$, in which the symmetric stretch mode of the sulfate head group (-$SO_3^-$) is sum-frequency-active[110]. Figure 2.3a shows the corresponding SFS spectrum. The SFS intensity was normalized by the spectrum of the broadband infrared pulse. It displays a

| mode | $\omega(\,\mathrm{cm}^{-1})$ | $\Upsilon(\,\mathrm{cm}^{-1})$ | $A/A_{d^+}$ |
|---|---|---|---|
| $d^+$ | $2852 \pm 2$ | $10 \pm 1$ | 1 |
| $r^+$ | $2871 \pm 3$ | $8 \pm 13$ | $0.33 \pm 0.10$ |
| $d^-$ | $2919 \pm 4$ | $11 \pm 17$ | $-0.57 \pm 0.18$ |
| $r^-$ | $2974 \pm 12$ | $10 \pm 5$ | $1.34 \pm 0.15$ |
| $d^+_{FR}$ | $2898 \pm 2$ | $24 \pm 1$ | $3.68 \pm 0.16$ |
| $r^+_{FR}$ | $2934 \pm 4$ | $9 \pm 2$ | $-0.78 \pm 0.07$ |
| $A_{NR}/A_{d^+}$ | $0.3 \pm 0.02$ | | |
| $\phi_{NR}$(deg) | $247 \pm 3$ | | |

Table 2.1: Parameters obtained from the fitting to the time- and frequency-resolved data in the CH-stretch spectral region. Amplitudes are given relative to the amplitude of the $d^+$ mode. Confidence intervals are given as $\pm$ one standard deviation.

strong resonance at $1062\,\mathrm{cm}^{-1}$ which we assign to the symmetric stretch mode of the head group. Additionally, a shoulder at lower frequencies $\sim$$995\,\mathrm{cm}^{-1}$ is visible. To further investigate this feature, we tuned the infrared pulse further to the red side of the spectrum. The resulting spectrum and the corresponding FID are shown in Fig. 2.3b,c. The spectral signature exhibits both the resonance of the sulfate

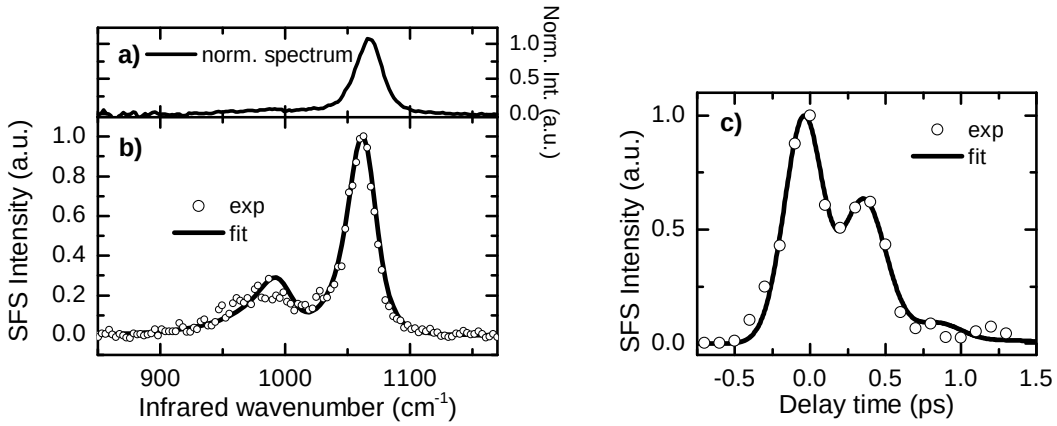


Figure 2.3: **A closer look at the beating feature:** (a) Frequency-domain and (b) Time-domain (FID) SFS signal of of $DS^-$ ions in the spectral fingerprint region. The exciting IR pulse was centered at $\sim$$1000\,\mathrm{cm}^{-1}$ to enhance the influence of the mode at $990\,\mathrm{cm}^{-1}$. Circles represent experimental data points and solid lines are simultaneous fits to the data using the model described in Section 2.2.2

head group and a second vibrational mode at $998\,\mathrm{cm}^{-1}$. This second mode is even more apparent in the time-resolved measurement; its interference with the sulfate

stretch mode results in a coherent beating of the FID signal with a beating period of $\sim 450\,\mathrm{fs}$. The corresponding difference frequency of $65\,\mathrm{cm}^{-1}$ fits well with the measured spectrum. The additional mode we observed has not been reported yet in SFG studies; nonetheless, the detected beating signal corroborates the evidence already seen in the frequency-resolved data. We suggest that the broader signal at $998\,\mathrm{cm}^{-1}$ originates from the C-O-S stretch band. Evidence for such a band in this frequency range has previously been reported in IR and Raman studies [111,112].

As for the CH-stretch spectral region, we fitted TD and FD data simultaneously. The results are summarized in Table 2.2. Due to the dispersion of both the calcium fluoride window and $D_2O$, we used a fit parameter for the linear chirp $a$ thereby including the possibility of some linear chirp of the exciting IR pulse. However, as already pointed out in the methods section, the influence of the two dispersive media mostly cancels; the fit is not very sensitive to the chirp and hence the data was fitted with $a$ set to zero. The residual deviations to the measured data might arise because of higher order dispersive contributions, which can not be completely accounted for by a linear chirp parameter. This dispersive influence could be included for a refined modeling procedure, which might improve the fit to the data especially on the red frequency side of the spectrum.

| mode | $\omega(\mathrm{cm}^{-1})$ | $\Upsilon(\mathrm{cm}^{-1})$ | $\mathrm{A}/\mathrm{A}_{\mathrm{SO_3\ ss}}$ |
|---|---|---|---|
| $SO_3$ ss | $1065 \pm 3$ | $8.7 \pm 1.3$ | 1 |
| COS | $998.0 \pm 5$ | $14.3 \pm 11.4$ | $0.38 \pm 0.12$ |
| $\mathrm{A}_{\mathrm{NR}}/\mathrm{A}_{\mathrm{SO_3\ ss}}$ | $0.09 \pm 0.03$ | | |
| $\phi_{\mathrm{NR}}(\mathrm{deg})$ | $214 \pm 30$ | | |

Table 2.2: Parameters obtained from the fitting to the time- and frequency-resolved data in the SO-stretch (spectral fingerprint) region. Confidence intervals are given as $\pm$ one standard deviation.

## 2.4 Conclusion

In summary, we demonstrate the first realization of time-domain sum frequency scattering experiment. We measured the free induction decay of vibrational modes of amphiphilic molecules that were adsorbed onto the interface of nanoscopic hexadecane droplets in aqueous solution. Both the alkyl C-H stretch response and the response in the spectral fingerprint region were measured. Coherent beating effects between vibrational modes could be observed, thus strongly suggesting a sum-frequency-active C-O-S vibrational mode around $995\,\mathrm{cm}^{-1}$. Using a simultaneous

fitting to both time- and frequency-resolved data, we found that in the region between 2890 and 2930 $\mathrm{cm}^{-1}$ some vibrational modes, likely the Fermi resonance band, vibrate out of phase with the symmetric methyl and methylene stretch modes. This time-domain SF study in a scattering geometry opens up possibilities to study dynamics of molecules at liquid-liquid interfaces, nanoscopic particle interfaces as well as biological interfaces in aqueous solutions. It thus represents a key step towards the study of vibrational dynamics, such as the rotational dynamics of water that are essential for a complete understanding of interfacial hydration processes.

# 3 Specific ion effects and electric double layer formation induced by hydrophobic interactions

*Hydrophobic effects play a key role in many physiochemical and biological systems where (charged) mixed hydrophilic/hydrophobic interfaces are ubiquitous. Using interface-specific and chemically specific techniques, we address how changing the counterion hydrophobicity affects the structure of an amphiphile-stabilized charged hydrophobic interface and the adjacent electric double layer. Using sum frequency and second harmonic scattering, as well as electrophoretic mobility measurements, we can separately follow the change in the water structure, in the effective charge of the interface, and in the structure of both counterions and amphiphiles. Only large tetraalkylammonium counterions with sizes $\gtrsim 1\,nm$ readily adsorb onto the interface, forming a Stern layer with the negatively charged amphiphilic dodecylsulfate ions. We found that this adsorbed double layer appears to be a mixed monolayer in which the positive counterions seem to reside as close to the hydrophobic interface as the adsorbed amphiphiles.*

## 3.1 Introduction

Roughly sixty percent of the human body consists of water, which is continuously in contact with biochemical constituents and dissolved ions. The sub-nm thick interfacial contact region of water with macromolecules or biomembranes typically comprises hydrophobic and (charged) hydrophilic parts. Specific ion effects[3,113,114] and hydrophobic effects[34,115], which are closely linked[12,44], greatly influence the structure and properties of the interface and the adjacent electric double layer[87]; both affect phenomena such as membrane formation, self-assembly, protein folding and stability[8,13,116–118].

Recent theoretical[7,119–121] and experimental studies[22,24,48,122–132] have provided valuable insights about ion-specific effects but have also shown that understanding of specific ion effects is challenging because of the complex solvation structure near an interface[11]. The solvation of hydrophobic solutes is governed by the strong water-water interaction and displays an important crossover from molecular to microscopic hydrophobicity on the nanometer length scale ($\sim$1 nm); water strengthens its H-bonding network around small hydrophobic solutes, but moves away from larger solutes forming a liquid-vapor-like interface[14,34,133]. This important crossover has been experimentally seen for solutes in bulk liquid water with X-ray and Raman spectroscopy[133,134].

Here, we want to add to the existing studies by investigating interfacial processes in which the hydrophobic interaction of solutes at a negatively charged aqueous hydrophobic interface induces a change in the surface structure. By following the structural changes of anions, cations, and water molecules as a function of changing hydrophobicity, we provide a complete molecular level picture of these induced changes. The amphiphilic anions, which negatively charge the surface, the cations whose hydrophobicity was varied, and water were probed with interface-specific techniques. Addionally, the zeta potential of the interface was measured, which indirectly allows us to determine the interfacial charge density. To study the effect of increasing hydrophobicity, we tuned the size of tetraalkylammonium cations ($TAA^+$) in the aqueous solution by increasing their alkyl chain length from a methyl group ($TMA^+$) to an ethyl ($TEA^+$), propyl ($TPA^+$), and butyl ($TBA^+$) group. The size of the cation, which is strongly connected to the hydrophobic interaction[34], thereby changes from a diameter of about 0.7 nm to 1 nm[135,136].

Our findings show that the most hydrophobic counterions ($TBA^+$ and $TPA^+$) readily adsorb to the interface and form a Stern layer. Our data further suggests that the structure of this layer is most likely a mixed monolayer structure

with anions and cations occupying independent surface sites. The less hydrophobic counterions ($TEA^+$ and $TMA^+$) showed only a weak or even no surface activity. First, we briefly motivate and introduce the methods and then describe our results, from which we determine the molecular structure and charge of the interface.

As a model system, we used a solution of negatively charged (amphiphile-stabilized) nanoscopic liquid hexadecane droplets in an aqueous solution. Such a system mimics key aspects of the multitude of charged hydrophobic/water interfaces in a biological environment and it captures the essential size range of objects present in a biochemical environment. The system also contains an extremely large surface to volume ratio in a small sample volume, which ensures an improved signal to noise ratio and reduced sensitivity to impurities compared to measurements on planar interfaces. It further allows for simultaneous charge and surface structure measurements. The charge within the slip plane or, respectively, the electrostatic potential at the slip plane, can be measured with electrokinetic mobility measurements[87]. The surface structure of water can be probed with second harmonic scattering (SHS), that occurs only in non-centrosymmetric regions; it therefore probes anisotropically oriented water molecules, as induced by an interface and/or an electric field[73,131,137,138]. The surface structure of anions and cations at the charged hydrophobic/water interface was measured with vibrational Sum Frequency Scattering (SFS), a vibrational coherent surface spectroscopy that measures the combined IR and Raman spectrum of molecules that can only give rise to signal in non-centrosymmetric environments such as interfaces[27,106]. SFS probes anisotropically oriented chemical moieties at the interface. Because of the azimuthal isotropy of the interface, it is only sensitive to chemical moieties that are oriented along the surface normal[50,139]. Interfacial $DS^-$ anions were probed by measuring their sulfate stretch (S-O) mode ($\sim$1045 $cm^{-1}$) and the interfacial $TAA^+$ cations were probed by measuring their methyl and methylene stretch (C-H) modes. Deuteration of both the oil phase and $DS^-$ ions was used to selectively probe the cations, since C-D and C-H modes vibrate at different frequencies. The combination of electrokinetic measurements, SHS, and SFS allows us to retrieve a complete molecular level picture of the nanoscopic oil droplet/water interface. We are thus able to follow the changes in the interfacial structure induced by an increasing hydrophobicity of the counterions present in the aqueous solution.

## 3.2 Materials and Methods

d-hexadecane (98% d, Cambridge Isotope), d-SDS (99% d, Cambridge Isotope), TMAC (99%, Fluka), TEAC (98%, Sigma-Aldrich), TPA (98%, Sigma-Aldrich),

TBAC (97%, Sigma-Aldrich) and $D_2O$ (99%, Sigma-Aldrich) were used as received.

Dispersions of oil droplets in water for SFG were prepared with 2 v/v % of hexadecane ($C_{16}$) in solutions of 20 mM of d-SDS and after emulsification diluted with solutions 200 mM solutions of TMA, TEA, TPA, and TBA, respectively, to arrive at the desired droplet volume percentage (1 v/v %) and salt concentration (compare 1.3.1). The size distribution and the zeta potential of the droplets were measured with dynamic light scattering and laser Doppler electrophoresis (Zetasizer Nano ZS, Malvern).

SHS and vibrational SFS were performed as described in 1.3.3 and 1.3.2. All shown SFS spectra were normalized by the IR spectrum which was measured by SFG in reflection geometry from a z-cut quartz crystal (C-H region) or from a gold substrate (S-O region).

## 3.3 Results

Fig. 3.1 shows the zeta potential and the SHS intensity of a dispersion of hexadecane nanodroplets (∼100 nm radius) that were stabilized with 10 mM sodium dodecylsulfate (SDS). The particles were dispersed in aqueous solutions of pure $D_2O$, or $D_2O$ with 100 mM of NaCl, TMACl, TEACl, TPACl, and TBACl, respectively. NaCl is surface neutral; the ions are neither accumulating at the surface, nor are they repelled from it[140]. We therefore used NaCl as a reference electrolyte. The

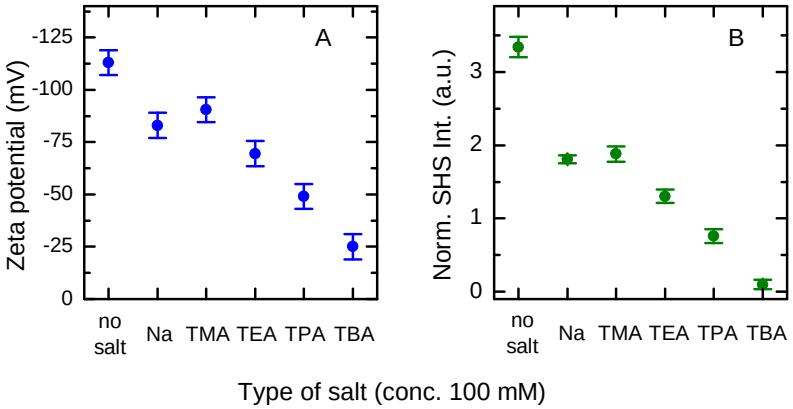


Figure 3.1: (a) Zeta potential and (b) SHS signal of $SDS^-$stabilized oil nanodroplets in solutions without salt, and with 100 mM of NaCl, TMACl, TEACl, TPACl and TBACl, respectively.

magnitude of the zeta potential decreases from the salt free solution to NaCl and TMACl by about 25 mV. It further decreases approximately 20 mV per additional

methylene group of the substituent chains, from -69 mV for TEACl to -25 mV for TBACl. Fig. 3.1b displays the corresponding SHS signal (with the exciting and the analyzed light polarized along the scattering plane, i.e. in pp polarization combination). The hyper Rayleigh scattering (HRS) background of the aqueous solution without droplets was subtracted from the measured SHS signal. The obtained value was normalized to the HRS response of pure water as detailed in Ref. 72. The change in the SHS intensity is similar to the change in the magnitude of the zeta potential; it decreases when salt is added to the solution and further decreases with increasing size of the cations, i.e. increasing number of methylene groups in the substituent chains.

Fig. 3.2 shows SFS spectra of a dispersion of hexadecane ($C_{16}$) oil nanodroplets prepared with deuterated (d)-$C_{16}$, and 10 mM of deuterated SDS in aqueous solutions of pure $D_2O$, and $D_2O$ with 100 mM of TMACl, TEACl, TPACl, and TBACl, respectively. Fig. 3.2a displays the SF spectra of the C-H modes. The response originates from $TAA^+$ ions alone, since the alkyl chains of $C_{16}$ and $DS^-$ were deuterated and therefore vibrate at lower frequencies[105]. The grey line represents a $DS^-$ alkyl chain spectrum of a dispersion of deuterated $C_{16}$ droplets in a solution of 10 mM of non-deuterated SDS. Fig. 3.2b displays the SF spectra of the S-O symmetric stretch vibration of deuterated $DS^-$ of the same samples as in (a). In Fig. 3.2c, we show the integrated amplitudes of the S-O response of the $DS^-$ anions and of the C-H response of the $TAA^+$ cations. The signal of the sulfate head group vibration of $DS^-$ ions on the interface is not changing with different dissolved cations, while the signal of the C-H vibration of $TAA^+$ ions increased for longer alkyl chains. Droplets solutions with $TMA^+$ ions did not display any surface signal. For $TEA^+$ ions, only weak features of probably the Fermi resonance ($2941\,cm^{-1}$) are visible. However, clear spectral signatures of the symmetric ($2874\,cm^{-1}$) and antisymmetric methyl stretch modes as well as the Fermi resonance appear in droplet solutions with $TPA^+$ and $TBA^+$ cations.

## 3.4 Discussion

### Transition of $TAA^+$ ions from bulk active to surface active

The absolute zeta potential values (Fig. 3.1a) decrease gradually with the size of the cation. For $Na^+$ and $TMA^+$ cations, the zeta potential is approximately equal, 20 mV lower than that for the salt-free solution. For these ionic solutions, the SHS signal decreases as well, but no cations are observed on the interface with SFS (Fig. 3.2a,c). The decrease of the zeta potential upon adding ions to the solution

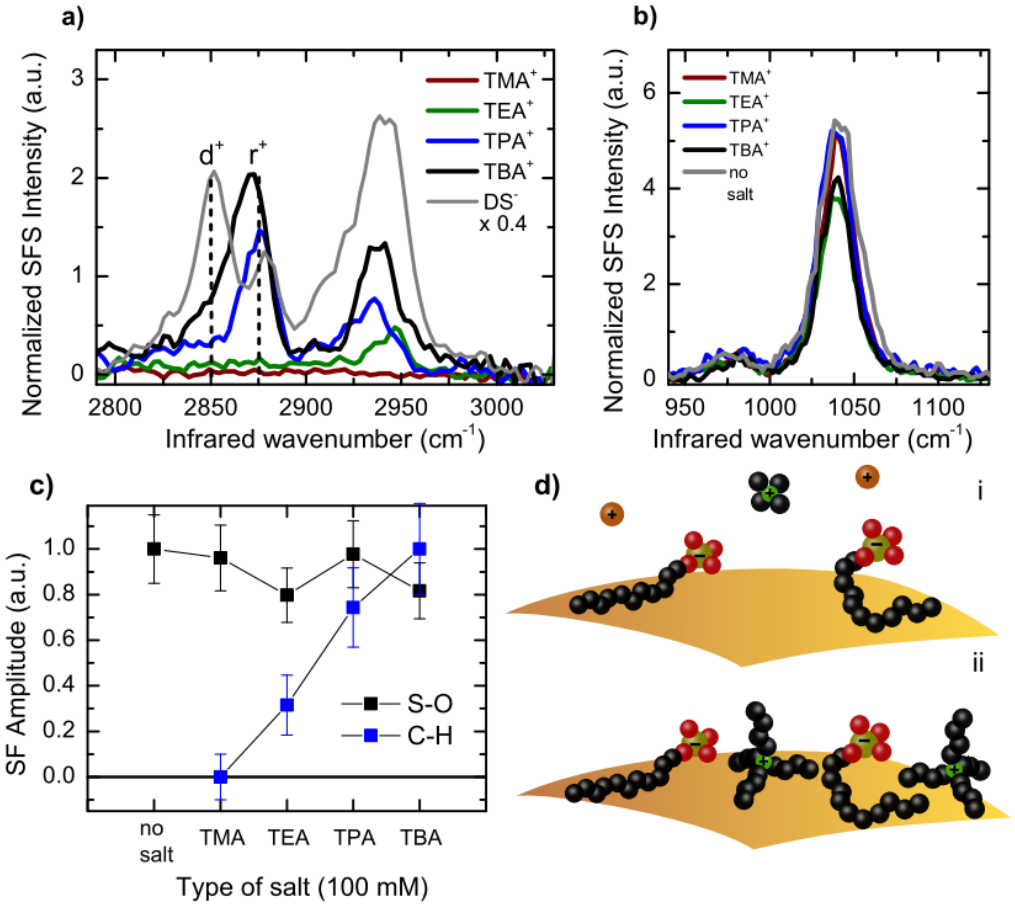


Figure 3.2: SFS spectra of hexadecane nanodroplets stabilized with 10 mM d-SDS in pure $D_2O$, and in aqueous ($D_2O$) solutions of 100 mM of TMACl, TEACl, TPACl, and TBACl, respectively. The spectra are recorded in ssp polarization combination (i.e. the SF and VIS beams are polarized perpendicular to the scattering plane, while the IR beam is polarized in the scattering plane). (a) SFS spectra displaying the C-H stretch vibrational signature of the $TAA^+$ ions at the hexadecane-$D_2O$ interface; for comparison, the (scaled) spectrum of h-$DS^-$ ions on the droplet interface of a sample with 10 mM h-SDS in pure $D_2O$ is also shown. (b) SFS spectra displaying the symmetric sulfate stretch mode of the d-$DS^-$ ions for samples with different TAA-counterions, and for comparison, no additional electrolyte. (c) Integrated amplitudes of the C-H and S-O SF signals indicating the relative amount of $TAA^+$ cations and $DS^-$ anions on the surface. The amplitude was normalized to the maximum signal of the respective series. (d) A possible illustration of the surface structure that agrees with the data. From top to bottom: surface with $DS^-$ and (i) $Na^+$/ $TMA^+$ ions, which both were shown to be bulk active, and (ii) $TBA^+$ ions, which readily adsorbed to the interface and likely form a mixed monolayer with the $DS^-$ ions.

can be explained by the compression of the double layer. With increasing size of the ions, the electrostatic potential inside the slip plane is increasingly reduced, because larger, more polarizable ions move closer to a hydrophobic surface[7,141–143]. For the solutions containing $TEA^+$, and to a much larger degree for those containing $TPA^+$ and $TBA^+$, the SFS signal shows that the cations adsorb onto the negatively charged oil-water interface. The fact that we observed a SFS signal clearly indicates that an adsorbed double (Stern) layer is formed with $TBA^+$ and $TPA^+$ ions, while $TMA^+$ and $Na^+$ ions reside in the diffuse double layer. The transition from bulk active to interface active ions happens at $\gtrsim$0.9-1 nm, the typical length scale on which previous theoretical and experimental work reported the hydrophobic crossover[14,34,46,133,144]. For example, Raman hydration shell spectra showed that there is cooperative behavior involved in the formation of dangling O-H bonds[47]. This cooperative behavior starts for $TAA^+$ solutes with an alkyl chain length of three carbon atoms, i.e. for $TPA^+$ ions.

### Molecular conformation of $TAA^+$ ions

From the SFS spectra shown in Fig. 3.2a,b, we can also infer information about the molecular conformation of the ions from the relative intensities of the methylene (-$CH_2$) and methyl (-$CH_3$) vibrations. The ratio of amplitudes of the symmetric -$CH_2$ ($d^+$) and -$CH_3$ ($r^+$) stretch modes is an indicator for conformational order[31,145–147]. The SF spectra of the $TPA^+$ and $TBA^+$ ions are dominated by the $r^+$ mode, while the $d^+$ is nearly absent. For $TPA^+$ ions with an even number of -$CH_2$ groups, the small contribution of the $d^+$ mode might be explained by an all-trans configuration of each of the four alkyl chains. In such a configuration the radiation from the two -$CH_2$ groups in each side chain cancels as a consequence of local inversion symmetry. However, this configuration would not explain the nearly absent $d^+$ mode in the case of $TBA^+$ ions, which have an odd number of -$CH_2$ groups in each side chain. A configuration that explains the spectra of both $TPA^+$ and $TBA^+$ ions consists of one side chain pointing into the water phase and the three residual side chains rather aligned along the interface (as illustrated in Fig. 3.2c). In this scenario, the methyl group that is pointing towards the water phase would mainly contribute to the spectral signature. Although not definitive, this interpretation is in agreement with angle-resolved photoelectron spectroscopy measurements and molecular dynamics simulation studies of the air-water and air-formamide interface[119,143,148]. The $TEA^+$ ion may adopt a different conformation, but the low signal to noise ratio makes the spectrum difficult to interpret.

### Surface charge density

In this paragraph, we aim to estimate the additional surface charge density induced by the adsorption of $TAA^+$ ions. To do so, we compare the amplitude of the $r^+$ mode of $TAA^+$ to that of $DS^-$ amphiphiles from a reference sample. The surface density and conformation of $DS^-$ has previously been determined by experiment and simulation[30,149]. The alky chains of $DS^-$ show gauche defects and are predominantly oriented parallel to the interface. $DS^-$ amphiphiles occupy on average an area of 4.25 $nm^2$ per molecule, corresponding to a charge density of -3.7 $\mu C/cm^2$. By comparing the relative strength of the $r^+$ mode of $TAA^+$ to that of $DS^-$ ions, we can therefore estimate the interfacial charge density of the $TAA^+$ cations from the charge density of $DS^-$ ions. This calculation should be treated with caution, as there are several flaws when directly comparing the spectra; namely (a) the droplets of the sample used for the $DS^-$ reference spectra were not made in the same batch as the droplets for the $TAA^+$ samples, so that the droplet size distribution might be slightly different; (b) the conformation and orientation of the $CH_3$ groups of $TAA^+$ and $DS^-$ are different. Based on the concluded alkyl conformation of the cations, mainly one methyl group per cation contributes to the signal. Most likely, this methyl group is oriented more normal to the interface than the 'flat' methyl group of the $DS^-$ anion (see above). This suggests that the TAA signal per molecule is greater than that of $DS^-$. The interfacial charge density of cations, as estimated from the amplitude ratio or the $r^+$ modes, therefore represents an estimate of the maximum cation surface density. This maximum surface charge density is estimated to 3.1 $\mu C/cm^2$ for $TBA^+$ and 2.6 $\mu C/cm^2$ for $TPA^+$. The numbers agree well with the reduction in the magnitude of the zeta potential (Fig. 3.1a).

### Stern layer structure

The electric double layer can contain both adsorbed ions (Stern layer) and diffusely bound ions[87]. A Stern layer is formed when the counterions are immediately adjacent or paired to surface charges. The SFS data shows that the surface charge density of anions is constant while the surface charge density of cations increases with increasing alkyl chain length of the cations' side chains (Fig. 3.2c). Surface active $TAA^+$ cations therefore do not compete with $DS^-$ for empty surface sites but rather form a mixed adsorbed double or monolayer. A few possible scenarios could be imagined: First, the counterions could be paired (i.e. in immediate proximity) to the $DS^-$ anions, or separated by water. Second, the ions could form a capacitor-like double layer or a mixed monolayer. Large, surface-active $TAA^+$ ions are hydrophobic 'soft' solutes and thus interact strongly with the hydrophobic

phase rather than with the 'hard' ionic group of $DS^-$ (see Section 1.1). One would therefore expect that the alkyl chains of the surface active $TAA^+$ ions seek contact with or even immerge into the oil phase. Since the head groups of $DS^-$ ions are well hydrated and reside rather deep in the water phase (compare Ch. 4 and Ref. 149), the TAA cations should be closer to the surface than the $DS^-$ head groups. Furthermore, a water-filled capacitor-like double layer with the $DS^-$ head group closer to the surface than $TAA^+$ is unlikely because it would result in an enhanced SHS signal which we did not observe. In summary, the above discussion suggests that cations and anions form a mixed monolayer at the oil-water interface of the droplets. The concept of matching water affinities (Section 1.1) suggests that the soft cation is not paired with the hard anionic head group of $DS^-$ in this mixed monolayer.

## 3.5 Conclusion

In summary, we have shown how the increased size and thus increased hydrophobicity of tetraalkylammonium ($TAA^+$) cations induces the formation of a Stern layer at the oil-water interface of a nanoscopic droplet dispersion. Using a combination of surface-specific techniques, we were able to clearly separate the induced changes in the structure of interfacial water, of interfacial dodecyl sulfate ($DS^-$) and $TAA^+$ ions, and the induced change in the interfacial charge density. We conclude that the formed Stern layer is most likely a mixed monolayer of $DS^-/TAA^+$ pairs and that it is only formed if the size of the $TAA^+$ cation is $\gtrsim$1 nm, i.e. for $TBA^+$ and $TPA^+$. Thus, the structure of ions and water molecules resembles more that of a zwitterionic monolayer[125] than that of a capacitor-like double layer. Our results show that the structure of the diffuse and adsorbed double layer changes strikingly when hydrophobic interactions are tuned. They also support that the hydrophobic domain size of $\sim$1 nm marks a crossover that is important for the interfacial organization of ions and water molecules. Moreover, the obtained knowledge about the hydrophobic behavior of $TAA^+$ ions might trigger further molecular-scale studies of these ions that are of wide interest for biology and chemistry because they are both important phase-transfer catalysts and ion-channel blockers[150–152].

# 4 Specific ion effects in amphiphile hydration and interface stabilization

*Ionic amphiphiles are known to stabilize the oil-water interface of nanoscopic droplets, presumably by dipping their hydrophobic tails into the oil phase while sticking their hydrophilic head groups into the water. With vibrational sum frequency scattering, we investigated the structure of the amphiphile-stabilized interface of two amphiphiles that contain the same alkyl tail but different head groups. We found that the amphiphiles adopt strikingly different structures at liquid hydrophobic water interfaces, linked to the specific interactions between water and the different amphiphile head groups, as shown by solute-correlated Raman spectroscopy. We showed that Dodecylsulfate ($DS^-$) ions induce no detectable change in the conformation of interfacial oil molecules while dodecyltrimethylammonium ($DTA^+$) clearly increase their disorder. Furthermore, the $DTA^+$ and $DS^-$ ions' alkyl chains showed distinct conformations on the oil-water interface, but similar structures at the interface of impenetrable PTFE particles. We correlate the differences we found with a Hofmeister-like ordering of the head groups. Our work suggests that specific head group interactions with water play a key role in driving the anionic $DS^-$ head group towards the water phase and the cationic $DTA^+$ head group towards the oil phase, thus also implying differing surface stabilization mechanisms.*

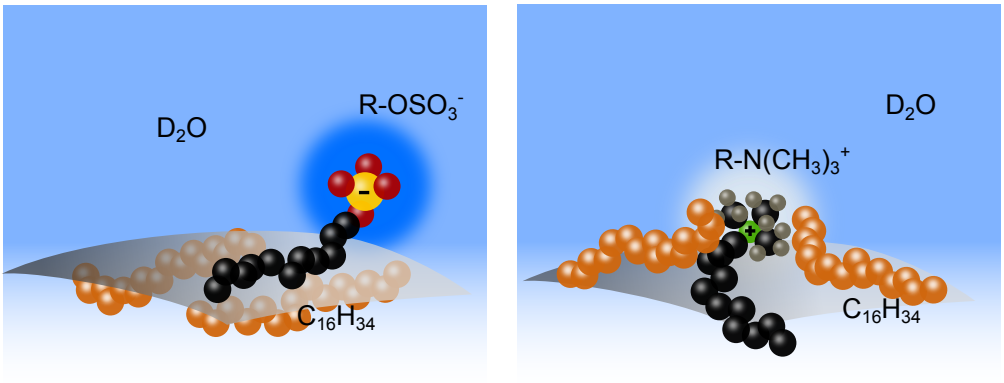


Figure 4.1: $DS^-$ and $DTA^+$ amphiphiles show distinct hydration behavior which results in strikingly different interfacial structures of the oil-water interface. This picture represents a tentative schematic of the conformational arrangement as determined by our experiments.

## 4.1 Introduction

Specific ion effects* occur in many biological and chemical phenomena, such as protein folding, enzyme activity, bacterial growth, transport across membranes, and colloidal assembly[3,37,113,114,153]. Similarly, specific effects attributed to ionic head groups were proposed, establishing a Hofmeister-like series for head groups of amphiphiles and lipids[154,155]. Here, we compare how different amphiphiles interact with liquid hydrophobic water interfaces. More specifically, we focus on single chain amphiphiles of similar structure, but either with negatively ($-OSO_3^-$) or positively charged ($-N(CH_3)_3^+$) head groups. We used surface sum frequency scattering (SFS) to probe changes in both the amphiphile and liquid oil structure induced by adsorption of the amphiphiles onto oil nanodroplets in water. Because biomolecules such as proteins have hydrophobic patches that are of nanoscopic size, oil nanodroplets in water can be used as a model system that is more realistic than planar hydrophobic water interfaces, such as the air-water interface. Nanoscopic droplet dispersions also enable the in-situ preparation of a large amount of clean oil-water interface. Although one might have expected that the two surfactants would adopt a quite similar structure at the interface, and that they would both have a similar influence on the structure of the interfacial oil molecules in the nanodroplet, our results tell a quite different story. We found that the head groups mentioned above, not only interact with water molecules very differently (as confirmed by Raman hydration shell spectroscopic measurements), but also have a remarkably

*for an introduction to specific ion effects, refer to section 1.1

different influence on both the surfactant's hydrophobic alkyl chain and the oil molecules in the nanodroplet. More specifically, the surfactants with the -$OSO_3^-$ head group did not affect the conformation of the oil molecules, while those with the -$N(CH_3)_3^+$ head group induced a clear change in the interfacial oil structure. Therefore the specific nature of the interaction of the ionic head groups with both water and oil has a major impact on the structure of such biologically relevant interfaces.

The chapter is organized as follows. We first describe the differences in the hydration shell of octylsulfate ($OS^-$) and octyltrimethylammonium ($OTA^+$) ions obtained with Raman solvation shell spectroscopy. Then we describe the vibrational sum frequency scattering measurements that were used to determine the structure of dodecylsulfate ($DS^-$) and dodecyltrimethylammonium ($DTA^+$) ions on impenetrable solid nanoparticles and penetrable liquid oil nanodroplets in water. By deuterating the oil phase, we can selectively measure the conformation of the amphiphile's alkyl chains. This is followed by a study of the change in hydrophobic oil conformation at the nanodroplet-amphiphile-water interface upon adsorption of amphiphiles with deuterated alkyl chains.

## 4.2 Materials and Methods

n-hexadecane (99.8%, Sigma-Aldrich), h-DTAB (99%, Sigma-Aldrich), d-hexadecane (98% d, Cambridge Isotope), d-SDS (99% d, Cambridge Isotope), d-DTAB (99% d, Cambridge Isotope) and $D_2O$ (99%, Sigma-Aldrich) were used as received. Aqueous solutions of sodium bromide (NaBr, 98.52%, J.T. Baker), trimethyloctylammonium bromide (OTA+, 98.0%, Aldrich), and sodium octylsulfate (SOS , 95% Sigma) with a concentration of 0.1 M were prepared using ultra-purified water (Milli-Q UF plus, Millipore, Inc., electrical resistance of 18.2 MΩcm)

Dispersions of oil droplets in water were prepared with 2 v/v% of hexadecane ($C_{16}$) in $D_2O$ and after emulsification diluted with solutions of DTAB or SDS in $D_2O$, to arrive at the desired droplet volume percentage (1 v/v%) and amphiphile concentration (compare 1.3.1). The size distribution and the zeta potential of the droplets were measured with dynamic light scattering and laser Doppler electrophoresis (Zetasizer Nano ZS, Malvern).

Frequency-resolved vibrational SFS was performed as described in 1.3.2. All shown SFS spectra were normalized by the IR spectrum which was measured by SFG in reflection geometry from a z-cut quartz crystal.

## 4.3 Results and Discussion

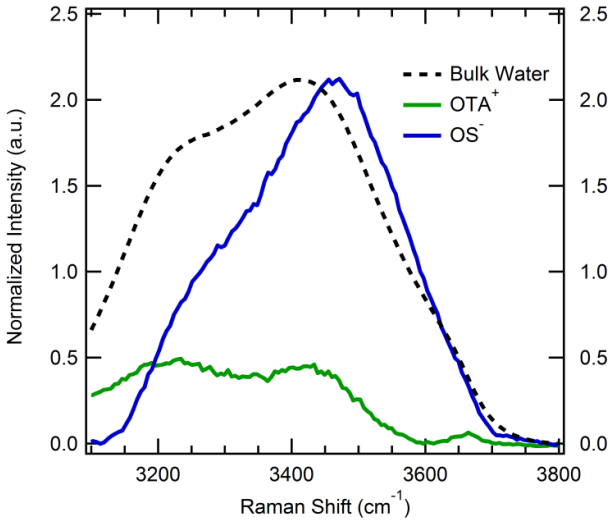


Figure 4.2: **Surfactant ion hydration.** Hydration shell spectra of octylsulfate ions ($OS^-$) and octyltrimethylammonium ($OTA^+$) ions obtained using Raman-MCR. The solute-correlated spectra are normalized to the respective CH stretches of the surfactant ions, displaying the OH-stretch vibrational response of water surrounding the surfactant ions. The black dashed line depicts the OH Raman band of bulk water (scaled to the same height as the $OS^-$ hydration shell OH band).

### Hydration shell structure

Interactions between water and solute molecules can be probed with Raman multivariate curve resolution (Raman-MCR)[79] by detecting solute-induced changes in the OH stretch band of water. For example, Raman-MCR has previously been used to detect water structure changes around hydrophobic[133,156,157] and ionic[78] solutes, as well as interactions between hydrophobic and ionic solutes[91]. Here, we report results obtained with Raman-MCR that reveal differences in the hydration shell structures of $OS^-$ and $OTA^+$ dissolved in water (well below the surfactant cmc).

Figure 4.2 shows the hydration shell spectra of the OH-stretch region of 0.1 M solutions of $OS^-$ ions (blue curve) and $OTA^+$ ions (green curve). The amphiphilic ions contain identical alkyl chains but have either a sulfate or a trimethylammonium head group. The spectra display the OH signature of water molecules that are affected by the solutes, i.e. the amphiphiles. The spectra of the two amphiphiles clearly differ significantly from each other, as well as from

the OH band of bulk water (dashed-black curve). The contribution from the $Br^-$ counterion of $OTA^+$ has been removed by including an equal concentration of NaBr in the water reference spectrum, as previously described[91]. Note that $Na^+$ ions have no observable effect on the water OH band[78]; therefore, no correction for the $Na^+$ counterion of $OS^-$ was necessary. Because of the corrections that have been made, the $OTA^+$ and $OS^-$ spectra in Figure 4.2 arise only from the hydration shell of the amphiphile itself, with little or no contribution from the corresponding counterion. The hydration shell OH spectrum of $OTA^+$ consists of two lobes, peaked at $\sim$3250 $cm^{-1}$ and $\sim$3450 $cm^{-1}$. The spectrum has a more prominent lower frequency OH stretch lobe than the bulk water spectrum. This has been previously observed for the hydration shells around non-polar groups, such as the hydrophobic tails of alcohols of various chain lengths[133]; it therefore indicates that there is enhanced tetrahedral ordering of water molecules around the $OTA^+$ ions. The observed spectrum also confirms that water does not form H-bonds directly to the cationic $OTA^+$ head group, as this would result in a peak at higher frequencies. The hydration shell spectrum of $OS^-$ ions looks quite different; it is dominated by a lobe a higher frequencies that can be associated with water OH groups that are H-bonded to the anionic sulfate head group. A similar spectrum is observed for the hydration shell spectrum of sulfate ions. Thus, the $OS^-$ hydration shell spectrum indicates hydrogen bonding between water and the sulfate head group. In other words, the solvation shell spectrum of $OTA^+$ is indicative of weaker hydration, while that of $OS^-$ is indicative of stronger hydration. We now turn to the molecular structure of the amphiphile-stabilized oil-water interface.

### Amphiphile conformation

Surfactants at the planar oil-water interface have been studied with various methods including neutron scattering, X-ray scattering, and Sum Frequency Generation (SFG)[30,108,158–165]. The molecular surface structure of the oil droplet-water interface can be measured with vibrational Sum Frequency Scattering (SFS), a vibrational coherent surface spectroscopy that measures the combined IR and Raman spectrum of molecules in non-centrosymmetric environments such as interfaces[27,90,95,106]. The SF intensity for each vibrational mode scales quadratically with the surface density of that group multiplied by the square of the cosine of the tilt angle with respect to the interface normal[50,139]. Vibrational modes that lie in the surface plane are therefore not observed. Selective deuteration allows us to independently probe both the surfactant and the oil molecules, since C-D and C-H modes vibrate at different frequencies[105]. The C-H stretch spectral region contains valuable information

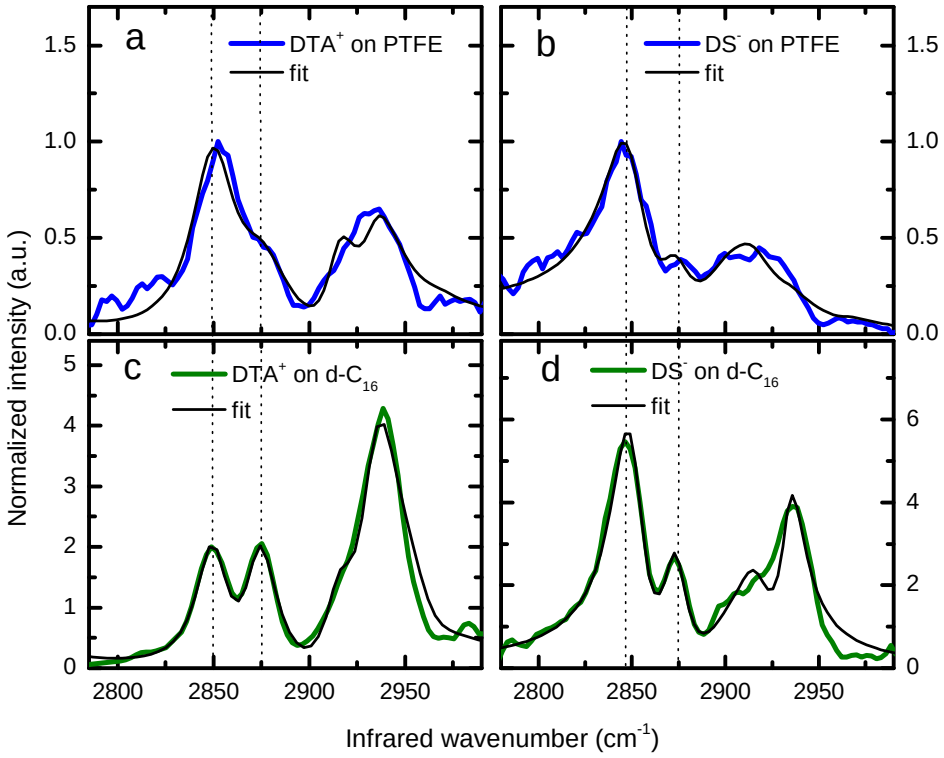


Figure 4.3: **Comparison of the amphiphile structure on the PTFE particle/water interface and the oil droplet/water interface.** (a),(b): SFS-spectra of the interface of PTFE particles with solutions containing $DTA^+$ (15 mM) and $DS^-$ (10 mM) ions. (c),(d) SFS-spectra of the interface of deuterated hexadecane droplets in solutions containing $DTA^+$ (15 mM) and $DS^-$ (10 mM). The frequencies of the symmetric methylene ($d^+$, 2850 $cm^{-1}$ and the symmetric methyl ($r^+$, 2874 $cm^{-1}$) stretch vibration are highlighted by dashed lines. All spectra are taken in the CH stretch frequency region and with the ssp polarization combination. Here, ssp indicates that the sum frequency and visible (infrared) beams are polarized perpendicular (parallel) with respect the scattering plane.

about the alkyl chain conformation and geometry. The amplitude ratio ($d^+/r^+$) of the symmetric methylene ($d^+$, at ~2850 $cm^{-1}$) and the symmetric methyl ($r^+$, at ~2874 $cm^{-1}$) stretch vibrational modes is a common indicator for the conformation of alkyl chains[31,145–147]. A value of $d^+/r^+ \ll 1$ is associated with a stretched alkyl chain, i.e. an all-trans conformation, whereas a value of $d^+/r^+ > 1$ indicates that gauche defects dominate the alkyl chain conformation. When we compare the spectra, we focus on this $d^+/r^+$ ratio, as differences in the spectral region above 2900 $cm^{-1}$ are not immediately useful to determine the chain conformation[105,166].

More specifically, the region above $\sim$2900 $cm^{-1}$ contains a number of modes that are not well resolved, some of which consist of couplings to overtones. The methyl groups in the $DTA^+$ head group vibrate at higher frequencies[105] so they also do not influence our observed $d^+/r^+$ ratios.

To critically test whether or not a given charged amphiphile penetrates into a liquid oil interface we have compared the surface structures of $DS^-$ ions and $DTA^+$ ions adsorbed on liquid oil nanodroplets and on impenetrable polytetrafluoroethylene (PTFE) particles. The following discussion begins with a description of our measurements of the structure of $DS^-$ and $DTA^+$ on PTFE nanoparticles and on deuterated hexadecane oil droplets, followed by a description of our measurements performed using alkyl-deuterated surfactants in order to elucidate amphiphile-induced changes in the interfacial structure of the liquid oil droplets.

Figure 4.3 shows SFS CH-spectra of $DTA^+$ and $DS^-$ ions on PTFE nanoparticles (4.3a,b) and on deuterated hexadecane oil droplets (4.3c,d) dispersed in solutions of SDS and DTAB in $D_2O$. The surfactant concentration in both solutions was slightly above their respective critical micelle concentrations (cmc) achieving maximum surface coverage. Micelles are centrosymmetric and too small to contribute to the signal[30,55]. Figs. 4.3a and 4.3b are very similar, which indicates that the surfactant alkyl chains adopt a similar structure when they adsorb onto the solid PTFE/water interface. Because of this similar conformation, the integrated signal amplitude is proportional to the number density of adsorbed surfactants; this shows that the interfacial coverage of $DS^-$ and $DTA^+$ on PTFE particles is comparable. Is not surprising that the alkyl chain conformation and interfacial coverage of the two amphiphiles on PTFE particles is so similar, because the surfactants both consist of identical alkyl tails and the solid PTFE substrate is impenetrable. Furthermore, the spectra for $DS^-$ ions on PTFE and on hexadecane oil droplets are also very similar (Figs. 4.3b,d), with large $d^+/r^+$ ratios of $\sim$3 indicating the predominance of gauche defects on the spectra shown in Figs. 4.3a,b and d. Our results therefore indicate that alkyl chains of $DTA^+$ ions on PTFE particles, of $DS^-$ ions on PTFE particles, as well as of $DS^-$ ions on hexadecane oil droplets all have approximately the same conformational structure. The spectrum of $DTA^+$ on hexadecane (Fig. 4.3c), however, is clearly different from the others. The $d^+/r^+$ ratio of $\sim$1 indicates an increased order in the alkyl chains. Thus, the surface structures of $DTA^+$ and $DS^-$ ions on the hydrophobic liquid oil droplet surface are considerably different.

The observed differences in the alkyl chain conformation of $DTA^+$ likely stem from enhanced interaction of its alkyl chain with the oil phase. One might

suspect that the effect is merely due to different surface densities of the amphiphiles on hexadecane droplets. Measurements with varying concentration of $DTA^+$ on hexadencane, however, show that the surface densities of the two amphiphiles are comparable and that the distinct conformation is already present at concentrations much below the saturation of the surface. Furthermore, even though counterions can in principally alter specific ion effects[154,167], we found the same distinct conformation of $DTA^+$ on hexadecane when we used $Cl^-$ instead of $Br^-$ as a counterion.

In the next section we consider the effect of the amphiphiles on the surface structure of the oil phase. We will also discuss possible reasons for the observed differences.

### Oil chain conformation

Having characterized the alkyl chains of the $DS^-$ and $DTA^+$ ions on the two substrates, we now describe the structural response of the interfacial oil molecules. Fig. 4.4 shows SFS spectra of the C-H-stretch modes of h-hexadecane droplets dispersed in $D_2O$ with different bulk concentrations of alkyl chain deuterated d-$DS^-$ (a) and d-$DTA^+$ (b). Fig. 4.4a shows the spectra obtained for bulk concentrations of d-$DS^-$ of 0.5, 1.0, 2.0, 5.0 and 7.0 mM (6-86 % of the critical micelle concentration). Within the experimental errors, there is no difference between the spectra: The d-$DS^-$ ions therefore do not detectably influence the oil surface structure. In other words, the liquid hexadecane oil molecules at the interface are not or only very weakly affected by the $DS^-$ ions. Fig. 4.4b depicts the spectrum of h-hexadecane droplets in $D_2O$ with bulk concentrations of d-$DTA^+$ of 0, 3.75, 7.5 and 15 mM (0-98 % of the cmc). The integrated spectral intensity and the $d^+/r^+$ ratio of the vibrational modes of the interfacial oil molecules increase with an increasing surface concentration of d-$DTA^+$ ions. These results clearly show that the surface structure of the interfacial oil molecules is altered by the $DTA^+$ ions, indicating a strong interaction of $DTA^+$ with the oil phase compared to the interaction of $DS^-$ with the oil phase.

In summary, the above results reveal striking differences between the interfacial structure of anionic $DS^-$ and cationic $DTA^+$ amphiphiles. They suggest that $DS^-$ does not or only very weakly penetrate the oil phase. Conversely, $DTA^+$ likely inserts its alkyl chain into the oil phase, a picture that is often given by textbooks independent of the exact nature of the amphiphile[168]. The scheme in Fig. 4.1 summarizes the discussion showing tentative schematic surface structures when the two amphiphiles adsorb to the oil droplet. We suggest the differences to be a result of the distinct interaction of the amphiphiles' head groups with water, as

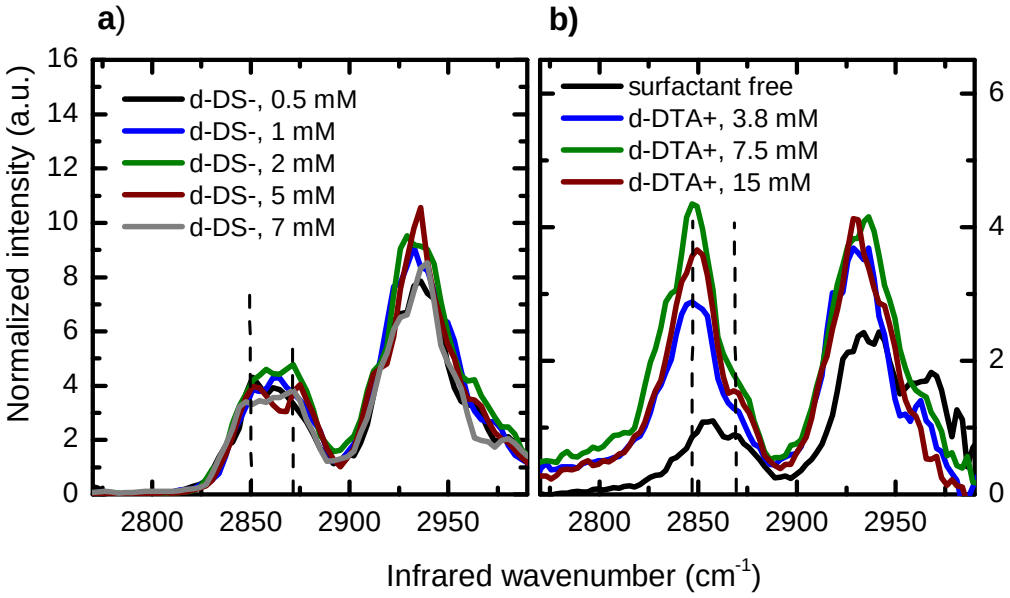


Figure 4.4: The influence of $DS^-$ and $DTA^+$ ions on the interfacial structure of the oil phase. The graphs show SFS spectra of the CH-region of hexadecane nanodroplets in solutions containing various concentrations of $DS^-$ (a) and $DTA^+$ ions (b) with deuterated alkyl chains. All spectra are taken in ssp polarization combination.

shown by the Raman measurements. In the following paragraph we further discuss how the observed behavior of the amphiphiles can be correlated with specific ion effects.

### Specific ion effects

The origin of the remarkably different behavior of $DS^-$ and $DTA^+$ ions lies in the different interaction of the head group ions with water, one being strongly hydrated, and the other being weakly hydrated. The Hofmeister series† describes such specific differences between ionic solutes[8,23,24]. The series ranks ions with respect to their physical properties[3].

$$F^- > \underline{HSO_4^-} > CH_3COO^- > Cl^- > Br^- > NO_3^- > I^- > ClO_4^- > SCN^-$$
$$Ca^{2+} < Mg^{2+} < Li^+ < Na^+ < K^+ < Rb^+ < Cs^+ < NH_4^+ < \underline{N(CH_3)_4^+}$$

In this ranking the ions are ordered according to their ability to salt-out (i.e. stabilize) proteins. In the above ordering, one finds hard weakly polarizable

†See Section 1.1 for a detailed discussion.

and strongly hydrated ions on the left and soft strongly polarizable and weakly hydrated ions on the right. The ionic head groups we studied have structures similar to tetramethylammonium ($N(CH_3)_4^+$), a soft cation, and bisulfate ($HSO_4^-$), a hard anion. In analogy to the given series, attempts have been made to rank ionic amphiphiles in a similar way[154,155]. Our findings strongly support such an ordering of head groups, since we have observed a strikingly different behavior of the monovalent $DTA^+$ and $DS^-$amphiphiles. The observed differences, as well as the differences in surface activity observed within the Hofmeister series could be either attributed to charge or hydrogen bonding. Distinguishing between both effects might be possible; however, because of water's asymmetric structure, the two interactions are intimately linked[169].

### Interfacial stabilization

Macroscopic measurements such as surface tension or enthalpy measurements rely on theoretical models that connect molecular and nanoscale phenomena to their macroscopic manifestations[16,170]. However, mean field theories, such as the Gouy-Chapman-Stern model, ignore the nano- and molecular scale solute and solvent structure; they often only account for water properties with its dielectric constant. It is therefore interesting to speculate about the relationship between the remarkably different interfacial structures of the studied cationic and anionic amphiphiles, the concentration dependence of the interfacial structure, and the resulting different molecular mechanisms by which they might lower the interfacial free energy of the oil-water interface. Our results suggest that anionic $DS^-$ amphiphiles stabilize the oil-water interface by decorating it with strongly hydrated sulfate groups. Thus, water is likely to play a major role and since the oil structure does not appear to change, it is not likely that its free energy changes when $DS^-$ ions are added. Furthermore, cationic $DTA^+$ ions are only weakly hydrated and when they adsorb to the interface, the conformational flexibility of the oil changes. Therefore, both the interfacial water and the oil interact with the amphiphile. The molecular actors have different roles in both surface structures, which suggests that the molecular mechanism by which the interfacial energy is lowered might also be different. This difference could be verified by additional temperature dependent measurements and/or molecular dynamics simulations performed to elucidate entropic, energetic, and molecular contributions to the corresponding amphiphile stabilized surface free energy. Such differences are potentially important to understand biochemical phenomena such as the assembly and stability of vesicles and membranes.

## 4.4 Conclusion

By combining solvation shell Raman spectroscopy and vibrational sum frequency scattering measurements we have discovered the strong influence of specific ion-water interactions on the structure of surfactant stabilized oil-water interfaces. Although, both cationic $DTA^+$ and anionic $DS^-$ amphiphiles stabilized the oil-water interface of nanoscopic droplet dispersion, they have a remarkably different influence on the molecular structure of the interface. $DTA^+$ amphiphiles were shown to only weakly interact with water and to induce a significant change in the structure of the oil phase upon adsorption to the oil-water interface. Conversely, $DS^-$ ions, which interact with water molecules through H-bonds, appear to not affect the conformation of interfacial oil molecules when they populate the interface. The differences we found can be correlated with a Hofmeister-like ordering of ionic headgroups. Furthermore, our results suggest differences between interfacial stabilization mechanisms of the two amphiphiles.

# 5 Charge asymmetry at aqueous hydrophobic interfaces

*The solvation of ions in a dielectric continuum is necessarily symmetric with respect to the sign of the ionic charge. Yet, many phenomena, such as the fact that the vast majority of biological membrane interfaces are neutral or negatively charged, the remarkably low point of zero charge of water, and the hydration energies of negative and positive ions indicate that water has a 'preference' for negative charge. This is evidently linked to the asymmetry of the molecular structure of water. Although there is ample indirect evidence for such charge asymmetry, no previous studies have quantified such effects. Here, we combined linear and non-linear optical spectroscopies to quantify differences between the hydration-shell and hydrophobic/water interfacial molecular structure induced by essentially identical ions that have an opposite charge. We found that tetraphenylborate anions and tetraphenylarsonium cations interact dramatically different: The anions are preferentially hydrated and induce greater orientation order on water near hydrophobic interfaces. In contrast, the cations have far fewer and weaker H-bonds than the anions and strongly reduce the orientational order of water near a hydrophobic interface. Our observations are consistent with the cooperative (for negative ions) or anti-cooperative (for positive ions) interactions of electrostatic forces and H-bonding. Our results further suggest that the enhanced ordering of water around negative solutes and negatively charged surfaces is responsible for the increased stability of negatively charged interfaces.*

## 5.1 Introduction

The vast majority of lipid (cell) membranes, macromolecules and their interfaces are either neutral or negatively charged[49]. The hydrophobic water surface carries a negative charge, and the point of zero charge of most interfaces occurs at very low pH[35,87,171]. The hydration free energies of anions are also significantly more negative than those of cations of similar size[172–174], as are the corresponding hydration entropies[173,175]. Moreover, dynamics of water reorientation and H-bond exchange are quite different around positive and negative ions[43,176]. Both experiments and simulations show that ions of different size, structure, and charge partition differently at aqueous interfaces[3,9]. Although such specific ion (i.e. Hofmeister) effects exist for both negative and positive ions, and although they typically correlate with differences in size, polarizability and/or charge density[40], specific ion effects are often smaller for positive ions than for negative ions[24]. All this suggests an inherent asymmetry in the interaction of water with positive and negative ions or interfaces. The implied charge asymmetry is certainly related to water's highly directional H-bonding proclivity. Although electrostatic interactions are symmetric with respect to charge, H-bonding interactions are not symmetric with respect to solute charge because water preferentially donates H-bonds to anions, $O-H\cdots X^-$. Generally, water's properties stemming from its H-bonding propensity are challenging to understand; e.g., the binding energy of two H-bonded water molecules is affected by other molecules in the vicinity, rendering H-bonding non-additive[177,178]. The asymmetry between the interaction of water with positive and negative ions likely plays an important role in many biochemical and other aqueous chemical processes. However, such asymmetries are difficult to measure and to theoretically model on a molecular level. Here, we show how charge asymmetry results in distinct hydration shell and interface structures of ions with virtually identical chemical and physical properties but opposite charge. We seek to probe the molecular foundation of the difference between the interaction of positive and negative ions with hydrophobic water interfaces. To do so, we investigated tetraphenylarsonium ($Ph_4As^+$) and tetraphenylborate ($Ph_4B^-$,see Fig. 5.1), which are ions of opposite charge but almost identical size, shape and chemical structure. Previous studies of these ions assumed they had identical free energies of transfer across an interface between any arbitrary pair of solvents, thus making the $Ph_4AsPh_4B$ salt ideal as a reference to obtain single ion solvation energies[179,180]. Even though evidence for small differences in the ion-solvent interaction of the two ions were suggested[181,182], their hydration properties were found to be almost identical[183,184]. This suggests,

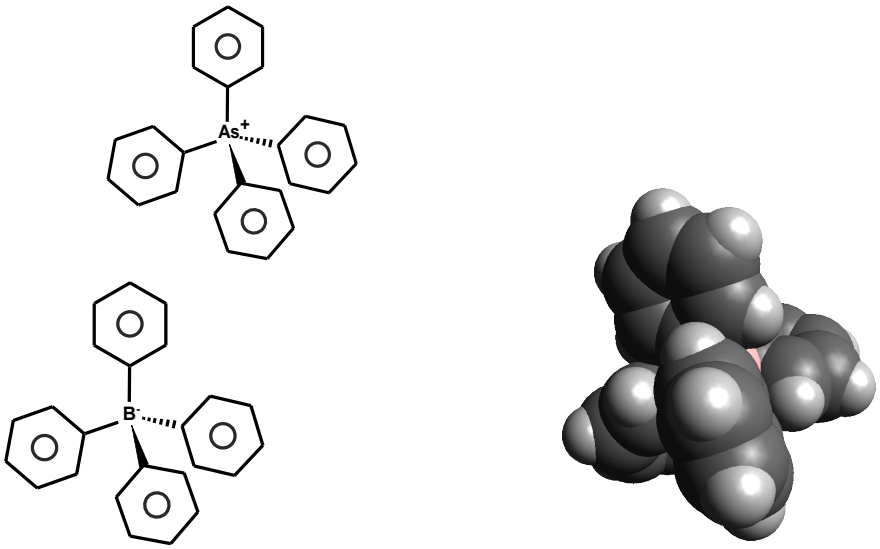


Figure 5.1: Tetraphenylarsonium and tetraphenylborate ions have virtually the same size, shape and chemical structure, but opposite charge. Because of their large dimension and therefore low charge density, the tetraphenylarsonium-tetraphenylborate salt is often used as a reference salt to obtain single-ion solvation energies.

that differences between the two ions are hard to capture and might show up only if methods are applied that are capable of probing the molecular structure of the ions and the surrounding water. We characterized differences in the hydration structure of the tetraphenyl ions; more precisely, we determined differences in the strength and number of H-bonds between water and the delocalized $\pi$-orbitals of the phenyl rings ($\pi$-H-bonding) with Raman hydration shell spectroscopy. Moreover, we probed the effect of the ions on the interfacial properties of a charged hydrophobic water interface with sum frequency and second harmonic scattering (SFS, SHS), and electrokinetic mobility measurements of a nanoscopic dispersion of oil droplets. In this way, we access the charge of the interface, the interfacial water structure, and the ion's interfacial structure of the liquid hydrophobic water interface. With regard to hydration, we found that the $\pi$-H-bond strength to water is stronger for $Ph_4B^-$ than for $Ph_4As^+$, and that the average number of $\pi$-H-bonds is about seven times greater for the anionic $Ph_4B^-$ than for the cationic $Ph_4As^+$. When the bulk concentrations of the two ions are equal, we found that the magnitude of the electrokinetic potential of nanoscopic oil drop interfaces is equal, implying a comparable interface charge density of the droplets with $Ph_4B^-$ and $Ph_4As^+$ on the interface. The influence those oppositely charged ions have on the water

phase is, however, remarkably different. More specifically, our results suggest that the interactions between water and the negative ions work together, while they counteract each other for the positive ions; this results in a more ordered water structure around droplets with negative $Ph_4B^-$ ions on the interface, thus indicating that the negative interface is more stable.

## 5.2 Materials and Methods

Chemicals for scattering experiments: n-hexadecane ($C_{16}$, 99%, Sigma-Aldrich), tetraphenylarsonium chloride (99.5%, Acros Organics), sodium tetraphenylborate (99.5%, Alfa Aesar), and $D_2O$ (99.8%, Sigma-Aldrich) were used as received. Glassware was cleaned with a 3:7 $H_2O_2$:$H_2SO_4$-solution, after which it was thoroughly rinsed with ultrapure water (0.053 $\mu$S/cm,TKA). Aqueous solutions of sodium chloride (Mallinckrodt), tetraphenylarsonium (V) chloride hydrate (97%, Sigma-Aldrich), and sodium tetraphenylborate (99.5%, Sigma-Aldrich) with a concentration of 0.1 M were prepared using ultra-purified water (Milli-Q UF plus, Millipore, Inc., electrical resistance of 18.2 M$\Omega$cm). Phenol (>99%, Sigma-Aldrich) was prepared at a concentration of 0.5 M.

Dispersions of oil droplets in water for SFG (SHG) were prepared with 2 (1) v/v % of hexadecane ($C_{16}$) in $D_2O$ and after emulsification diluted with solutions of $Ph_4As^+$ or $Ph_4B^-$ in $D_2O$, to arrive at the desired droplet volume percentage (1 (0.1) v/v % for SFS (SHS)) and salt concentration (compare also Section 1.3.1). The size distribution and the zeta potential of the droplets were measured with dynamic light scattering and laser Doppler electrophoresis (Zetasizer Nano ZS, Malvern).

SHS and vibrational SFS were performed as described in 1.3.3 and 1.3.2. All shown SFS spectra were normalized by the IR spectrum which was measured by SFG in reflection geometry from a z-cut quartz crystal.

## 5.3 Results and Discussion

**Hydration shell structure**

Interactions between water and solute molecules can be probed with Raman multivariate curve resolution (Raman-MCR)[79] to detect solute-correlated spectral changes in the O-H stretch band of water. For example, Raman-MCR has previously been used to detect water structure changes around benzene and other hydrophobic[133] and ionic[78] solutes. Here, we report results obtained with Raman-MCR that reveal differences between the hydration shell structures of $Ph_4B^-$ and

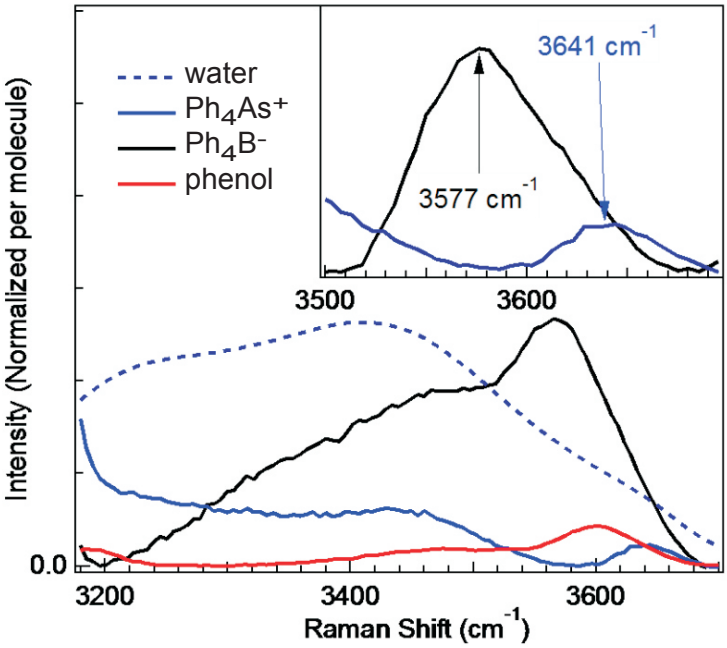


Figure 5.2: **Hydration shell spectra of oppositely charged but chemically identical ions.** The O-H stretch Raman intensity arising from the hydration shell of negatively charged $Ph_4B^-$ ions (black) and positively charged $Ph_4As^+$ ions (blue) are compared with that of the neutral aromatic phenol dissolved in water (red). The Raman spectrum of bulk water (dotted curve) is shown for reference (arbitrarily scaled to approximately the same height as the $Ph_4B^-$ spectrum). The inset figure shows the $\pi$-H-bond peaks of $Ph_4B^-$ (black) and $Ph_4As^+$ (blue), after subtraction of the H-bonded O-H background. The experimental concentrations of $Ph_4B^-$ and $Ph_4As^+$ were 0.1 M and that of phenol was 0.5 M; as each of the spectra were normalized to the respective C-H stretch band area (multiplied with the total number of C-H groups), all the spectra are effectively scaled to the same solute concentration.

$Ph_4As^+$. We also compare to the hydration shell of phenol, which has a single uncharged phenyl ring.

Figure 5.2 shows the hydration shell (solute-correlated Raman-MCR) spectra of the O-H stretch region of dilute solutions of $Ph_4B^-$ ions (black curve), $Ph_4As^+$ ions (blue curve), and phenol (red curve), all normalized to the same solute concentration, and for comparison, the O-H stretch band of bulk water (dashed curve, see the caption to Fig. 5.2 for further details). The $Na^+$ counterions have no observable effect on the water O-H band and the $Cl^-$ contribution to the hydration shell spectrum of $Ph_4As^+$ was removed by including NaCl in the water reference solution, at the same concentration as $Ph_4As^+$, as previously described[91].

The phenol spectrum displays a peak at $\sim$3600 cm$^{-1}$ that has been assigned in previous Raman[157] and gas phase cluster work[185] to a $\pi$-H-bond. Additionally, a weak red-shifted H-bonded O-H band[82] is visible. The number of $\pi$-H bonds per molecule can be estimated from the ratio of the area of the $\pi$-H-bonded O-H to that of the aromatic C-H stretch, combined with the previously reported theoretical estimate that a $\pi$-H-bonded O-H has a Raman cross section that is approximately 21% larger than that of an aromatic C-H[157]. The $\pi$-H-bonded O-H peak of $Ph_4B^-$ is red-shifted by 64 cm$^{-1}$ and has a $7 \pm 1$ times larger area than $Ph_4As^+$, implying that the $\pi$-H-bond between water and $Ph_4B^-$ is significantly stronger and more abundant than that of water to $Ph_4As^+$. More specifically, the area ratio of the $Ph_4B^-$ and $Ph_4As^+$ O-H peaks[174] shown in the inset panel in Fig. 5.2 implies that the $\pi$-H-bond to $Ph_4B^-$ is approximately $-kT\ln(7) \sim -2kT$ (-5 kJ/mol) stronger than the bond to $Ph_4As^+$. The observed significant red-shift of the $\pi$-H-bond O-H peak of $Ph_4B^-$ relative the peak of $Ph_4As^+$ further supports this finding, since a stronger H-bond weakens the O-H and therefore red-shifts the oscillators response. It is noteworthy that the probability of forming a $\pi$-H-bond to each one of the phenyl rings of the $Ph_4As^+$ cation is also about 5 times smaller than that to the neutral phenol molecule. Thus, the solvation shells of $Ph_4B^-$ and $Ph_4As^+$ are clearly different, with the $Ph_4As^+$ cation having far fewer and weaker $\pi$-H-bonds to water than the $Ph_4B^-$ anion. We now turn to the molecular structure of water and the ions at the hydrophobic oil-water interface.

### Probing interfacial charge and structure

To study the liquid oil-water interface, we used a nanoscopic dispersion of hexadecane ($C_{16}$) droplets in an aqueous solution that contained $Ph_4B^-$ or $Ph_4As^+$ ions. Such a system contains $\sim$3000 cm$^2$ of surface area per mL and is thus ideal to study liquid-liquid interfaces, because it allows for measurements with a high signal-to-noise ratio and is less prone to be affected by impurities. We estimated the surface charge with electrokinetic zeta potential measurements and probed $Ph_4B^-$ and $Ph_4As^+$ ions at the oil droplet-water interface with vibrational sum frequency scattering (SFS), a vibrational coherent surface spectroscopy that measures the combined IR and Raman spectrum of molecules, which can only give rise to signal in non-centrosymmetric environments such as interfaces[27,30,106]. Because of the azimuthal isotropy of the interface, SFS is only sensitive to chemical moieties that are oriented along the surface normal[50,139]. Vibrational modes associated with groups that lie in the surface plane are therefore not observed. The surface structure of water can be tracked with second harmonic scattering (SHS), that also

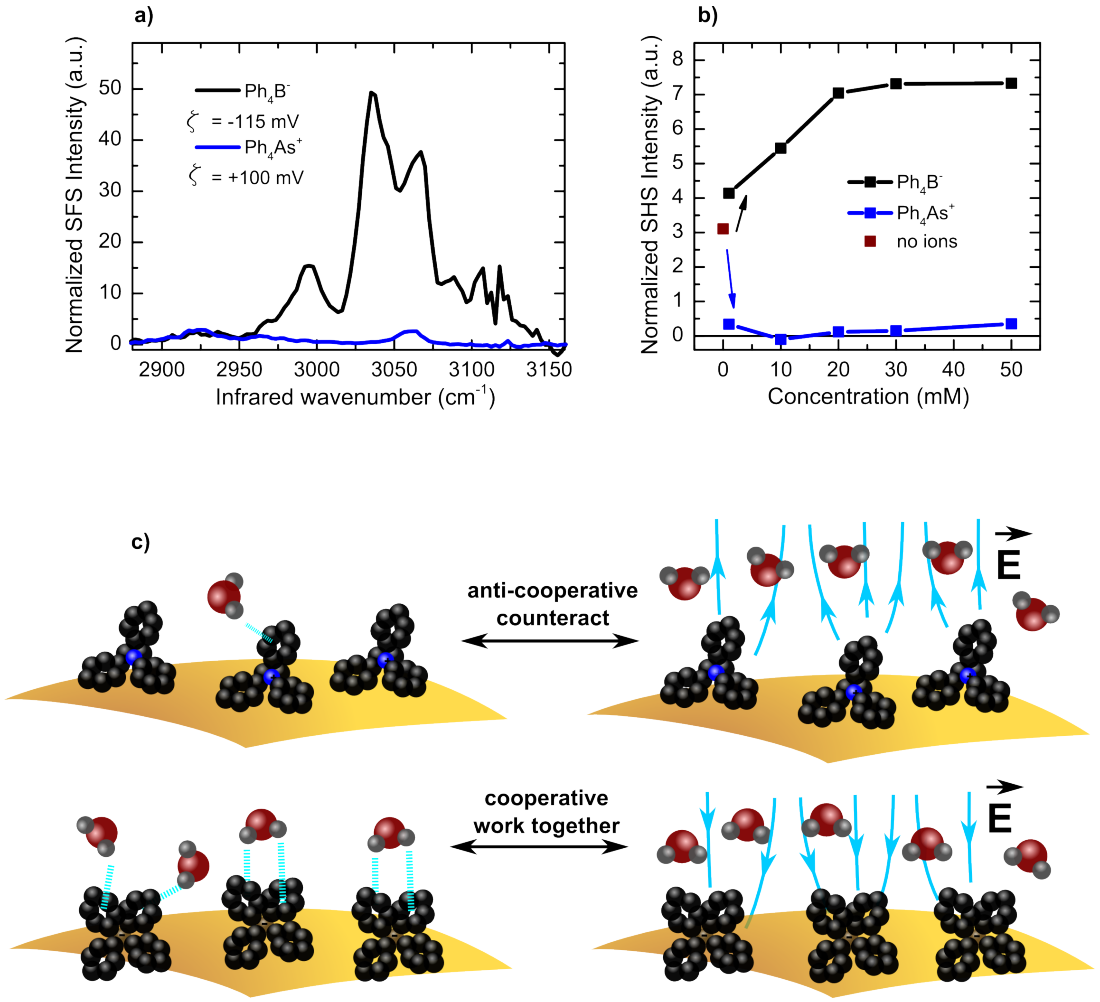


Figure 5.3: **Interfacial structure of $Ph_4$-ions.** (a): SFS spectra (ppp, all beams polarized in the plane of incidence) of the interface of oil nanodroplets in aqueous ($D_2O$) solutions of 10 mM of $Ph_4B^-$ (black) and $Ph_4As^+$ ions (blue). The spectra are normalized to the C-H stretch modes of the oil ($\sim$2935 $cm^{-1}$). (b): SHS signal intensity of dispersion of oil droplets in aqueous solution with varying concentrations of the ions in (a). The signal intensity in pp polarization combination was corrected for the hyper Rayleigh background signal and then normalized to the water signal in ss polarization combination. The red data point shows the response of the pure oil-water dispersion without any ions. The zeta potential of the pure oil droplets in water was $\sim$-50 mV. (c) Illustration of the difference in surface hydration: for negative ions, H-bonding and electrostatic interactions cooperate, while they counteract each other for positive ions.

occurs only in non-centrosymmetric regions. SHS probes anisotropically oriented water distributions in the interfacial region, as induced by an electric field or by the mere presence of the interface[73,131,186]. The H-bonding network, which is on average isotropic in the bulk liquid arranges quite different at interfaces[25,187]. Fig. 5.3a shows SFS spectra of hexadecane nanodroplets in solutions of 10 mM of $Ph_4B^-$ (black curve) and $Ph_4As^+$ (blue curve) in $D_2O$. The corresponding zeta potentials of the solutions were -100 mV and +115 mV, respectively, indicating that the droplets have a comparable interfacial charge density. The counterions $Na^+$ and $Cl^-$ are not interfacially active at a hydrophobic water interface[140]; thus, we assume that they do not influence the presented results. The SFS spectra display the C-H stretch modes of the phenyl rings of the tetraphenyl ions ($\gtrsim 2960\,cm^{-1}$), as well as the high frequency side of the interfacial hexadecane molecules ($\sim$2900-2950 $cm^{-1}$). The SFS spectra for $Ph_4B^-$ and $Ph_4As^+$ are similar below 2960 $cm^{-1}$, but above 2960 $cm^{-1}$, they are very different. First, the intensity of $Ph_4B^-$ is more than ten times larger than that of $Ph_4As^+$. Second, the spectral features differ significantly. The frequencies can be assigned to combined C-H ring stretch modes originating from the individual phenyl rings (for more details see Refs. 188–193). Fig. 5.3b shows the SHS intensities measured from droplet solutions prepared at different ion concentrations. The hyper rayleigh scattering background signal of the aqueous solutions without droplets was subtracted and the resulting difference was normalized to the response of water in ss polarization combination. As for the SFS signal, the SHS signal is also strikingly different, the SHS signal of the dispersion with $Ph_4B^-$ being large compared to that with $Ph_4As^+$. Below, we discuss these results in relation to the corresponding interfacial water structure, beginning with the SFS results.

### Asymmetric interface structure

$Ph_4As^+$ ions generate a much weaker SFS signal and a quite different spectral signature than the $Ph_4B^-$ ions, even though the interfacial number densities of both ions are comparable. The difference in signal therefore implies that the two ions adopt a very different structure at the surface of the oil droplet. A reason for the difference could be the distinct hydration behavior of the two ions, as shown by the solute-correlated Raman measurements. One might therefore expect the ions to also be differently hydrated at the oil-water interface. This distinct hydration behavior might drive $Ph_4As^+$ closer to the droplet surface than $Ph_4B^-$, thus affecting the orientation and the local environment of the phenyl rings. It may also be significant that the As-C bonds of $Ph_4As^+$ are more rotationally flexible

than the B-C bonds of $Ph_4B^-$ [194]. By slightly rotating the As-C axis of the phenyl rings of $Ph_4As^+$, its phenyl rings could lie more parallel to the interface, thus generating little or no SFS signal. How the water structure is affected can be seen by the SHS measurements (Fig. 5.3b). The results show that adsorption of $Ph_4B^-$ onto the droplet interface greatly increases the SHS signal with respect to the signal of the neat oil-water interface (red data point in Fig.5.3b). This increase implies that the total orientational anisotropy of water molecules is enhanced by $Ph_4B^-$ ions at the interface. In contrast, the positively charged $Ph_4As^+$ ions remove the water orientation present on the neat oil-water interface, producing virtually the same SHS signal as an aqueous solution of $Ph_4As^+$ without any oil droplets. The hydrogen atoms of water act as donors when they form a $\pi$-H-bond with the phenyl rings. Because of H-bonding it would be thus favorable for water molecules to be oriented with their hydrogen atoms towards the phenyl rings, as depicted in Fig. 5.3c. For a negatively charged interface, the electric field tends to orient water molecules in the same way because of the interaction of the field with the water dipoles. However, a positive surface charge tends to orient water molecules such that the oxygen points towards the surface. Thus, H-bonding and charge-dipole interaction work together in the case of the negative $Ph_4B^-$ ions but rather counteract each other for positive $Ph_4As^+$ ions. This is consistent with our observation that $Ph_4B^-$ forms more and stronger hydrogen bonds to water, while the counteracting charge-dipole interaction weakens the H-bonds to $Ph_4As^+$. At the oil droplet-water interface this specific orientation of water molecules around the ions results in the strikingly different water structures, as observed in the SHS signal. If the negative $Ph_4B^-$ ions are present at the interface, this generates a greater degree of water anisotropy (directionality). In the case of positive $Ph_4As^+$ ions at the interface, the counteracting interactions result in a vanishing interfacial water anisotropy. It is remarkable that the initial anisotropy of the water molecules on the neat surface vanishes already at low bulk concentrations of $Ph_4As^+$. In contrast, the SHS signal increases with concentration, but beyond a certain $Ph_4B^-$ concentration ($\sim$20 mM) the increase levels off, because the greater ionic strength of the solution screens the surface electric field more effectively, thereby reducing the amount of water that is orienationally affected.

## 5.4 Conclusion

In summary, we have quantified the charge asymmetry associated with the hydration of two oppositely charged but otherwise virtually identical ions in water and on a hydrophobic water interface. Raman-MCR results revealed that water forms far

fewer and weaker $\pi$-H-bonds to the positively charged tetraphenylarsonium ion than to the negatively charged tetraphenylborate ion. Our SFS and SHS results further show that the two ions adopt quite different structures and induce strikingly different interfacial water structures at an oil-water interface. Our observations can be consistently explained by cooperating (for negative ions) and anti-cooperative (for positive ions) electrostatic and H-bonding interactions.

Our findings show on a molecular level how inherent charge asymmetries arise; this could explain the predominance of the negative charge, as observed on oil droplets, air bubbles and many biological interfaces.

# Conclusion and Outlook

This thesis addresses key phenomena at hydrophobic aqueous interfaces. With sum frequency and second harmonic scattering, a detailed molecular-scale view of ion-specific, amphiphile-specific, and charge-specific effects at nanoscopic hydrophobic interfaces is obtained. The results demonstrate distinct features of the molecular-level interfacial structure; these features stem from specific interactions with water and are apparent in the distinct water structure at the interface. The aspects that have been covered range from hydrophobic effects (Ch. 3) over specific amphiphile effects (Ch. 4) to inherent charge asymmetries in the ion-water interaction (Ch. 5).

In a series of tetraalkylammonium ($TAA^+$) ions with increasing size, we studied the influence of an increased hydrophobic interaction of these ions with the hydrophobic surface of dodecylsulfate ($DS^-$)-stabilized oil nanodroplets. The adsorption of the large $TBA^+$ and $TPA^+$ ions to the surface and thus the formation of a Stern layer could be followed; the employed methods allowed capturing the structure of amphiphiles, hydrophobic counterions, and interfacial water. This revealed that the Stern layer is rather a mixed zwitterionic $TAA^+/DS^-$ monolayer than a capacitor-like double layer. In this monolayer, amphiphiles and surface-active counterions do not compete for empty surface sites. Moreover, the transition from bulk-active to surface-active has been determined to happen at a size of the cations of around $\sim$1 nm, consistent with the typical length scale at which a hydrophobic crossover from small to large solutes is expected.

Ionic amphiphiles that contain equal alkyl chains, but opposite charge and dissimilar head groups have been investigated. Those amphiphiles lower the surface tension by the same amount, thus indicating a similar microscopic mechanism. However, as revealed by our study, they induce strikingly different molecular conformations in the interfacial oil layer. Moreover, the alkyl chain conformation of the amphiphiles remarkably differs. The differences can be correlated with the Hofmeister ordering of ions, suggesting an analogous ordering for functional head groups of amphiphiles. The results show that the ionic head groups interact distinctly with the water phase, demonstrating that the molecular mechanism of

interfacial stabilization is quite different.
The insights gained about the structuring of amphiphiles at hydrophobic interfaces could in the future be further refined; phospholipids, the building units of the membrane bilayer, are also amphiphilic molecules that can contain a number of different functional groups. Future studies will try to reveal mechanisms involved when different phospholipds adsorb to hydrophobic (charged) interfaces. Ultimately, this research aims at a complete understanding of specific effects at protein interfaces. The balance of hydrophilic and hydrophobic forces is subtle in a biological environment. Model systems will therefore need to systematically study chain length effects and the influence of temperature on the interfacial structure. For instance, although the interaction of the hydrophobic phase with $DTA^+$ was shown to be much stronger than that with $DS^-$, some interaction has to exist that could appear in refined measurements. Preliminary data indicates that a small change in the conformation of the oil phase is induced when $DS^-$ ions adsorb to the hydrophobic interface. Those effects might become more clear using amphiphiles with the same headgroup as in $DS^-$ but with longer alkyl chains, or at different temperatures. Systematic measurements that further elucidate this issue will also provide insights into whether the differences found are due to the opposite charge, the difference in hydrogen bonding propensity, or both.

Such a charge asymmetry is expressed in the preference of many 'natural' interfaces to appear negatively charged — for example, the neat oil-water and air-water interfaces. In this thesis we also quantified an inherent charge asymmetry at an aqueous hydrophobic interface. Tetraphenylarsonium and tetraphenylborate ions, which are chemically virtually identical but of opposite charge, were shown to have distinct hydration behaviors in bulk solution and at the hydrophobic oil-water interface. The here obtained results demonstrate how intrinsic charge asymmetries arise through the H-bonding propensity of water and thus provide important clues on the natural preference for negative charge at aqueous interfaces.

In this thesis, we also presented a key step towards the study of vibrational dynamics at liquid-liquid and buried nanoscopic interfaces. Future studies will therefore address the vibrational dynamics of many of the systems that have been described here. All the presented phenomena stem from distinct interactions with water molecules and concern the structure of water near interfaces; it will therefore be insightful to also access the vibrational dynamics of water molecules at hydrophobic liquid-liquid interfaces.

**Publications**

The present thesis is based on the following manuscripts / publications:

- Rüdiger Scheu and Sylvie Roke, *Towards vibrational dynamics at liquid-liquid and nano-interfaces: Time-resolved Sum Frequency Scattering*, submitted, 2013.

- Rüdiger Scheu, Yixing Chen, Mireia Subinya, and Sylvie Roke, *Stern layer formation induced by hydrophobic interactions: a molecular level study*, J. Am. Chem. Soc., 2013, 135(51), pp 19330-19335.

- Rüdiger Scheu, Hilton B. de Aguiar, Blake M. Rankin, Dor Ben-Amotz, and Sylvie Roke, *Specific ion effects in amphiphile hydration and interface stabilization*, J. Am. Chem. Soc., 2014 accepted, DOI: 10.1021/ja4120117

- Rüdiger Scheu, Blake M. Rankin, Yixing Chen, Kailash C. Jena, Dor Ben-Amotz, and Sylvie Roke, *Charge Asymmetry at Aqueous Hydrophobic Interfaces and Hydration-Shells*, submitted, 2013.

Other publications not described within this thesis:

- Hilton B. de Aguiar, Rüdiger Scheu, Kailash C. Jena, Alex G. F. de Beer, and Sylvie Roke, *Comparison of scattering and reflection SFG: a question of phase-matching.*, Phys. Chem. Chem. Phys., 12:6828.6832, 2012.

- Kailash C. Jena, Rüdiger Scheu and Sylvie Roke, *Surface impurities are not responsible for the charge on the oil/water interface: A comment.*, Ang.Chemie, 51(52):12938-12940, 2012.

- Alex G. F. de Beer, Yixing Chen, Rüdiger Scheu, John Conboy, and Sylvie Roke, *Analysis of Complex Sum Frequency Spectra Using Fourier Filtering*, J. Phys. Chem. C, accepted, 2013.

Publications in non-peer-reviewed popular journals

- Rüdiger Scheu and Sylvie Roke, *Eingeseift vom falschen Modell*, Physik in unserer Zeit, 03/2011, 137-143.

# Bibliography


[1] J. da Silva and R. Williams, *The Biological Chemistry of the Elements: The Inorganic Chemistry of Life*. OUP Oxford, 2001.

[2] W.-k. Zhang, H.-f. Wang, and D.-s. Zheng, "Quantitative measurement and interpretation of optical second harmonic generation from molecular interfaces," *Phys. Chem. Chem. Phys.*, vol. 8, no. 35, 2006.

[3] W. Kunz, *Specific Ion Effects*. World Scientific Publishing Company, 2009.

[4] P. Lo Nostro and B. W. Ninham, "Hofmeister phenomena: An update on ion specificity in biology," *Chem. Rev.*, vol. 112, no. 4, pp. 2286–2322, 2012.

[5] Y. Marcus, "Effect of ions on the structure of water: Structure making and breaking," *Chem. Rev.*, vol. 109, no. 3, pp. 1346–1370, 2009.

[6] W. Kunz, "Specific ion effects in colloidal and biological systems," *Curr. Opin. Colloid Interface Sci.*, vol. 15, no. 1-2, pp. 34 – 39, 2010.

[7] N. Schwierz, D. Horinek, and R. R. Netz, "Anionic and cationic Hofmeister effects on hydrophobic and hydrophilic surfaces," *Langmuir*, vol. 29, no. 8, pp. 2602–2614, 2013.

[8] F. Hofmeister, "Zur Lehre von der Wirkung der Salze," *Arch. Exp. Pathol. Pharmakol.*, vol. 24, pp. 247–260, 1888.

[9] D. J. Tobias and J. C. Hemminger, "Getting specific about specific ion effects," *Science*, vol. 319, no. 5867, pp. 1197–1198, 2008.

[10] A. J. Patel, P. Varilly, S. N. Jamadagni, H. Acharya, S. Garde, and D. Chandler, "Extended surfaces modulate hydrophobic interactions of neighboring solutes," *Proc. Natl. Acad. Sci.*, vol. 108, no. 43, pp. 17678–17683, 2011.

[11] R. R. Netz and D. Horinek, "Progress in modeling of ion effects at the vapor/water interface," *Annu. Rev. Phys. Chem.*, vol. 63, no. 1, pp. 401–418, 2012.

[12] M. Lund, P. Jungwirth, and C. E. Woodward, "Ion specific protein assembly and hydrophobic surface forces," *Phys. Rev. Lett.*, vol. 100, p. 258105, 2008.

[13] L. R. Pratt and A. Pohorille, "Hydrophobic effects and modeling of biophysical aqueous solution interfaces," *Chem. Rev.*, vol. 102, no. 8, pp. 2671–2692, 2002.

[14] J. J. Kuna, K. Voitchovsky, C. Singh, H. Jiang, S. Mwenifumbo, P. K. Ghorai, M. M.

Stevens, S. C. Glotzer, and F. Stellacci, "The effect of nanometre-scale structure on interfacial energy," *Nat. Mater.*, vol. 8, no. 10, pp. 837–842, 2009.

[15] H. Acharya, S. Vembanur, S. N. Jamadagni, and S. Garde, "Mapping hydrophobicity at the nanoscale: Applications to heterogeneous surfaces and proteins," *Faraday Discuss.*, vol. 146, pp. 353–365, 2010.

[16] S. N. Jamadagni, R. Godawat, and S. Garde, "Hydrophobicity of proteins and interfaces: Insights from density fluctuations," *Annu. Rev. Chem. Biomol. Eng.*, vol. 2, no. 1, pp. 147–171, 2011.

[17] A. W. Adamson and A. P. Gast, *Physical chemistry of surfaces*. J. Wiley, 6 ed., 1997.

[18] M. L. Schlossman, "Liquid-liquid interfaces: studied by X-ray and neutron scattering," *Curr. Opin. Colloid Interface Sci.*, vol. 7, no. 3-4, pp. 235 – 243, 2002.

[19] P. S. Pershan and M. L. Schlossman, *Liquid surfaces and interfaces: Synchrotron X-ray methods*. Cambridge University Press, 2012.

[20] Y. R. Shen, "Surface properties probed by second-harmonic and sum-frequency generation," *Nature*, vol. 337, no. 6207, pp. 519–525, 1989.

[21] K. B. Eisenthal, "Liquid interfaces probed by second-harmonic and sum-frequency spectroscopy," *Chem. Rev.*, vol. 96, no. 4, pp. 1343–1360, 1996.

[22] A. M. Jubb, W. Hua, and H. C. Allen, "Environmental chemistry at vapor/water interfaces: Insights from vibrational sum frequency generation spectroscopy," *Annu. Rev. Phys. Chem.*, vol. 63, no. 1, pp. 107–130, 2012.

[23] Y. Zhang and P. S. Cremer, "Chemistry of Hofmeister anions and osmolytes," *Annu. Rev. Phys. Chem.*, vol. 61, no. 1, pp. 63–83, 2010.

[24] S. C. Flores, J. Kherb, and P. S. Cremer, "Direct and reverse Hofmeister effects on interfacial water structure," *J. Phys. Chem. C*, vol. 116, no. 27, pp. 14408–14413, 2012.

[25] L. F. Scatena, M. G. Brown, and G. L. Richmond, "Water at hydrophobic surfaces: Weak hydrogen bonding and strong orientation effects," *Science*, vol. 292, no. 5518, pp. 908–912, 2001.

[26] M. Bonn and R. K. Campen, "Optical methods for the study of dynamics in biological membrane models," *Surf. Sci.*, vol. 603, no. 10-12, pp. 1945–1952, 2009.

[27] S. Roke, "Nonlinear optical spectroscopy of soft matter interfaces," *ChemPhysChem*, vol. 10, no. 9-10, pp. 1380–1388, 2009.

[28] S. Roke, W. G. Roeterdink, J. E. G. J. Wijnhoven, A. V. Petukhov, A. W. Kleyn, and M. Bonn, "Vibrational sum frequency scattering from a submicron suspension," *Phys. Rev. Lett.*, vol. 91, no. 25, p. 258302, 2003.

[29] M. L. Strader, H. B. de Aguiar, A. G. F. de Beer, and S. Roke, "Label-free spectro-

scopic detection of vesicles in water using vibrational sum frequency scattering," *Soft Matter*, vol. 7, pp. 4959–4963, 2011.

[30] H. B. de Aguiar, A. G. F. de Beer, M. L. Strader, and S. Roke, "The interfacial tension of nanoscopic oil droplets in water is hardly affected by SDS surfactant," *J. Am. Chem. Soc.*, vol. 132, no. 7, pp. 2122–2123, 2010.

[31] H. B. de Aguiar, M. L. Strader, A. G. F. de Beer, and S. Roke, "Surface structure of sodium dodecyl sulfate surfactant and oil at the Oil-in-Water droplet Liquid/Liquid interface: A manifestation of a nonequilibrium surface state," *J. Phys. Chem. B*, vol. 115, no. 12, pp. 2970–2978, 2011.

[32] K. C. Jena, R. Scheu, and S. Roke, "Surface impurities are not responsible for the charge on the oil/water interface: A comment," *Angew. Chem.*, vol. 51, no. 52, pp. 12938–12940, 2012.

[33] H. B. de Aguiar, R. Scheu, K. C. Jena, A. G. F. de Beer, and S. Roke, "Comparison of scattering and reflection SFG: a question of phase-matching," *Phys. Chem. Chem. Phys.*, vol. 14, pp. 6826–6832, 2012.

[34] D. Chandler, "Interfaces and the driving force of hydrophobic assembly," *Nature*, vol. 437, no. 7059, pp. 640–647, 2005.

[35] J. K. Beattie, A. M. Djerdjev, and G. G. Warr, "The surface of neat water is basic," *Faraday Discuss.*, vol. 141, p. 31, 2009.

[36] F. Hofmeister, "Zur Lehre von der Wirkung der Salze," *Arch. Exp. Pathol. Pharmakol.*, vol. 25, no. 1, pp. 1–30, 1888.

[37] W. Kunz, P. L. Nostro, and B. Ninham, "The present state of affairs with Hofmeister effects," *Curr. Opin. Colloid Interface Sci.*, vol. 9, no. 1-2, pp. 1 – 18, 2004.

[38] R. G. Pearson, "Hard and soft acids and bases," *J. Am. Chem. Soc.*, vol. 85, no. 22, pp. 3533–3539, 1963.

[39] R. G. Parr and R. G. Pearson, "Absolute hardness: companion parameter to absolute electronegativity," *J. Am. Chem. Soc.*, vol. 105, no. 26, pp. 7512–7516, 1983.

[40] L. Vrbka, M. Mucha, B. Minofar, P. Jungwirth, E. C. Brown, and D. J. Tobias, "Propensity of soft ions for the air/water interface," *Curr. Opin. Colloid Interface Sci.*, vol. 9, no. 1-2, pp. 67 – 73, 2004.

[41] K. Collins, "Charge density-dependent strength of hydration and biological structure," *Biophys. J.*, vol. 72, no. 1, pp. 65 – 76, 1997.

[42] K. D. Collins, "Ions from the Hofmeister series and osmolytes: effects on proteins in solution and in the crystallization process," *Methods*, vol. 34, no. 3, pp. 300 – 311, 2004.

[43] K. J. Tielrooij, N. Garcia-Araez, M. Bonn, and H. J. Bakker, "Cooperativity in ion hydration," *Science*, vol. 328, no. 5981, pp. 1006–1009, 2010.

[44] D. Horinek, A. Herz, L. Vrbka, F. Sedlmeier, S. I. Mamatkulov, and R. R. Netz, "Specific ion adsorption at the air/water interface: The role of hydrophobic solvation," *Chem. Phys. Lett.*, vol. 479, no. 4-6, pp. 173 – 183, 2009.

[45] K. Lum, D. Chandler, and J. D. Weeks, "Hydrophobicity at small and large length scales," *J. Phys. Chem. B*, vol. 103, no. 22, pp. 4570–4577, 1999.

[46] N. Huang, D. Schlesinger, D. Nordlund, C. Huang, T. Tyliszczak, T. M. Weiss, Y. Acremann, L. G. M. Pettersson, and A. Nilsson, "Microscopic probing of the size dependence in hydrophobic solvation," *J. Chem. Phys.*, vol. 136, no. 7, p. 074507, 2012.

[47] J. G. Davis, B. M. Rankin, K. P. Gierszal, and D. Ben-Amotz, "On the cooperative formation of non-hydrogen-bonded water at molecular hydrophobic interfaces," *Nat Chem*, vol. 5, no. 9, pp. 796–802, 2013.

[48] G. Luo, S. Malkova, J. Yoon, D. G. Schultz, B. Lin, M. Meron, I. Benjamin, P. Vanýsek, and M. L. Schlossman, "Ion distributions near a liquid-liquid interface," *Science*, vol. 311, no. 5758, pp. 216–218, 2006.

[49] J. M. Berg, J. L. Tymoczko, and L. Stryer, *Biochemistry.* New York: W H Freeman, 2002.

[50] A. G. F. de Beer and S. Roke, "Obtaining molecular orientation from second harmonic and sum frequency scattering experiments in water: Angular distribution and polarization dependence," *J. Chem. Phys.*, vol. 132, no. 23, p. 234702, 2010.

[51] P. Butcher and D. Cotter, *The Elements of Nonlinear Optics.* Cambridge Studies in Modern Optics, Cambridge University Press, 1991.

[52] Y. Shen, *The principles of nonlinear optics.* Wiley classics library, Wiley-Interscience, 2003.

[53] J. Jackson, *Classical electrodynamics.* Wiley, 1975.

[54] P. S. Pershan, "Nonlinear optical properties of solids: Energy considerations," *Phys. Rev.*, vol. 130, no. 3, p. 919, 1963.

[55] J. I. Dadap, J. Shan, and T. F. Heinz, "Theory of optical second-harmonic generation from a sphere of centrosymmetric material: small-particle limit," *J. Opt. Soc. Am. B*, vol. 21, no. 7, pp. 1328–1347, 2004.

[56] P. Guyot-Sionnest, W. Chen, and Y. R. Shen, "General considerations on optical second-harmonic generation from surfaces and interfaces," *Phys. Rev. B*, vol. 33, no. 12, p. 8254, 1986.

[57] H. Held, A. I. Lvovsky, X. Wei, and Y. R. Shen, "Bulk contribution from isotropic media in surface sum-frequency generation," *Phys. Rev. B*, vol. 66, no. 20, p. 205110, 2002.

[58] R. Bersohn, Y.-H. Pao, and H. L. Frisch, "Double-quantum light scattering by

molecules," *J. Chem. Phys.*, vol. 45, no. 9, pp. 3184–3198, 1966.

[59] D. P. Shelton and J. E. Rice, "Measurements and calculations of the hyperpolarizabilities of atoms and small molecules in the gas phase," *Chem. Rev.*, vol. 94, no. 1, pp. 3–29, 1994.

[60] N. Gomopoulos, C. Lütgebaucks, Q. Sun, C. Macias-Romero, and S. Roke, "Label-free second harmonic and hyper rayleigh scattering with high efficiency," *Opt. Express*, vol. 21, no. 1, pp. 815–821, 2013.

[61] C. Hirose, N. Akamatsu, and K. Domen, "Formulas for the analysis of surface sum-frequency generation spectrum by CH stretching modes of methyl and methylene groups," *J. Chem. Phys.*, vol. 96, p. 997, 1992.

[62] A. G. F. de Beer and S. Roke, "Sum frequency generation scattering from the interface of an isotropic particle: Geometrical and chiral effects," *Phys. Rev. B*, vol. 75, no. 24, p. 245438, 2007.

[63] B. Busson and A. Tadjeddine, "Non-uniqueness of parameters extracted from resonant Second-Order nonlinear optical spectroscopies," *J. Phys. Chem. C*, vol. 113, no. 52, pp. 21895–21902, 2009.

[64] A. G. F. de Beer, J.-S. Samson, W. Hua, Z. Huang, X. Chen, H. C. Allen, and S. Roke, "Direct comparison of phase-sensitive vibrational sum frequency generation with maximum entropy method: Case study of water," *J. Chem. Phys.*, vol. 135, no. 22, pp. –, 2011.

[65] A. G. F. de Beer, Y. Chen, R. Scheu, J. C. Conboy, and S. Roke, "Analysis of complex spectra using fourier filtering," *J. Phys. Chem. C*, vol. 117, no. 50, pp. 26582–26587, 2013.

[66] N. Ji, V. Ostroverkhov, C.-Y. Chen, and Y.-R. Shen, "Phase-sensitive sum-frequency vibrational spectroscopy and its application to studies of interfacial alkyl chains," *J. Am. Chem. Soc.*, vol. 129, no. 33, pp. 10056–10057, 2007.

[67] C. Humbert, O. Pluchery, E. Lacaze, A. Tadjeddine, and B. Busson, "A multiscale description of molecular adsorption on gold nanoparticles by nonlinear optical spectroscopy," *Phys. Chem. Chem. Phys.*, vol. 14, pp. 280–289, 2012.

[68] A. N. Bordenyuk, H. Jayathilake, and A. V. Benderskii, "Coherent vibrational quantum beats as a probe of Langmuir-Blodgett monolayers," *J. Phys. Chem. B*, vol. 109, no. 33, pp. 15941–15949, 2005.

[69] S. Nihonyanagi, A. Eftekhari-Bafrooei, and E. Borguet, "Ultrafast vibrational dynamics and spectroscopy of a siloxane self-assembled monolayer," *J. Chem. Phys.*, vol. 134, p. 084701, 2011.

[70] A. J. Moad and G. J. Simpson, "A unified treatment of selection rules and symmetry relations for Sum-Frequency and second harmonic spectroscopies," *J. Phys. Chem. B*, vol. 108, no. 11, pp. 3548–3562, 2004.

[71] K. Clays and A. Persoons, "Hyper-rayleigh scattering in solution," *Phys. Rev. Lett.*, vol. 66, pp. 2980–2983, 1991.

[72] B. Schürer, S. Wunderlich, C. Sauerbeck, U. Peschel, and W. Peukert, "Probing colloidal interfaces by angle-resolved second harmonic light scattering," *Phys. Rev. B*, vol. 82, no. 24, p. 241404, 2010.

[73] K. C. Jena, P. A. Covert, and D. K. Hore, "The effect of salt on the water structure at a charged solid surface: Differentiating second- and third-order nonlinear contributions," *J. Phys. Chem. Lett.*, vol. 2, no. 9, pp. 1056–1061, 2011.

[74] S. Ong, X. Zhao, and K. B. Eisenthal, "Polarization of water molecules at a charged interface: second harmonic studies of the silica/water interface," *Chem. Phys. Lett.*, vol. 191, no. 3-4, pp. 327–335, 1992.

[75] S. Roke, M. Bonn, and A. V. Petukhov, "Nonlinear optical scattering: The concept of effective susceptibility," *Phys. Rev. B*, vol. 70, no. 11, p. 115106, 2004.

[76] "Solute-correlated raman spectroscopy. http://www.chem.purdue.edu/bendor/research2.html."

[77] W. H. Lawton and E. A. Sylvestre, "Self modeling curve resolution," *Technometrics*, vol. 13, no. 3, pp. 617–633, 1971.

[78] P. N. Perera, B. Browder, and D. Ben-Amotz, "Perturbations of water by alkali halide ions measured using multivariate raman curve resolution," *J. Phys. Chem. B*, vol. 113, no. 7, pp. 1805–1809, 2009.

[79] K. R. Fega, D. S. Wilcox, and D. Ben-Amotz, "Application of raman multivariate curve resolution to solvation-shell spectroscopy," *Appl. Spectrosc.*, vol. 66, no. 3, pp. 282–288, 2012.

[80] K. Awa, T. Okumura, H. Shinzawa, M. Otsuka, and Y. Ozaki, "Self-modeling curve resolution (SMCR) analysis of near-infrared (NIR) imaging data of pharmaceutical tablets," *Analytica Chimica Acta*, vol. 619, no. 1, pp. 81 – 86, 2008.

[81] B. M. Auer and J. L. Skinner, "IR and Raman spectra of liquid water: Theory and interpretation," *J. Chem. Phys.*, vol. 128, no. 22, pp. –, 2008.

[82] C. J. Tainter, Y. Ni, L. Shi, and J. L. Skinner, "Hydrogen bonding and OH-stretch spectroscopy in water: Hexamer (cage), liquid surface, liquid, and ice," *J. Phys. Chem. Lett.*, vol. 4, no. 1, pp. 12–17, 2013.

[83] J. R. Scherer, M. K. Go, and S. Kint, "Raman spectra and structure of water from -10 to 90.deg.," *J. Phys. Chem.*, vol. 78, no. 13, pp. 1304–1313, 1974.

[84] R. Borsali and R. Pecora, *Soft-Matter Characterization*. Soft Matter Characterization, Springer, 2008.

[85] Malvern Instruments, *Zetasizer Nano Series User Manual*, 0317, issue 1.1 ed., 2004.

[86] R. Hunter, *Zeta Potential in Colloid Science: Principles and Applications*. Colloid science, Academic Press, 1988.

[87] R. J. Hunter, *Foundations of Colloid Science.* Oxford University Press, USA, 2 ed., 2001.

[88] P. Guyot-Sionnest, "Coherent processes at surfaces: Free-induction decay and photon echo of the Si-H stretching vibration for H/Si(111)," *Phys. Rev. Lett.*, vol. 66, no. 11, p. 1489, 1991.

[89] J. C. Owrutsky, J. P. Culver, M. Li, Y. R. Kim, M. J. Sarisky, M. S. Yeganeh, A. G. Yodh, and R. M. Hochstrasser, "Femtosecond coherent transient infrared spectroscopy of CO on cu(111)," *J. Chem. Phys.*, vol. 97, no. 6, p. 4421, 1992.

[90] S. Roke, A. W. Kleyn, and M. Bonn, "Time- vs. frequency-domain femtosecond surface sum frequency generation," *Chem. Phys. Lett.*, vol. 370, no. 1-2, pp. 227–232, 2003.

[91] B. M. Rankin, M. D. Hands, D. S. Wilcox, K. R. Fega, L. V. Slipchenko, and D. Ben-Amotz, "Interactions between halide anions and a molecular hydrophobic interface," *Faraday Discuss.*, 2013.

[92] M. T. Zanni and R. M. Hochstrasser, "Two-dimensional infrared spectroscopy: a promising new method for the time resolution of structures," *Curr. Opin. Struct. Biol.*, vol. 11, no. 5, pp. 516 – 522, 2001.

[93] H. Arnolds, "Vibrational dynamics of adsorbates - quo vadis?," *Prog. Surf. Sci.*, vol. 86, no. 1-2, pp. 1 – 40, 2011.

[94] C. Hsieh, R. K. Campen, A. C. Vila Verde, P. Bolhuis, H. Nienhuys, and M. Bonn, "Ultrafast reorientation of dangling OH groups at the Air-Water interface using femtosecond vibrational spectroscopy," *Phys. Rev. Lett.*, vol. 107, no. 11, p. 116102, 2011.

[95] F. Vidal and A. Tadjeddine, "Sum-frequency generation spectroscopy of interfaces," *Rep. Prog. Phys.*, vol. 68, no. 5, pp. 1095–1127, 2005.

[96] H. Arnolds and M. Bonn, "Ultrafast surface vibrational dynamics," *Surf. Sci. Rep.*, vol. 65, no. 2, pp. 45–66, 2010.

[97] S. Roke, A. W. Kleyn, and M. Bonn, "Ultrafast surface dynamics studied with femtosecond sum frequency generation," *J. Phys. Chem. A*, vol. 105, no. 10, pp. 1683–1686, 2001.

[98] M. Bonn, C. Hess, and M. Wolf, "The dynamics of vibrational excitations on surfaces: Co on ru(001)," *J. Chem. Phys.*, vol. 115, no. 16, pp. 7725–7735, 2001.

[99] A. N. Bordenyuk and A. V. Benderskii, "Spectrally- and time-resolved vibrational surface spectroscopy: Ultrafast hydrogen-bonding dynamics at D2O/CaF2 interface," *J. Chem. Phys.*, vol. 122, no. 13, p. 134713, 2005.

[100] R. Trebino, "Frog," in *Frequency-Resolved Optical Gating: The Measurement of Ultrashort Laser Pulses*, pp. 101–115, Springer US, 2000.

[101] J. E. Bertie, M. K. Ahmed, and H. H. Eysel, "Infrared intensities of liquids. 5. Optical and dielectric constants, integrated intensities, and dipole moment derivatives of water and water-d2 at 22 deg C," *J. Phys. Chem.*, vol. 93, no. 6, pp. 2210–2218, 1989.

[102] S. Mukamel, *Principles of Nonlinear Optical Spectroscopy.* Oxford University Press: New York, 1995.

[103] J. Diels and W. Rudolph, *Ultrashort Laser Pulse Phenomena.* Optics and photonics, Elsevier Science, 2006.

[104] B. Efron and R. Tibshirani, *An Introduction to the Bootstrap.* Chapman & Hall/CRC Monographs on Statistics & Applied Probability, Taylor & Francis, 1994.

[105] E. Tyrode and J. Hedberg, "A comparative study of the CD and CH stretching spectral regions of typical surfactants systems using VSFS: Orientation analysis of the terminal CH3 and CD3 groups," *J. Phys. Chem. C*, vol. 116, no. 1, pp. 1080–1091, 2012.

[106] A. G. Lambert, P. B. Davies, and D. J. Neivandt, "Implementing the theory of sum frequency generation vibrational spectroscopy: A tutorial review.," *Appl. Spectrosc. Rev.*, vol. 40, no. 2, pp. 103–145, 2005.

[107] G. R. Bell, C. D. Bain, and R. N. Ward, "Sum-frequency vibrational spectroscopy of soluble surfactants at the air/water interface," *J. Chem. Soc., Faraday Trans.*, vol. 92, no. 4, pp. 515–523, 1996.

[108] M. C. Messmer, J. C. Conboy, and G. L. Richmond, "Observation of molecular ordering at the liquid-liquid interface by resonant sum frequency generation," *J. Am. Chem. Soc.*, vol. 117, no. 30, pp. 8039–8040, 1995.

[109] H. Wang, E. C. Y. Yan, E. Borguet, and K. B. Eisenthal, "Second harmonic generation from the surface of centrosymmetric particles in bulk solution," *Chem. Phys. Lett.*, vol. 259, no. 1-2, pp. 15–20, 1996.

[110] C. M. Johnson and E. Tyrode, "Study of the adsorption of sodium dodecyl sulfate (SDS) at the air/water interface: targeting the sulfate headgroup using vibrational sum frequency spectroscopy," *Phys. Chem. Chem. Phys.*, vol. 7, no. 13, p. 2635, 2005.

[111] M. Picquart, "Vibrational model behavior of SDS aqueous solutions studied by raman scattering," *J. Phys. Chem.*, vol. 90, no. 2, pp. 243–250, 1986.

[112] A. J. Prosser and E. I. Franses, "Infrared reflection absorption spectroscopy (IRRAS) of aqueous nonsurfactant salts, ionic surfactants, and mixed ionic surfactants," *Langmuir*, vol. 18, no. 24, pp. 9234–9242, 2002.

[113] M. C. Gurau, S.-M. Lim, E. T. Castellana, F. Albertorio, S. Kataoka, and P. S. Cremer, "On the mechanism of the Hofmeister effect," *J. Am. Chem. Soc.*, vol. 126, no. 34, pp. 10522–10523, 2004.

[114] P. Jungwirth and D. J. Tobias, "Specific ion effects at the Air/Water interface," *Chem. Rev.*, vol. 106, no. 4, pp. 1259–1281, 2006.

[115] W. Blokzijl and J. B. F. N. Engberts, "Hydrophobic effects. opinions and facts," *Angew. Chem.*, vol. 32, no. 11, pp. 1545–1579, 1993.

[116] M. Gradzielski, "Investigations of the dynamics of morphological transitions in amphiphilic systems," *Curr. Opin. Colloid Interface Sci.*, vol. 9, no. 3-4, pp. 256–263, 2004.

[117] W.-k. Zhang, D.-s. Zheng, Y.-y. Xu, H.-t. Bian, Y. Guo, and H.-f. Wang, "Reconsideration of second-harmonic generation from isotropic liquid interface: Broken Kleinman symmetry of neat air/water interface from dipolar contribution," *J. Chem. Phys.*, vol. 123, p. 224713, 2005.

[118] C. Tanford, *The Hydrophobic Effect: Formation of Micelles and Biological Membranes*. Wiley-Interscience: New York, 1973.

[119] B. Winter, R. Weber, P. M. Schmidt, I. V. Hertel, M. Faubel, L. Vrbka, and P. Jungwirth, "Molecular structure of surface-active salt solutions: Photoelectron spectroscopy and molecular dynamics simulations of aqueous tetrabutylammonium iodide," *J. Phys. Chem. B*, vol. 108, no. 38, pp. 14558–14564, 2004.

[120] D. Horinek and R. R. Netz, "Specific ion adsorption at hydrophobic solid surfaces," *Phys. Rev. Lett.*, vol. 99, p. 226104, 2007.

[121] P. Jungwirth and B. Winter, "Ions at aqueous interfaces: From water surface to hydrated proteins," *Annu. Rev. Phys. Chem.*, vol. 59, no. 1, pp. 343–366, 2008.

[122] M. Mucha, T. Frigato, L. M. Levering, H. C. Allen, D. J. Tobias, L. X. Dang, and P. Jungwirth, "Unified molecular picture of the surfaces of aqueous acid, base, and salt solutions," *J. Phys. Chem. B*, vol. 109, no. 16, pp. 7617–7623, 2005.

[123] A. J. Hopkins, S. Schrödle, and G. L. Richmond, "Specific ion effects of salt solutions at the CaF2/water interface," *Langmuir*, vol. 26, no. 13, pp. 10784–10790, 2010.

[124] A. Eftekhari-Bafrooei and E. Borguet, "Effect of surface charge on the vibrational dynamics of interfacial water," *J. Am. Chem. Soc.*, vol. 131, no. 34, pp. 12034–12035, 2009.

[125] X. Chen, W. Hua, Z. Huang, and H. C. Allen, "Interfacial water structure associated with phospholipid membranes studied by Phase-Sensitive vibrational sum frequency generation spectroscopy," *J. Am. Chem. Soc.*, vol. 132, no. 32, pp. 11336–11342, 2010.

[126] P. L. Hayes, J. N. Malin, C. T. Konek, and F. M. Geiger, "Interaction of nitrate, barium, strontium and cadmium ions with fused quartz/water interfaces studied by second harmonic generation," *J. Phys. Chem. A*, vol. 112, no. 4, pp. 660–668, 2008.

[127] M. Xu, C. Y. Tang, A. M. Jubb, X. Chen, and H. C. Allen, "Nitrate anions and ion pairing at the air-aqueous interface," *J. Phys. Chem. C*, vol. 113, no. 6,

pp. 2082–2087, 2009.

[128] Z. Zhang, P. Fenter, L. Cheng, N. C. Sturchio, M. J. Bedzyk, M. Předota, A. Bandura, J. D. Kubicki, S. N. Lvov, P. T. Cummings, A. A. Chialvo, M. K. Ridley, P. Bénézeth, L. Anovitz, D. A. Palmer, M. L. Machesky, and D. J. Wesolowski, "Ion adsorption at the rutile-water interface: Linking molecular and macroscopic properties," *Langmuir*, vol. 20, no. 12, pp. 4954–4969, 2004.

[129] V. Kohli, Z. Zhang, C. Park, and P. Fenter, "Rb+ and Sr2+ adsorption at the TiO2 (110)-electrolyte interface observed with resonant anomalous X-ray reflectivity," *Langmuir*, vol. 26, no. 2, pp. 950–958, 2010.

[130] P. Fenter and N. C. Sturchio, "Mineral-water interfacial structures revealed by synchrotron X-ray scattering," *Progress in Surface Science*, vol. 77, no. 5-8, pp. 171 – 258, 2004.

[131] E. C. Y. Yan, Y. Liu, and K. B. Eisenthal, "New method for determination of surface potential of microscopic particles by second harmonic generation," *J. Phys. Chem. B*, vol. 102, no. 33, pp. 6331–6336, 1998.

[132] Y. Liu, E. C. Y. Yan, X. Zhao, and K. B. Eisenthal, "Surface potential of charged liposomes determined by second harmonic generation," *Langmuir*, vol. 17, no. 7, pp. 2063–2066, 2001.

[133] J. G. Davis, K. P. Gierszal, P. Wang, and D. Ben-Amotz, "Water structural transformation at molecular hydrophobic interfaces," *Nature*, vol. 491, no. 7425, pp. 582–585, 2012.

[134] D. M. Huang and D. Chandler, "The hydrophobic effect and the influence of solute-solvent attractions," *J. Phys. Chem. B*, vol. 106, no. 8, pp. 2047–2053, 2002.

[135] J. Israelachvili, *Intermolecular and Surface Forces*. Elsevier, 2009.

[136] P. Calmettes, W. Kunz, and P. Turq, "Distribution of small organic cations in aqueous solutions," *Physica B: Condensed Matter*, vol. 180-181, Part 2, no. 0, pp. 868 – 870, 1992.

[137] A. Eftekhari-Bafrooei and E. Borguet, "Effect of electric fields on the ultrafast vibrational relaxation of water at a charged Solid-Liquid interface as probed by vibrational sum frequency generation," *J. Phys. Chem. Lett.*, vol. 2, no. 12, pp. 1353–1358, 2011.

[138] S. Roy and D. K. Hore, "Simulated Structure and Nonlinear Vibrational Spectra of Water Next to Hydrophobic and Hydrophilic Solid Surfaces," *J. Phys. Chem. C*, vol. 116, no. 43, pp. 22867–22877, 2012.

[139] X. Zhuang, P. B. Miranda, D. Kim, and Y. R. Shen, "Mapping molecular orientation and conformation at interfaces by surface nonlinear optics," *Phys. Rev. B*, vol. 59, no. 19, p. 12632, 1999.

[140] M. Vazdar, E. Pluharová, P. E. Mason, R. Vachá, and P. Jungwirth, "Ions at

hydrophobic aqueous interfaces: Molecular dynamics with effective polarization," *J. Phys. Chem. Lett.*, vol. 3, no. 15, pp. 2087–2091, 2012.

[141] K. Tamaki, "The surface activity of tetrabutylammonium halides in the aqueous solutions," *Bull. Chem. Soc. Jpn.*, vol. 40, no. 1, pp. 38–41, 1967.

[142] K. Tamaki, "The surface activity of tetraalkylammonium halides in aqueous solutions. the effect of hydrophobic hydration," *Bull. Chem. Soc. Jpn.*, vol. 47, no. 11, pp. 2764–2767, 1974.

[143] T. Hrobárik, L. Vrbka, and P. Jungwirth, "Selected biologically relevant ions at the air/water interface: A comparative molecular dynamics study," *Biophys. Chem.*, vol. 124, no. 3, pp. 238 – 242, 2006.

[144] S. Garde and A. J. Patel, "Unraveling the hydrophobic effect, one molecule at a time," *Proc. Natl. Acad. Sci.*, vol. 108, no. 40, pp. 16491–16492, 2011.

[145] D. A. Beattie, S. Haydock, and C. D. Bain, "A comparative study of confined organic monolayers by raman scattering and sum-frequency spectroscopy," *Vib. Spectrosc.*, vol. 24, no. 1, pp. 109 – 123, 2000.

[146] O. Esenturk and R. A. Walker, "Surface vibrational structure at alkane liquid/vapor interfaces," *J. Chem. Phys.*, vol. 125, no. 17, p. 174701, 2006.

[147] P. Guyot-Sionnest, J. H. Hunt, and Y. R. Shen, "Sum-frequency vibrational spectroscopy of a langmuir film: Study of molecular orientation of a two-dimensional system," *Phys. Rev. Lett.*, vol. 59, no. 14, p. 1597, 1987.

[148] F. Eschen, M. Heyerhoff, H. Morgner, and J. Vogt, "The concentration-depth profile at the surface of a solution of tetrabutylammonium iodide in formamide, based on angle-resolved photoelectron spectroscopy," *J. Phys.: Condens. Matter*, vol. 7, no. 10, p. 1961, 1995.

[149] R. Vácha and S. Roke, "Sodium dodecyl sulfate at water-hydrophobic interfaces: A simulation study," *J. Phys. Chem. B*, vol. 116, no. 39, pp. 11936–11942, 2012.

[150] R. Moberg, F. Boekman, O. Bohman, and H. O. G. Siegbahn, "ESCA studies of phase-transfer catalysts in solution: ion pairing and surface activity," *J. Am. Chem. Soc.*, vol. 113, no. 10, pp. 3663–3667, 1991.

[151] E. Kutluay, B. Roux, and L. Heginbotham, "Rapid intracellular TEA block of the KcsA potassium channel," *Biophys. J.*, vol. 88, no. 2, pp. 1018 – 1029, 2005.

[152] Q. Li, S. Xie, Z. Liang, X. Meng, S. Liu, H. H. Girault, and Y. Shao, "Fast ion-transfer processes at nanoscopic liquid/liquid interfaces," *Angew. Chem.*, vol. 121, no. 43, pp. 8154–8157, 2009.

[153] K. D. Collins and M. W. Washabaugh, "The Hofmeister effect and the behaviour of water at interfaces," *Q. Rev. Biophys.*, vol. 18, no. 04, pp. 323–422, 1985.

[154] N. Vlachy, B. Jagoda-Cwiklik, R. Vácha, D. Touraud, P. Jungwirth, and W. Kunz,

"Hofmeister series and specific interactions of charged headgroups with aqueous ions," *Advances in Colloid and Interface Science*, vol. 146, no. 1-2, pp. 42 – 47, 2009.

[155] S. Kumar, H. Patel, and S. Patil, "Test of Hofmeister-like series of anionic headgroups: clouding and micellar growth," *Colloid Polym. Sci.*, vol. 291, no. 9, pp. 2069–2077, 2013.

[156] P. N. Perera, K. R. Fega, C. Lawrence, E. J. Sundstrom, J. Tomlinson-Phillips, and D. Ben-Amotz, "Observation of water dangling OH bonds around dissolved nonpolar groups," *Proc. Natl. Acad. Sci.*, vol. 106, no. 30, pp. 12230 –12234, 2009.

[157] K. P. Gierszal, J. G. Davis, M. D. Hands, D. S. Wilcox, L. V. Slipchenko, and D. Ben-Amotz, "pi-hydrogen bonding in liquid water," *J. Phys. Chem. Lett.*, vol. 2, no. 22, pp. 2930–2933, 2011.

[158] J. R. Lu, A. Marrocco, T. J. Su, R. K. Thomas, and J. Penfold, "Adsorption of dodecyl sulfate surfactants with monovalent metal counterions at the air-water interface studied by neutron reflection and surface tension," *J. Colloid Interface Sci.*, vol. 158, no. 2, pp. 303 – 316, 1993.

[159] M. L. Schlossman and A. M. Tikhonov, "Molecular ordering and phase behavior of surfactants at water-oil interfaces as probed by X-ray surface scattering," *Annu. Rev. Phys. Chem.*, vol. 59, pp. 153–177, 2008.

[160] E. Sloutskin, Z. Sapir, C. D. Bain, Q. Lei, K. M. Wilkinson, L. Tamam, M. Deutsch, and B. M. Ocko, "Wetting, mixing, and phase transitions in Langmuir-Gibbs films," *Phys. Rev. Lett.*, vol. 99, p. 136102, 2007.

[161] E. Staples, J. Penfold, and I. Tucker, "Adsorption of mixed surfactants at the Oil-Water interface," *J. Phys. Chem. B*, vol. 104, no. 3, pp. 606–614, 2000.

[162] A. Zarbakhsh, J. R. P. Webster, and J. Eames, "Structural studies of surfactants at the oil-water interface by neutron reflectometery," *Langmuir*, vol. 25, no. 7, pp. 3953–3956, 2009.

[163] J. C. Conboy and G. L. Richmond, "Examination of the electrochemical interface between two immiscible electrolyte solutions by second harmonic generation," *J. Phys. Chem. B*, vol. 101, no. 6, pp. 983–990, 1997.

[164] M. M. Knock, G. R. Bell, E. K. Hill, H. J. Turner, and C. D. Bain, "Sum-Frequency spectroscopy of surfactant monolayers at the Oil-Water interface," *J. Phys. Chem. B*, vol. 107, no. 39, pp. 10801–10814, 2003.

[165] K. M. Wilkinson, L. Qunfang, and C. D. Bain, "Freezing transitions in mixed surfactant/alkane monolayers at the air-solution interface," *Soft Matter*, vol. 2, no. 1, pp. 66–76, 2006.

[166] H.-F. Wang, W. Gan, R. Lu, Y. Rao, and B.-H. Wu, "Quantitative spectral and orientational analysis in surface sum frequency generation vibrational spectroscopy

(SFG-VS)," *Int. Rev. Phys. Chem.*, vol. 24, no. 2, pp. 191–256, 2005.

[167] P. Mukerjee, K. Mysels, and P. Kapauan, "Counterion specificity in the formation of ionic micelles - size, hydration, and hydrophobic bonding effects," *J. Phys. Chem.*, vol. 71, no. 13, pp. 4166–4175, 1967.

[168] J. Goodwin, *Colloids and Interfaces with Surfactants and Polymers: An Introduction.* Wiley, 2004.

[169] "General discussion," *Faraday Discuss.*, vol. 160, pp. 311–327, 2013.

[170] R. Aveyard, B. Binks, P. Cooper, and P. Fletcher, "Incorporation of hydrocarbons into surfactant monolayers," *Adv. Colloid Interface Sci.*, vol. 33, no. 2-4, pp. 59 – 77, 1990.

[171] R. Vacha, S. W. Rick, P. Jungwirth, A. G. F. de Beer, H. B. de Aguiar, J. Samson, and S. Roke, "The orientation and charge of water at the hydrophobic oil Droplet-Water interface," *J. Am. Chem. Soc.*, vol. 133, no. 26, pp. 10204–10210, 2011.

[172] G. Hummer, L. R. Pratt, and A. E. Garcia, "Free energy of ionic hydration," *J. Phys. Chem.*, vol. 100, no. 4, pp. 1206–1215, 1996.

[173] R. M. Lynden-Bell and J. C. Rasaiah, "From hydrophobic to hydrophilic behaviour: A simulation study of solvation entropy and free energy of simple solutes," *J. Chem. Phys.*, vol. 107, no. 6, pp. 1981–1991, 1997.

[174] T. L. Beck, "The influence of water interfacial potentials on ion hydration in bulk water and near interfaces," *Chem. Phys. Lett.*, vol. 561-562, no. 0, pp. 1 – 13, 2013.

[175] K. D. Collins, G. W. Neilson, and J. E. Enderby, "Ions in water: Characterizing the forces that control chemical processes and biological structure," *Biophys. Chem.*, vol. 128, no. 2-3, pp. 95 – 104, 2007.

[176] D. Laage, G. Stirnemann, F. Sterpone, R. Rey, and J. T. Hynes, "Reorientation and allied dynamics in water and aqueous solutions," *Annu. Rev. Phys. Chem.*, vol. 62, pp. 395–416, 2011.

[177] F. N. Keutsch and R. J. Saykally, "Water clusters: Untangling the mysteries of the liquid, one molecule at a time," *Proc. Natl. Acad. Sci.*, vol. 98, no. 19, pp. 10533–10540, 2001.

[178] L. V. Slipchenko and M. S. Gordon, "Damping functions in the effective fragment potential method," *Mol. Phys.*, vol. 107, no. 8-12, pp. 999–1016, 2009.

[179] E. Grunwald, G. Baughman, and G. Kohnstam, "The solvation of electrolytes in dioxane-water mixtures, as deduced from the effect of solvent change on the standard partial molar free energy," *J. Am. Chem. Soc.*, vol. 82, no. 22, pp. 5801–5811, 1960.

[180] A. Grossfield, P. Ren, and J. W. Ponder, "Ion solvation thermodynamics from simulation with a polarizable force field," *J. Am. Chem. Soc.*, vol. 125, no. 50, pp. 15671–15682, 2003.

[181] H. L. Friedman, "Regularities and specific effects in enthalpies of transfer of ions from water to aprotic solvents," *J. Phys. Chem.*, vol. 71, no. 6, pp. 1723–1726, 1967.

[182] J. F. Coetzee and W. R. Sharpe, "Solute-solvent interactions. VI. Specific interactions of tetraphenylarsonium, tetraphenylphosphonium, and tetraphenylborate ions with water and other solvents," *J. Phys. Chem.*, vol. 75, no. 20, pp. 3141–3146, 1971.

[183] B. G. Cox and A. J. Parker, "Solvation of ions. XVII. Free energies, heats, and entropies of transfer of single ions from protic to dipolar aprotic solvents," *J. Am. Chem. Soc.*, vol. 95, no. 2, pp. 402–407, 1973.

[184] W. Wachter, R. Buchner, and G. Hefter, "Hydration of tetraphenylphosphonium and tetraphenylborate ions by dielectric relaxation spectroscopy," *J. Phys. Chem. B*, vol. 110, no. 10, pp. 5147–5154, 2006.

[185] T. S. Zwier, "The spectroscopy of solvation in hydrogen-bonded aromatic clusters," *Annu. Rev. Phys. Chem.*, vol. 47, no. 1, pp. 205–241, 1996.

[186] R. K. Campen, A. K. Pymer, S. Nihonyanagi, and E. Borguet, "Linking surface potential and deprotonation in nanoporous silica: Second harmonic generation and acid/base titration," *J. Phys. Chem. C*, vol. 114, no. 43, pp. 18465–18473, 2010.

[187] Y. R. Shen and V. Ostroverkhov, "Sum-frequency vibrational spectroscopy on water interfaces: Polar orientation of water molecules at interfaces," *Chem. Rev.*, vol. 106, no. 4, pp. 1140–1154, 2006.

[188] G. Varsanyi, *Assignments for Vibrational Spectra of Benzene Derivatives*, vol. 1. Adam Hilger, London, 1974.

[189] D. C. Duffy, P. B. Davies, and C. D. Bain, "Surface vibrational spectroscopy of organic counterions bound to a surfactant monolayer," *J. Phys. Chem.*, vol. 99, no. 41, pp. 15241–15246, 1995.

[190] K. S. Gautam, A. D. Schwab, A. Dhinojwala, D. Zhang, S. M. Dougal, and M. S. Yeganeh, "Molecular structure of polystyrene at air/polymer and solid/polymer interfaces," *Phys. Rev. Lett.*, vol. 85, pp. 3854–3857, 2000.

[191] M. Oh-e, S.-C. Hong, and Y. R. Shen, "Orientations of phenyl sidegroups and liquid crystal molecules on a rubbed polystyrene surface," *Appl. Phys. Lett.*, vol. 80, no. 5, pp. 784–786, 2002.

[192] K. A. Briggman, J. C. Stephenson, W. E. Wallace, and L. J. Richter, "Absolute molecular orientational distribution of the polystyrene surface," *J. Phys. Chem. B*, vol. 105, no. 14, pp. 2785–2791, 2001.

[193] E. L. Hommel and H. C. Allen, "The air-liquid interface of benzene, toluene, m-xylene, and mesitylene: a sum frequency, raman, and infrared spectroscopic study," *Analyst*, vol. 128, pp. 750–755, 2003.

[194] R. Schurhammer and G. Wipff, "Are the hydrophobic AsPh4+ and BPh4- ions equally solvated? a theoretical investigation in aqueous and nonaqueous solutions

using different charge distributions," *J. Phys. Chem. A*, vol. 104, no. 47, pp. 11159–11168, 2000.

# Curriculum Vitae

**Rüdiger Scheu**
Chemin du Mont-Tendre 18
1007 Lausanne
email: ruediger.scheu@gmx.de

born on 2.8.1981 in Böblingen, Germany
unmarried, German

## Education and Professional Experience

| | |
|---|---|
| 01/2010–ongoing | PhD Photonics program, École Polytechnique Fédérale de Lausanne<br>Title of thesis: *Specific ion effects and the molecular structure of water, ions, and amphiphiles on nanoscopic hydrophobic interfaces*<br>Thesis director: Prof. Sylvie Roke |
| 03/2009–09/2009 | Internship Toptica Photonics in Gräfelfing, Germany: research and development, femtosecond fibre lasers |
| 11/2008–12/2008 | Scientist in Rupert Huber's group, University of Konstanz |
| 10/2002–09/2008 | Diploma in Physics, Universtiy of Konstanz,<br>Title of Thesis: *Ultrabroadband THz-Optoelectronics based on a fs Erbium fibre laser*<br>Group of Prof. Alfred Leitenstorfer,<br>Supervisor: Prof. Rupert Huber |

## Teaching Experience

| | |
|---|---|
| 2012/2013 | Tutoring in Life Sciences at EPFL, Lausanne |
| 2007/2008 | Physics tutor in the Department of Physics, University of Konstanz |
| 2005 | Math tutor in the Department of Mathematics, University of Konstanz |

## Foreign Experience

| | |
|---|---|
| 09/2005–09/2006 | University of Western Ontario in London, Canada<br>Scholarship of the "Landesstiftung Baden-Württemberg" |
| 01/2006–09/2006 | Research project in the group of Prof. Silvia Mittler, University of Western Ontario:<br>*White light spectroscopy with gold nanoparticles* |

## Soft skills

| | |
|---|---|
| Languages | fluent in English and French<br>basics in Spanish |
| Computer | Python, Matlab, Mathematica, SolidWorks (CAD), Labview, Latex, Inkscape, MS-Office |
| Teaching | Dance instructor, Swing Dance (Lindy Hop) |

Lausanne, November 2013